STUDY OF THE CHARM MESON DECAYS USING BELLE II EXPERIMENT

A THESIS

Submitted to the

PANJAB UNIVERSITY, CHANDIGARH

For the Award of

DOCTOR OF PHILOSOPHY

2024

in

FACULTY OF SCIENCE

BY

LATIKA AGGARWAL

GUIDE

Dr. Sunil Bansal **Dr. Vishal Bhardwaj**

DEPARTMENT OF PHYSICS
PANJAB UNIVERSITY
CHANDIGARH, INDIA

September, 2024

DECLARATION

I declare that the thesis entitled "**STUDY OF THE CHARM MESON DECAYS USING BELLE II EXPERIMENT**" has been prepared by me under the guidance of Dr. Sunil Bansal, University Institute of Engineering and Technology, Panjab University, Chandigarh and Dr. Vishal Bhardwaj, Indian Institute of Science Education and Research, Mohali. No part of this thesis has formed the basis for the award of any degree or fellowship previously.

Latika Aggarwal

Department of Physics

Panjab University, Chandigarh, India

DATE:

CERTIFICATE

We certify that Latika Aggarwal has prepared her thesis entitled "**STUDY OF THE CHARM MESON DECAYS USING BELLE II EXPERIMENT**", for the award of Ph.D. degree of the Panjab University, Chandigarh, under our guidance. She has carried out the work at the Department of Physics, Panjab University, Chandigarh and University Institute of Engineering and Technology, Panjab University, Chandigarh.

Dr. Sunil Bansal
University Institute of Engineering and Technology,
Panjab University,
Chandigarh-160014

Dr. Vishal Bhardwaj
Indian Institute of Science
Education and Research,
Mohali-140306

DATE:

DATE:

Dedicated to

My Family

and
Friends

Acknowledgements

First and foremost, I am extremely thankful to the Almighty, the supreme power, for blessing me with an amazing life, health and strength to overcome the difficulties and stay motivated towards this wonderful journey. Thank you, Almighty for blessing me with what I have desired.

I feel privileged to acknowledge my deep sense of gratitude to my Supervisors Dr. Sunil Bansal and Dr. Vishal Bhardwaj for their unwavering support, guidance and patience throughout the entirety of my Ph.D. journey. Their insights and expertise have been invaluable and their encouragement have been a constant source of motivation.

From the very beginning of my Ph.D. journey, Dr. Sunil Bansal has shown an exceptional level of commitment and dedication. His insightful feedback and academic guidance have shaped my growth as a researcher and an individual. His ability to inspire and motivate has been a constant source of strength for me.

Dr. Vishal Bhardwaj has also been incredibly generous with his time and resources and has created a friendly environment for seeking advice and discussing any concerns. His dedication, encouragement and insightful feedback have played a pivotal role in shaping the outcome of this thesis.

I want to express a special thanks to Prof. J.B. Singh for the constant discussion, guidance and moral support throughout the Ph.D. journey. His expertise and enthusiasm for research has profoundly influenced my approach to academia. It has been an honor and a privilege to work under his guidance.

I would also like to extend my appreciation to the Director of UIET and the Chairperson of the Department of Physics for providing facilities to work at UIET *and the Physics Department. I am also grateful to the members of my research advisory committee (RAC), Prof. Monika Randhawa, Prof. Vipin Bhatnagar and Dr. Suresh Kumar for their constructive feedback and suggestions that help me to improve the quality of my research.*

I would like to acknowledge the financial assistance given to me, in the form of a research fellowship, by the University Grants Commission, New Delhi, India during my Ph.D.

I am thankful to my seniors, colleagues and friends Dr. Meena, Dr. Rajat Gupta, Dr. Amandeep Kaur Virdi, Dr. Jyoti Babbar, Dr. Amandeep Kaur, Dr. Sandeep Hundle, Dr. Gitanjali, Dr. Harjot, Ayushi, Sunil, Prachi, and Bhumika. I am also grateful to my colleagues and friends in the Belle II collaboration Dr. Manish, Dr. Renu, Sanjeeda, Chanchal, Shubhangi, Ipsita, Sourabh and Neetesh for their help and support throughout my research work.

I would like to extend my appreciation to my best friends Diwanshu and Bhumika. Your unwavering friendship, encouragement, and understanding have been a constant source of strength and joy in both high and low times. Thank you for the countless hours of listening, the laughter and belief in my abilities. Your support has been invaluable in my life.

A heartfelt thank you to my family. First and foremost, I am deeply grateful to my mother, Smt. Kanta Devi, who is an inspiration to me. She is a perfect example of how an individual should be and I aspire to be like her in every way. Her unconditional love, encouragement and sacrifices have enabled me to pursue my dreams. I would like to thank my late father, Sh. Vidya Bhushan, who is no longer with us, but whose blessings continue to guide me which has been a constant source of encouragement. I am also grateful to my cousins Varun, Tawish, Tawisha and

Chahat for their unconditional love. Special thanks to my cousin and friend Shelza for all the happiness, support, love and encouragement in all aspects of my life.

My sincere gratitude extends to my father-in-law, Sh. Krishan Lal and my mother-in-law, Smt. Sunita Rani, for their love and encouragement. I would appreciate my brother-in-law, Mr. Gagan Goyal and my sister-in-law, Mrs. Shinu Rani for their help and care throughout this journey. I would also like to thank the little ones of our family Navika and Vinayak for bringing immense joy and laughter during stressful days. I am thankful to all the family members and relatives for their support.

Finally, I am extremely thankful to Dr. Manish Goyal, my husband for unconditional love and care. His unwavering support and understanding have been my guide through the ups and downs of this journey. This would not have been possible without his support. I am deeply grateful for your presence in my life.

I offer my sincere thanks to all those who have contributed to this work, directly or indirectly.

Latika Aggarwal

List of Publications

Internal Belle II note :

1. Rediscovery of D^0 $, \rightarrow$ $K_S\pi^0$ with Belle II Detector.
   Latika Aggarwal, Sunil Bansal, Vishal Bhardwaj and J.B. Singh, BELLE2-NOTE-PH-2020-037.

2. Measurement of branching fraction of $D_s^{*+} \rightarrow D_s^+\pi^0$ relative to $D_s^{*+} \rightarrow D_s^+\gamma$.
   Latika Aggarwal, Sunil Bansal and Vishal Bhardwaj, BELLE2-NOTE-PH-2023-031.

Published conference proceedings

1. L. Aggarwal, "Rare Charm Decays at Belle II", Springer Proceedings in Physics, vol. 277 (2022). Springer, Singapore. doi.org/10.1007/978-981-19-2354-8_26.

2. L. Aggarwal, S. Bansal and V. Bhardwaj, "Measurements of the Ratio of Partial Widths: $\Gamma(D_s^{*+} \rightarrow D_s^+\pi^0)/\Gamma(D_s^{*+} \rightarrow D_s^+\gamma)$", Springer Proceedings in Physics, vol. 304. Springer, Singapore. doi.org/10.1007/978-981-97-0289-3_357.

Publications as co-author with Belle II Collaboration

1. Belle II Collaboration,"Precise measurement of the D^0 and D^+ lifetimes at Belle II", Phys. Rev. Lett. **127**, 211801 (2021).

2. Belle II Collaboration, "Combined analysis of Belle and Belle II data to determine the CKM angle ϕ_3 using $B^+ \rightarrow D(K_s^0 h^+ h^-)h^+$ decays", JHEP **2022**, 063 (2022).

3. Belle II Collaboration, "Measurement of lepton mass squared moments in $B \rightarrow X_c l \bar{\nu}_l$ decays with the Belle II experiment", Phys. Rev. D **107**, 072002 (2023).

4. Belle II Collaboration, “Measurement of the Λ_c^+ lifetime”, Phys. Rev. Lett. **130**, 071802 (2023).

5. Belle II Collaboration, “Search for a dark photon and an invisible dark Higgs boson in $\mu^+\mu^-$ and missing energy final states with the Belle II experiment”, Phys. Rev. Lett. **130**, 071804 (2023).

6. Belle II Collaboration, “Measurement of the Ω_c^0 lifetime at Belle II”, Phys. Rev. D **107**, L031103 (2023).

7. Belle II Collaboration, “Observation of $e^+e^- \to \omega\chi_{bJ}$ and search for $X_b \to \omega\Upsilon(1S)$ at $\sqrt{s}$ near 10.75 GeV”, Phys. Rev. Lett. **130**, 091902 (2023).

8. Belle II Collaboration, “Search for an invisible $Z^{'}$ in a final state with two muons and missing energy at Belle II”, Phys. Rev. Lett. **130**, 231801 (2023).

9. Belle II Collaboration, “Search for lepton-flavor-violating τ decays to a lepton and an invisible boson at Belle II”, Phys. Rev. Lett. **130**, 181803 (2023).

10. Belle II Collaboration, “A test of light-lepton universality in the rates of inclusive semileptonic B-meson decays at Belle II”, Phys. Rev. Lett. **131**, 051804 (2023).

11. Belle II Collaboration, “Measurement of the B^0 lifetime and flavor-oscillation frequency using hadronic decays reconstructed in 2019-2021 Belle II data”, Phys. Rev. D **107**, L091102 (2023).

12. Belle II Collaboration, “Measurement of the branching fraction and CP asymmetry of $B^0 \to \pi^0\pi^0$ decays using 2019-2021 Belle II data”, Phys. Rev. D **107**, 112009 (2023).

13. Belle II Collaboration, “Novel method for the identification of the production flavor of neutral charmed mesons”, Phys. Rev. D **107**, 112010 (2023).

14. Belle II Collaboration, “Measurement of CP violation in $B^0 \to K_s^0\pi^0$ decays at Belle II”, Phys. Rev. Lett. **131**, 111803 (2023).

15. Belle II Collaboration, “Measurement of the τ-lepton mass with the Belle II experiment”, Phys. Rev. D **108**, 032006 (2023).

16. Belle II Collaboration, “Precise measurement of the D_s^+ lifetime at Belle II”, Phys. Rev. Lett. **131**, 171803 (2023).

17. Belle II Collaboration, “Search for a long-lived spin-0 mediator in $b \to s$ transitions at the Belle II experiment”, Phys. Rev. D **108**, L111104 (2023).

18. Belle II Collaboration, “Measurement of CP asymmetries and branching-fraction ratios for $B^{\pm} \to DK^{\pm}$ and $D\pi^{\pm}$ with $D \to K_s^0 K^{\pm} \pi^{mp}$ using Belle and Belle II data”, JHEP **2023**, 146 (2023).

19. Belle II Collaboration, “Search for a $\tau^+\tau^-$ resonance in $e^+e^- \to \mu^+\mu^-\tau^+\tau^-$ events with the Belle II experiment”, Phys. Rev. Lett. **131**, 121802 (2023).

20. Belle II Collaboration, “Measurement of CP asymmetries in $B^0 \to \phi K_s^0$ with Belle II”, Phys. Rev. D **108**, 072012 (2023).

21. Belle II Collaboration, “Tests of light-lepton universality in angular asymmetries of $B^0 \to D^{*-} l\nu$ decays”, Phys. Rev. Lett. **131**, 181801 (2023).

22. Belle II Collaboration, “Measurement of branching-fraction ratios and CP asymmetries in $B^{\pm} \to D_{CP} K^{\pm}$ decays at Belle and Belle II”, JHEP **2024**, 212 (20204).

23. Belle II Collaboration, “Determination of $|V_{cb}|$ using $\bar{B}^0 D^{*+} l^- \bar{\nu}_l$ decays with Belle II”, Phys. Rev. D **108**, 092013 (2023).

24. Belle II Collaboration, “Measurement of branching fractions and direct CP asymmetries for $B \to K\pi$ and $B \to \pi\pi$ decays at Belle II”, Phys. Rev. D **109**, 012001 (2024).

25. Belle II Collaboration, “First measurement of $R(X_{\tau/l})$ as an inclusive test of the $b \to c\tau\nu$ anomaly”, Phys. Rev. Lett. **132**, 211804 (2024).

26. Belle II Collaboration, "Evidence for $B^+ \to K^+\nu\bar{\nu}$ decays", Phys. Rev. D **109**, 112006 (2024).

27. Belle II Collaboration, "Search for the $e^+e^- \to \eta_b(1S)\omega$ and $e^+e^- \to \chi_{b0}(1P)\omega$ processes at $\sqrt{s} = 10.745$ GeV", Phys. Rev. D **109, 072013** (2024).

28. Belle II Collaboration, "A new graph-neural-network flavor tagger for Belle II and measurement of $\sin(2\phi_1)$ in $B^0 \to J/\psi K_s^0$decays", Phys. Rev. D **110**, 012001 (2024).

29. Belle II Collaboration, "Measurement of CP asymmetries in $B^0 \to K_s^0 K_s^0 K_s^0$ decays at Belle II", Phys. Rev. D **109**, 112020 (2024).

30. Belle II Collaboration, "Search for a $\mu^+\mu^-$ resonance in four-muon final states at Belle II", Phys. Rev. D **109**, 112015 (2024).

Presentations in Conferences and Symposiums

1. Presented in the "XXIV DAE-BRNS Symposium on High Energy Physics" held online by the National Institute of Science Education and Research, Jatni, Odisha, India during December 14-18, 2020.

2. Presented in the "15^{th} Chandigarh Science Congress (CHASCON) 2022" held at Panjab University, Chandigarh, India from September 15-17, 2022.

3. Presented in the "XXV DAE-BRNS Symposium on High Energy Physics" held at Indian Institute of Science Education and Research, Mohali, Punjab, India from December 12-16, 2022.

4. Presented in the "16^{th} Chandigarh Science Congress (CHASCON) 2023" held at Panjab University, Chandigarh, India from October 12-14, 2023.

Contents

List of Figures

List of Tables

Abstract

The Standard Model of elementary particle physics is the most successful theory to explain the fundamental particles and their interactions. Despite its success, the Standard Model leaves many questions unanswered, such as the fundamental characterstics of gravity, the source of neutrino masses, dark matter, dark energy, and the matter-antimatter asymmetry in the universe. The observed CP violation is insufficient to explain the universe's matter dominance, suggesting undiscovered sources of CP asymmetry. The Belle II experiment situated at the SuperKEKB accelerator, Japan aims to explore new physics in quark and lepton flavor transition by covering data ranges from 1 ab^{-1} to 50 ab^{-1}. This large data sample enables detailed probes of new physics and cross-checks against Standard Model deviations. Flavor physics in the charm sector plays a key role in exploring the physics beyond the Standard Model. The Belle II experiment conducts a broad charm physics program that provides many opportunities to test the Standard Model predictions and search for the signatures of new physics. The higher trigger efficiency, excellent γ and π^0 particle reconstruction, efficient flavor-tagging and access to a number of control samples for systematic studies are some of the advantages of studying charm physics at Belle II.

The analysis presented in this thesis "measurements of the branching fraction $\mathcal{B}(D_s^{*+} \to D_s^+\pi^0)$ with respect to $\mathcal{B}(D_s^{*+} \to D_s^+\gamma)$" is important for understanding the strong interactions involving the charm quarks in Quantum Chromodynamics (QCD). These measurements can provide crucial input for the theoretical models. By comparing experimental results with the theoretical predictions, these models can be improved. Additionally, these measurements test the Standard Model predictions where any deviation from the expected results can indicate the presence of new physics beyond the Standard Model. These early and precise measurements from Belle II data also help in evaluating the Belle II detector's performance. These measurements are performed using an integrated luminosity of 424 fb^{-1} of e^+e^- collision data at or near the $\Upsilon(4S)$ resonance using the Belle II detector. This analysis reports the most precise result to date and found to be consistent with the previous measurements and theoretical predictions.

Chapter 1

Introduction

For centuries, the question of "What is the world made of?" or more simply, "What is matter made of?" has been a widespread inquiry. Elementary particle physics addresses this question on the smallest scale of size. It is a branch of physics dedicated to the study of fundamental particles and their properties. Fundamental particles also known as elementary particles lack substructure which means they are not composed of smaller objects. The history of elementary particle physics is a journey marked by significant discoveries and theoretical advancements. In 1897, the study of particle physics was started when the electron was discovered by J.J. Thomson [1] which changed our understanding of atomic structure. In 1911, Ernest Rutherford's gold foil experiment demonstrated that most of the atom's mass concentrated at the positive core which is surrounded by electrons [2]. With the discovery of neutrons by James Chadwick in 1932 [3], it became clear that the nucleus is made of neurons and protons. The development of quantum mechanics provided a framework for understanding of atomic and subatomic processes. In the 1960s, the quark model was independently proposed by Gell-Mann and George Zweig, suggesting that protons, neutrons, and other hadrons are composed of quarks [4, 5]. This period led to the development of quantum field theories [6] and discoveries of various quarks, bosons and mesons with the help of various cosmic ray experiments or accelerators such as cyclotrons, betatrons and synchrotrons. A detailed description can be found in [7]. The Standard Model of Particle Physics is the current best theory to describe the most basic building blocks of the universe and the interactions between them [8, 9]. The Standard Model is complete after the discovery of the Higgs bosons in 2012, at the Large Hadron Collider (LHC) at CERN [10, 11], which provided an evidence for the mechanism that gives mass to elementary particles [12].

1.1 The Standard Model of Particle Physics

The Standard Model of particle physics is the effective quantum field theory that describes the fundamental particles and interactions between them. The quantum field theory framework emerges from combining quantum mechanics with special relativity and provides the most fundamental description of nature known today. The quantum field interacts with each other and the Standard Model describes these interactions at the subatomic level. The Lagrangian formalism is used to describe particles and their interactions which are not forbidden by the symmetries of the dynamics. The core concept is local gauge symmetry which means that the Lagrangian remains unchanged under space-time-dependent transformations of field phases. Interaction terms appear in the Lagrangian when it is required to be invariant under these local gauge symmetries. The Standard Model is based on the symmetry group

$$SU(3)_C \otimes SU(2)_L \otimes U(1)_Y,$$

where $SU(3)_C$ describes the strong interactions with C stands for color charge [13]. $SU(2)_L \otimes U(1)_Y$ describes the combination of weak and electromagnetic interactions. Three distinguished physicists-Steven Weinberg, Abdus Salam, and Sheldon Glashow-each independently proposed a theoretical framework to unify two fundamental interactions: the electromagnetic and weak forces [14–16]. $SU(2)_L$ represents

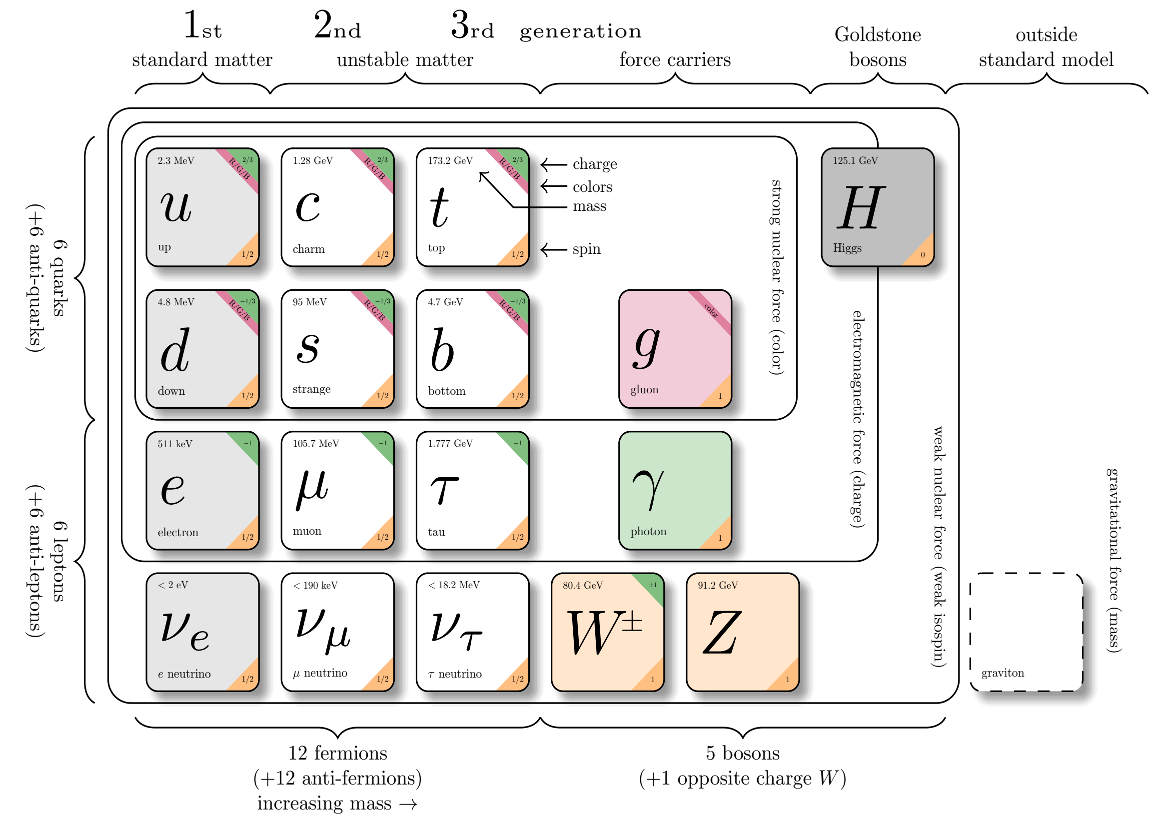

Figure 1.1: Scheme of particles and interactions in the Standard Model [17].

weak isospin doublets where "L" indicates that only particles with left chirality are affected by the weak interactions.

Figure 1.1 depicts the full range of fundamental particles included in the Standard Model. The Standard Model categorizes all known elementary particles into two main groups: fermions and bosons. Fermions are the building blocks of matter and bosons are force carriers. In the Standard Model, bosons are classified into two groups: gauge bosons with spin 1 and a scalar boson called Higgs boson with spin 0. The gauge bosons mediate interactions between the fundamental particles.

	Lepton	Symbol	Anti-particle	Charge	Mass (Mev/c^2)	Mean life
First Generation	Electron	e^-	e^+	-1	0.511	stable
	e-neutrino	ν_e	$\bar{\nu_e}$	0	$< 2.2 \times 10^{-6}$	stable
Second Generation	Muon	μ^-	μ^+	-1	105.7	2.2×10^{-6}
	μ-neutrino	ν_μ	$\bar{\nu_\mu}$	0	< 0.17	stable
Third Generation	Tau	τ^-	τ^+	-1	1776.8	2.9×10^{-13}
	τ-neutrino	ν_τ	$\bar{\nu_\tau}$	0	< 15.5	stable

Table 1.1: Leptons and their properties

1.1.1 Fundamental Particles

As discussed above, the Standard Model explains how fundamental spin $\frac{1}{2}$ fermions; quarks and leptons form up all known matter. Quarks and leptons along with their antiparticles come in three groups called families.

The lepton family includes charged electron (e), muon (μ) and tau (τ) and they carry integral electric charges. The μ and τ are heavier versions of the electron. Neutrinos, ν are the neutral leptons and each type of the charged lepton has its corresponding flavor of neutrino, indicated by a subscript. The mass of the τ (μ) particle is about 3478 (207) times that of the mass of the e, so both charged τ and μ are unstable and quickly decay into electrons, neutrinos and other particles. The average lifetime of the μ is about 2.2×10^{-6} s while that of the τ is much shorter about only 2.9×10^{-13} s. There are also six antileptons with opposite charges compared to corresponding leptons. Each pair of leptons is assigned a lepton number, represented by L_e, L_μ and L_τ. For the e^- and its neutrino, ν_e, $L_e = +1$ while their antiparticles (e^+ and $\bar{\nu_e}$) have L_e = -1. Similarly, L_μ and L_τ are assigned to μ and τ and their respective, neutrinos. The charged leptons interact through weak and electromagnetic forces while neutrinos interact only via weak force. Table 1.1 represents the lepton classification along with their properties.

The quarks carry fractional electric charges like $+\frac{2}{3}$ or $-\frac{1}{3}$ of unit electronic charge e. Similar to the leptons, the quarks are also grouped into pairs with electric

	Quark	Symbol	Antiparticle	Charge	Mass (MeV/c^2)	Isospin	Strangeness
First	Down	d	$\bar{d}$	-1/3	4.8	1/2	0
Generation	Up	u	$\bar{u}$	2/3	2.3	1/2	0
Second	Strange	s	$\bar{s}$	-1/3	95	0	-1
Generation	Charm	c	$\bar{c}$	2/3	1275	0	0
Third	Bottom	b	$\bar{b}$	-1/3	4180	0	0
Generation	Top	t	$\bar{t}$	2/3	173210	0	0

Table 1.2: Quarks and their properties

charges differing by one unit. Each type of quark called 'flavor' is represented by a symbol: u for 'up', d for 'down', s for 'strange', c for 'charmed', b for 'bottom' and t for 'top'. Quarks interact through the strong, electromagnetic and weak forces.

Unlike leptons, quarks cannot exist as free particles because of the phenomenon known as quark confinement. According to this, they can only be found bound together in combinations, such as mesons are made up of quark-antiquark pairs while baryons consist of three quarks. When the quarks are forced to separate from each other, the attractive potential energy of the strong interaction between them increases and requires more energy to separate them. This energy eventually creates new quark-antiquark pairs and ensures quarks remain bound together and never exist independently.

The stable particles of the universe, i.e. the electrons, e and the u and d quarks make up all the matter. The heavier quarks s, c and b also combines to form particles like protons and neutrons but they are unstable and decay in typically 10^{-13} s to u and d combinations like the heavy leptons decay to electrons. Table 1.2 represents quark classification with their properties.

Quarks are also characterized by a property called color that leads to interactions and spectroscopies and this phenomenon is different from those of leptons. The three colors of quarks are named red (r), green (g), and blue (b). Meson and baryon states must have a net zero value of all three color charges known as color singlets and expressed in the principle of color confinement first developed by Greenberg [18].

1.1.2 Fundamental Interactions

All elementary particles interact with each other through fundamental interactions. These interactions are classified based on their strength, effective range, and the nature of the mediating particles. There are four fundamental forces in nature: Strong, Electromagnetic (EM), Weak, and Gravitational. Table 1.3 summarizes these interactions along with their mediating particles.

- **Strong Interactions:** The strong interactions bind the quarks together in the neutron and proton, and the neutrons and protons within atomic nuclei. This force overcomes the electromagnetic repulsion between positively charged protons and ensures nuclear stability [7]. The interquark force is mediated by a massless particle called the gluon which carries the color charge. This force acts only on the particles that possess colored charge such as quarks and gluons themselves. Gluons not only mediate strong interactions but also have the possibility of self-interactions.

- **Weak Interactions:** The weak interactions are mediated by both electrically neutral Z^0 bosons and positively and negatively charged $W^{\pm}$ bosons. The Z^0 and $W^{\pm}$ bosons have a unique property that they are the only type of gauge bosons having mass [19, 20]. Weak interactions change the flavor of the quarks and enable transformations between different types of particles.

- **Electromagnetic Interactions:** The electromagnetic interactions are mediated by the photon exchange. This interaction acts between particles that carry the electric charge. This interaction affects the structure of atoms and governs the behavior of light. Quantum Electrodynamics (QED) provides a highly precise framework for describing this force [21].

- **Gravitational Interactions:** The gravitational forces act universally on the particles but are the weakest of the four fundamental forces in particle physics experiments, approximately 10^{-39} times weaker than the strong interactions. It is mediated by the exchange of a spin 2 boson called the graviton. The graviton has not been experimentally observed yet and also is not a part of the theoretical framework of the Standard Model.

Interaction	Strength	Range	Mediator	Mass (GeV)	Charge	Spin
Strong	1	10^{-13}	Gluons	0	0	1
Electromagnetic	$\frac{1}{137}$	∞	Photon	0	0	1
Weak	10^{-9}	10^{-16}	$W^{\pm}$, Z^{0}	80.39, 91.19	$\pm e$, 0	1
Gravitational	10^{-39}	∞	Graviton	0	0	2

Table 1.3: Characteristics of the fundamental interactions.

The last remaining boson of the Standard Model is the scalar Higgs boson which arises from the excitation of the Higgs field. The Higgs field was first proposed in 1964 [12] and this field penetrates all matter and space in the universe and provides a mechanism for fundamental particles to acquire mass through their interactions with the field. The Higgs field also breaks the electroweak symmetry that arises from the unification of the weak and electromagnetic forces to allow force carrying particles such as the Z^0 and $W^{\pm}$ bosons to have mass [22]. The Higgs boson was discovered in 2012 by CMS and ATLAS experiments at CERN's LHC [10, 11].

1.1.3 Physics beyond the Standard Model

Despite its enormous success in describing the basic building blocks and fundamental forces of nature, the Standard Model leaves many of the fundamental questions unanswered. The Standard Model doesn't account for the mediation of gravity and there is no evidence supporting the existence of gravitons. Neutrinos are assumed to be massless in the Standard Model but there is strong evidence of their finite masses [23] which leads to the possible hints of physics beyond the Standard Model.

The origin of the parameters governing six quark and six lepton flavors remains unclear. Additionally, the Standard Model does not explain dark matter, dark energy and the matter-antimatter asymmetry of the universe. The violation of CP symmetry is a necessary condition for the evolution of a matter-dominated universe [24] but the observed CP violation in the quark sector that originates from the complex phase of the Cabibbo-Kobayashi-Maskawa (CKM) matrix [25] is not sufficient to explain the dominance of matter in the universe. This observation suggests there must exist undiscovered sources of the CP asymmetry that are responsible for the matter-dominated Universe. To explain these observations, several theoretical models beyond the Standard Model i.e. Supersymmetry (SUSY) [26], Minimum Supersymmetric Standard Model (MSSM) [27], Extra Dimensions, etc., have been proposed but these models are not yet experimentally supported.

The observations and theoretical considerations suggested that the Standard Model has been successful but at the energy range from eV–TeV. One of the main goals of today's particle physics is to extend the Standard Model to the higher energy scale to address the unresolved issues. There are three approaches to explore physics beyond the Standard Model: Energy frontier, Intensity frontier and Cosmic frontier. Figure 1.2 represents the reach of various colliders in searching for new physics.

The energy frontier approach in high energy physics uses powerful accelerators to explore the fundamental nature of matter by colliding the particles at very high energies. The goal of this approach is to discover new particles, explore new energy regimes and test the Standard Model. At the energy frontier, CMS [29] and ATLAS [30] experiments at the Large Hadron Collider [31] have discovered new particles through proton-proton collision data at center-of-mass energy, $\sqrt{s} \sim$ 14 TeV. The discovery of the Higgs boson by the ATLAS and CMS experiments at LHC in 2012, is one of the remarkable examples of the discoveries made at the

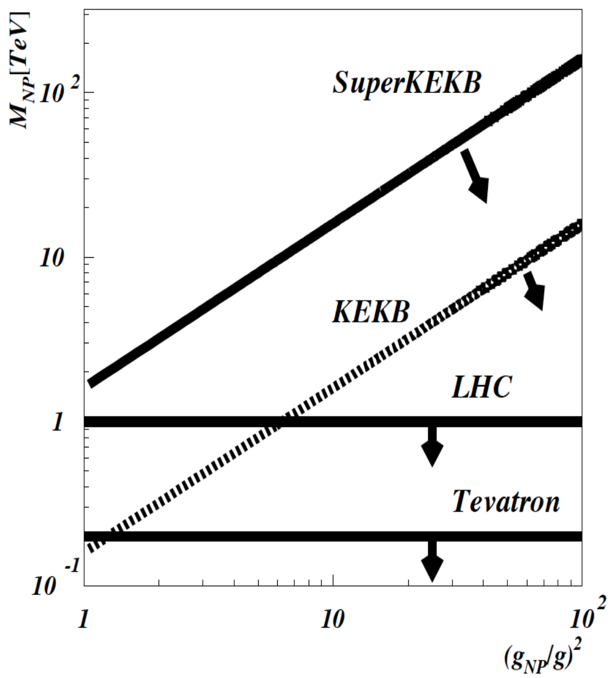

Figure 1.2: Region of sensitivity to new physics as a function of the flavor violating couplings in direct and indirect searches [28].

energy frontier approach. The Higgs bosons play a crucial role in the Standard Model so by precisely studying its properties researchers will be able to establish its exact character and help to understand if there exist any phenomena beyond the Standard Model. To explore the physics beyond the Standard Model, searches are being conducted at the energy frontier to look for supersymmetry (SUSY) particles, dark matter candidates, extra dimensions, and other exotic phenomena predicted by various theories. While this approach provides experimental evidence of new physics, its reach is constrained to the maximum energy available at the collider. The sensitivity to direct production depends on both the cross-section and the size of the data sample.

Unlike the energy and the intensity frontier which focuses on particle collisions in accelerators, the cosmic frontier investigates the universe itself as a natural laboratory. Observations like the bending of light called gravitational lensing [32] and the behavior of supernovae [33] shows that the universe is mostly made up of dark matter and dark energy and only 5% of the universe is known so far. To explore these mysterious dark components, scientists use a combination of underground experiments and telescopes, both on the ground and in space. In recent decades, the cosmic front led to major discoveries including, the universe likely underwent a period of exponential expansion earlier with quantum fluctuations and created the seeds for large-scale structures. The growth of these structures is affected by dark matter and dark energy and the Universe is currently expanding at an accelerating rate [34]. Thus the cosmic frontier approach in high energy physics explores the fundamental properties of the universe and physics beyond the Standard Model by studying cosmic phenomena.

At the intensity approach, the collision rates are increased significantly but with moderate energies. The focus is on the precise measurement of the Standard Model parameters where deviations from the Standard Model predictions offers a hint to the new physics. At the intensity frontier, new physics can be studied at both e^+e^- colliders such as CLEO [35], BABAR [36], BESIII [37], Belle [38] and Belle II [28] as well as at pp colliders such as LHCb [39]. Here, “rare” and “precision” refer to the processes that are strongly suppressed and allowed, respectively in the Standard Model. If the goal of the experiment is precision measurements, the initial state has to be known which is the major drawback of using hadron colliders for precision measurements, because in a hadron collider, quarks and gluons interact which leads to an unknown initial state. Lepton colliders are preferable for precise measurements because leptons are elementary particles that do not have a substructure and due to this nature, the initial state after a collision of two leptons is well known. This is the approach used in B physics experiments and their sensitivity depends on the flavor violating couplings of new physics. The Belle II experiment at the SuperKEKB accelerator [40] explores new physics effects in the Intensity frontier regime. B-factories, including Belle II not only study B decays but also charm and τ lepton physics. Greater sensitivities at Belle II will help to exploit new physics by the constraining measurements in flavor physics studies.

1.2 Flavor physics at Belle II

The Belle II experiment aims to address many questions in flavor physics that could help to explore physics beyond the Standard Model. One of the major areas of focus is to explore CP violation in the quark sector. By studying the differences in the decay rates of B^0 and $\bar{B}^0$ mesons through the measurements in time dependent CP violations in the penguin decays of $b \to d$ and $b \to s$ quarks, Belle II aims to discover new sources of CP violations. Another crucial area of study is the large CP violation observed in the time-integrated rates of charmless hadronic B decays, such as $B \to K\pi$ and $B \to K\pi\pi$. Additionally, the search for CP violation in charm mixing which is negligible in the Standard Model, could provide an understanding of the new phenomena in the up-type quark sector.

The possibility of left-right asymmetry of the nature and existence of flavor changing neutral currents beyond the Standard Model can be explored by measuring time-dependent CP violation in $B \to K^{*0}(\to K_s^0\pi^0)\gamma$ decays, triple-product CP violation asymmetries in $B \to VV$ decays and semi-leptonic decays such as $B \to Vl\nu$, $V = D^*\rho$. Exploring the sources of lepton flavor violation (LFV) beyond the Standard Model is another crucial area for Belle II. Neutrino experiments have found large mixing involving τ neutrinos, raising the possibility of LFV processes such as $\tau \to \mu\nu$. Belle II's unmatched sensitivity to τ decays, due to minimal collision background, enables us to analyze τ leptons for LF and CP violation, as well as measure the electric dipole moment and anomalous magnetic moment of the τ lepton. The Belle II experiment measures CKM matrix elements and their phases with precision and provides a critical understanding of the quark sector. Recent discoveries of many states by B-factories and hadron colliders have changed our understanding of Quantum Chromodynamics in the low-energy regime. The study of quarkonia, which can be produced near resonance by adjusting the machine energy or through initial state radiation is also an important agenda for the Belle II experiment.

Along with the above possibilities, Belle II experiment has a vast charm physics program that offer a significant improvement in understanding the particle physics. There are many decay channels to study direct CP violation in the charm sector. Recently Belle II experiment has provided the most precise measurements of D^0 and D^+ lifetimes [41]. The Belle II experiment's advanced techniques and precise measurements in the charm sector helps to probe the physics beyond the Standard Model.

1.3 Charm Physics

Charm physics provides unique possibilities to explore the strong and weak interactions within and beyond the Standard Model. The charm quark is the second-generation up-type quark of the three generations and ranks the third-heaviest among the six quarks. Charm particles can exist in many forms, from open charm mesons or baryons, containing one or multiple (for baryons) charm quarks to charmonium states which are bound states of charm anti-charm ($c\bar{c}$) quark pairs.

The first observation of the charm quark came with the discovery of J/ψ meson. This also validates the existence of the fourth quark as expected in the GIM mechanism [42] which is the theoretical explanation for the suppression of Flavor Changing Neutral Currents (FCNC). Charm physics plays a crucial role in studying flavor physics in explaining the properties and interactions of quarks and leptons. Through studying the process that involves charm quarks such as the mixing of neutral charm meson ($D^0 - \bar{D}^0$ mixing), CP violations, Flavor changing Neutral Currents (FCNC) or Lepton Flavor Violation (LFV) and precision measurements of decay rates and branching fractions, new physics phenomenon can be explored.

1.3.1 Charm Mixing

When the neutral charm mesons oscillate to their anti-particles before decay, it is known as $D^0 - \bar{D}^0$ mixing or charm mixing. Mixing can occur through the exchange of $W^{\pm}$ bosons, quarks or by the particles beyond the Standard Model. Charm mixing can serve as a valuable tool for probing the physics beyond the Standard Model.

The mass eigenstates of neutral D mesons can be expressed in terms of the flavor eigenstates in the following way:

$$\left|D_{1,2}\right\rangle = p\left|D^0\right\rangle \pm q\left|\bar{D}^0\right\rangle,$$

where p and q are the complex parameters satisfying $|p|^2 + |q|^2$ =1. Additionally, $CP\left|D^0\right\rangle = +\left|\bar{D}^0\right\rangle$, which means in the limit of CP symmetry, $p = q$, $D_{1(2)}$ corresponds to CP-even (odd) eigenstate. The mixing parameters are defined as:

$$x = \frac{m_1 - m_2}{\Gamma} \text{ and } y = \frac{\Gamma_1 - \Gamma_2}{2\Gamma},$$

where, $m_{1,(2)}$ and $\Gamma_{1,(2)}$ represents mass and width of the $D_{1,(2)}$ state and $\Gamma = (\Gamma_1 + \Gamma_2)/2$ denotes the average decay width.

The world average values of the mixing and CP-violation parameters are x = (4.07 $\pm$ 0.44) $\times$ 10^{-3}, y = (6.47 $\pm$ 0.24) $\times$ 10^{-3}, $q/p = 0.994^{+0.016}_{-0.015}$ and arg(q/p) = (-2.6 $\pm$ 1.1)$^{\circ}$. In 2007, the first evidence for charm mixing was established using a combination of results from Belle and BaBar [43]. In 2012, LHCb observed charm mixing in a single experiment by measuring $y \neq 0$ in $D^0 \to K^+\pi^-$ decays [44] which was later confirmed by the Belle experiment using the same decay [45]. Belle II is anticipated to make a significant contribution to these studies and improve the determinations of x.

1.3.2 CP violation in charm

While the experimental evidence of CP violations in the decays of strange and beauty sectors has been firmly established but search to find CP violation charm meson decays is still going on. There is a unique opportunity to explore CP violation in charm hadrons with particles containing only up-type quarks. The size of CP violation in the charm sector is predicted to be very small in the Standard Model and the theoretical predictions are challenging due to the presence of low-energy strong-interaction effects. In 2019, the LHCb observed CP violations for the first time in the decays of $D^0 \to K^- K^+$ and $D^0 \to \pi^- \pi^+$. [46]

In the charm sector, CP violations can be classified into three categories [47]:

1. Direct CP violation: This occurs when the absolute value of the decay amplitude of D meson decays to final state f (A_f) is different from its corresponding CP-conjugated amplitude. Direct CP violation involves the decay amplitudes that are broken at least in the two parts associated with different weak and strong phases,

$$A_f = |A_1| e^{i\delta_1} e^{i\phi_1} + |A_2| e^{i\delta_2} e^{i\phi_2},$$

   where ϕ_i represents the weak phases and under CP transformation, ϕ_i transforms to $-\phi_i$. δ_i represents the strong phase and under CP transformation, δ_i transforms to δ_i. In this way, CP-conjugate amplitude, $A\bar{f}$ is different from A_f.

2. CP violation occurs in $D^0 - \bar{D}^0$ mixing matrix: In this type of CP violation, ΔC

= 2 transitions occur either via the Standard Model or through new physics amplitudes at one loop or tree level that lead to non-diagonal entries in the $D^0 - \bar{D^0}$ mass matrix.

$$\left[M - i\frac{\Gamma}{2}\right]_{ij} = \begin{pmatrix} A & p^2 \\ q^2 & A \end{pmatrix}$$

This CP violation is observed when

$$R_m^2 = |p/q|^2 = \frac{2M_{12} - i\Gamma_{12}}{2M_{12}^* - i\Gamma_{12}^*} \neq 1$$

3. CP violation when there is an interference of decays with and without mixing: This occurs when there is interference between decays with and without mixing for the subset of final states to which both D^0 and $\bar{D^0}$ decays. If f is the final state, then CP violation contributions can be summarized as

$$\lambda_f = \frac{q}{p}\frac{\bar{A}_f}{A_f} = R_m^{i(\phi+\delta)}\left|\frac{\bar{A}_f}{A_f}\right|,$$

Where A_f and $\bar{A}_f$ represent the transition amplitudes for $D^0 \to f$ and $\bar{D^0} \to f$, respectively. δ represents the strong phase difference between A_f and $\bar{A}_f$ and ϕ is the weak phase difference between the ratio of decay amplitudes and the mixing matrix.

The non-diagonal entries of the mixing matrix lead to different mass eigenstates of neutral D meson from the weak eigenstates,

$$\left|D_2^1\right\rangle = p\left|D^0\right\rangle \pm q\left|\bar{D^0}\right\rangle,$$

on diagonalizing the $D^0 - \bar{D}^0$ mass matrix by taking $|p|^2 + |q|^2 = 1$, complex parameters p and q can be obtained. If CP-violations in mixing are neglected then p will be equal to q and $\left|D_{1,2}\right\rangle$ becomes CP eigenstates,

$CP\,|D_{\pm}\rangle = \pm\,|D_{\pm}\rangle$,

$$|D_{\pm}\rangle = \frac{1}{\sqrt{2}}\left[\left|D^0\right\rangle \pm \left|\bar{D}^0\right\rangle\right]$$

1.3.3 Rare Charm decays

Flavor Changing Neutral Currents (FCNC) is a crucial tool for probing the physics beyond the Standard Model. FCNCs only occur at the loop levels because of the flavor structure of the Standard Model allowing to explore the effect that is forbidden at the tree level. In the charm sector, rare decays are primarily mediated by the quark-level FCNC transitions such as $c \to ul^+l^-$ and $c \to u\gamma^*(\gamma^* \to l^+l^-)$. For many years, rare decays have been extensively studied in the down-type quark sector such as in B and K decays. However, FCNCs and rare decay processes have not been much explored in the charm sector. This is because the values of FCNC for the charm hadrons are very small in the Standard Model. Due to the absence of a heavy down-type quark in the charm hadrons, the GIM mechanism is highly effective for these decays because it decouples short-distance contributions in a similar way as the top quark does for B and K decays. This effectiveness has both advantages as well as disadvantages. It allows New Physics effects to be larger than predicted by the Standard Model but also the Standard Model predictions can be strongly influenced by long-distance contributions from the propagation of light quarks. These long-distance contributions are non-perturbative and cannot be calculated precisely using current theoretical methods which leads to large uncertainties in predictions.

The simplest of the rare charm decays are purely leptonic decays such as $D^0 \to l^+l^-$. In the Standard Model, this transition has very small contributions

Int. Luminosity	1 ab^{-1}	5 ab^{-1}	10 ab^{-1}	50 ab^{-1}
$\mathcal{B}_{UL}^{90\%}(D^0 \to \gamma\gamma)(10^{-1})$	8.5	4.9	2.7	1.5

Table 1.4: Expected upper limit on the branching fraction of $D^0 \to \gamma\gamma$ decays as a function of Belle II integrated luminosity [50].

making them a clean probe to explore new physics. Other rare decays such as $D \to \rho\gamma$ have significant Standard Model contributions but these are more difficult to calculate.

The branching fractions for some of these pure leptonic rare charm decays are as follows [48]:

$$B(D^0 \to e^+e^-) < 7.9 \times 10^{-8}$$

$$B(D^0 \to \mu^+\mu^-) < 6.2 \times 10^{-9}$$

$$B(D^0 \to \mu^\pm e^\mp) < 1.3 \times 10^{-8}$$

The rare decay $D^0 \to \gamma\gamma$ involves $c \to u$ transition is also FCNC process that will be studied at Belle II. The Standard Model predicts its branching fraction to be at most 10^{-8} but some extensions of Standard Model suggest this branching fraction can be enhanced by upto 100 times. The current restrictive limit is $\mathcal{B}(D^0 \to \gamma\gamma)$ $< 8.5 \times 10^{-7}$ at 90% confidence level [49], which is about two orders of magnitude higher than the Standard Model prediction. The Belle II experiment will provide an opportunity to search for these rare decays, as listed in Table 1.4, of the charm meson.

1.3.4 Measurement of $\mathcal{B}(D_s^{*+} \to D_s^+\pi^0)/\mathcal{B}(D_s^{*+} \to D_s^+\gamma)$

The decay of strange charm meson, D_s^{*+} is considered one of the important aspects to analyze. Due to the breaking of the flavor symmetry of the quarks, $SU(2)$, the dominating decay modes of D_s^{*+} are the radiative mode $D_s^{*+} \to D_s^+\gamma$ and isospin violating hadronic process $D_s^{*+} \to D_s^+\pi^0$. The study of these decays is important to explore the dynamics of Quantum Chromodynamics and test the theoretical predictions. Different theoretical models predict the branching ratios of these decays. These models include the lattice QCD (LQCD) [51], chiral perturbation theory (χPT) [52], [53], [54], the Nambu-Jona-Lasinio model (NJLM) [55], light-front quark model (LFQM) [56], relativistic quark model (RQM) [57], the QCD sum rules (QCDSR) [58], the nonrelativistic quark model (NRQM) [59] and the covariant model (CM) [60]. These models provide different approaches to understanding the dynamics of the strong interaction and predicting decay rates. Table 1.5 summarizes and compares the theoretical predictions for the partial widths and branching fractions of $D_s^{*+} \to D_s^+\pi^0$ and $D_s^{*+} \to D_s^+\gamma$ along with theoretical uncertainties. These measurements help to constrain the parameters of the theoretical models and contribute to our understanding of the underlying physics.

Precise measurements of these branching fractions are crucial for determining fundamental parameters of the Standard Model, such as the decay constant ($f_{D_s^+}$) of the D_s^+ meson and the Cabibbo-Kobayashi-Maskawa (CKM) matrix element (V_{cs}) describing the transition from a charm quark (c) to a strange quark (s) in weak interactions mediated by the W boson. These parameters are essential for understanding the dynamics of flavor-changing processes in particle physics. The objective of this thesis work is to measure the branching fraction $\mathcal{B}(D_s^{*+} \to D_s^+\pi^0)$ with respect to the $\mathcal{B}(D_s^{*+} \to D_s^+\gamma)$ with the Belle II experiment at SuperKEKB.

Experimental measurements of the branching fractions of D_s^{*+} decays have been performed using data from electron-positron collision experiments; BaBar [61], CLEO [62] and BESIII [63]. Table 1.6 summarizes the results from the measurement of $\mathcal{B}(D_s^{*+} \to D_s^+\pi^0)/\mathcal{B}(D_s^{*+} \to D_s^+\gamma)$ from different experiments. There is a tension between the predictions of the covariant model and the measured results. It would

	$\Gamma[\mathcal{B}]_{(D_s^{*+}\to D_s^+\gamma)}$	$\Gamma[\mathcal{B}]_{(D_s^{*+}\to D_s^+\pi^0)}$	$\mathcal{B}(D_s^{*+}\to D_s^+\pi^0)/\mathcal{B}(D_s^{*+}\to D_s^+\gamma)$
PDG	..[$(94.2 \pm 0.7)\%$]	..[$(5.9 \pm 0.7)\%$]	$(6.2 \pm 0.8)\%$
LQCD [51]	0.066 ± 0.026	–	–
χPT [52]	4.5	–	–
χPT [53]	–	–	$8 \times 10^{-5}/\mathcal{B}(D_s^{*+}\to D_s^+\gamma)$
χPT [54]	–	$0.0081^{+0.0030}_{-0.0026}$	–
NJLM [55]	0.09	–	–
LFQM [56]	0.18 ± 0.01	–	–
RQM [57]	$0.321^{+0.009}_{-0.008}$	–	–
QCDSR [58]	0.25 ± 0.08	–	–
NRQM [59]	0.21	–	–
CM [60]	3.53[$(92.7 \pm 0.7)\%$]	0.277[$(7.3 \pm 0.7)\%$]	$(7.9 \pm 0.8)\%$

Table 1.5: Comparison of theoretical predictions for the decay widths[branching fractions] of $D_s^{*+}\to D_s^+\pi^0$ and $D_s^{*+}\to D_s^+\gamma$ across various models.

Experiment	$\mathcal{B}(D_s^{*+}\to D_s^+\pi^0)/\mathcal{B}(D_s^{*+}\to D_s^+\gamma)$
CLEO [62]	$0.062^{+0.020}_{-0.018}$(stat.) $\pm$ 0.022(syst.)
BaBar [61]	0.062 ± 0.005(stat.) $\pm$ 0.006(syst.)
BESIII [63]	0.062 ± 0.004(stat.) $\pm$ 0.002(syst.)

Table 1.6: Previous results from the measurement of $\mathcal{B}(D_s^{*+}\to D_s^+\pi^0)/\mathcal{B}(D_s^{*+}\to D_s^+\gamma)$ from different experiments.

be interesting to see how the measurements from Belle II compare, as they might provide further insights or constraints on the model's validity and potential refinements. This thesis reports the measurement of branching fraction $\mathcal{B}(D_s^{*+}\to D_s^+\pi^0)$ with respect to the $\mathcal{B}(D_s^{*+}\to D_s^+\gamma)$ using Belle II e^+e^- collision data corresponds to integrated luminosity of 424 fb^{-1}.

1.4 Thesis Organization

This thesis reports the study of charm meson decays using Belle II experiment. Each chapter provides details about experimental setup, data management and research methodologies used in this work. This thesis is organized as follows:

- The current chapter provides an overview of particle physics, Standard Model particles and interactions, highlighting its limitations and beyond Standard Model searches. It discusses different approaches used in experimental high energy physics and also highlights the role of Belle II in new physics searches through precision measurements. This chapter also explores charm mixing, CP violations and rare decays in the charm sector.

- Chapter 2 gives an overview of the experimental setup, providing the details of the SuperKEKB accelerator and its performance compared to its predecessor. This chapter explores the architecture and functionality of the Belle II detector explaining the role of each sub-detector, the trigger system, and the Data Acquisition (DAQ) system.

- Chapter 3 provides a basic overview of data management in the Belle II experiment, including tools and techniques to convert raw data into meaningful quantities for analysis. This chapter also introduces the Belle II framework, discusses simulated data and explains various types of background. All these quantities are crucial for understanding the experimental environment and data analysis methods.

- Chapter 4 focuses on the measurement of branching fraction $\mathcal{B}(D_s^{*+} \to D_s^+\pi^0)$ with respect to the $\mathcal{B}(D_s^{*+} \to D_s^+\gamma)$. This chapter covers the technical details i.e. selection criteria, yield extraction, systematic studies etc. for the measurement of the ratio of the branching fractions using electron-positron collision data collected with the Belle II detector.

- Chapter 5 summarizes the results on the measurement of branching fraction $\mathcal{B}(D_s^{*+} \to D_s^+\pi^0)$ with respect to the $\mathcal{B}(D_s^{*+} \to D_s^+\gamma)$.

Bibliography

[1] J. J. Thomson, "XL. Cathode Rays," *The London, Edinburgh, and Dublin Philosophical Magazine and Journal of Science*, vol. 44, no. 269, pp. 293–316, 1897.

[2] E. Rutherford, "The scattering of alpha and beta particles by matter and the structure of the atom," *Philosophical Magazine Series 6*, vol. 21, pp. 669–688, 1911.

[3] J. Chadwick, "Possible Existence of a Neutron," *Nature*, vol. 129, p. 312, 1932.

[4] M. Gell-Mann, "A schematic model of baryons and mesons," *Physics Letters*, vol. 8, no. 3, pp. 214–215, 1964.

[5] G. Zweig, "An SU(3) model for strong interaction symmetry and its breaking", pp. 22–101. Feb. 1964.

[6] M. E. Peskin and D. V. Schroeder, "An Introduction to quantum field theory". Reading, USA: Addison-Wesley, 1995.

[7] D. Griffiths, "Introduction to elementary particles". Wiley, 2008.

[8] D. H. Perkins, "Introduction to High Energy Physics". Cambridge University Press, 4th ed., 2000.

[9] F. Halzen and A. Martin, "Quarks and Leptones: An Introductory Course in Modern Particle Physics". Wiley, 1984.

[10] S. Chatrchyan et al. (CMS Collaboration), "Observation of a new boson at a mass of 125 GeV with the CMS experiment at the LHC," *Physics Letters B*, vol. 716, pp. 30–61, 2012.

[11] G. Aad et al. (ATLAS Collaboration), "Observation of a new particle in the search for the Standard Model Higgs boson with the ATLAS detector at the LHC," *Physics Letters B*, vol. 716, pp. 1–29, 2012.

[12] P. W. Higgs, "Broken Symmetries and the Masses of Gauge Bosons," *Physical Review Letters*, vol. 13, pp. 508–509, 1964.

[13] W. Marciano and H. Pagels, "Quantum chromodynamics," *Physics Reports*, vol. 36, pp. 137–276, 1978.

[14] S. Weinberg, "A Model of Leptons," *Physical Review Letters*, vol. 19, pp. 1264–1266, 1967.

[15] A. Salam and J. C. Ward, "Electromagnetic and weak interactions," *Physics Letters*, vol. 13, pp. 168–171, 1964.

[16] S. L. Glashow, "Partial-symmetries of weak interactions," *Nuclear Physics*, vol. 22, pp. 579–588, 1961.

[17] M. Bonanomi, "The Higgs Boson and the Standard Model of Particle Physics", pp. 1–20. Cham: Springer Nature Switzerland, 2023.

[18] O. W. Greenberg, "Spin and Unitary-Spin Independence in a Paraquark Model of Baryons and Mesons," *Physical Review Letters*, vol. 13, pp. 598–602, Nov. 1964.

[19] G. Arnison et al. (UA1 Collaboration), "Experimental observation of lepton pairs of invariant mass around 95 GeV/c^2 at the CERN SPS collider," *Physics Letters B*, vol. 126, pp. 398–410, 1983.

[20] P. Bagnaia et al. (UA2 Collaboration), "Evidence for $Z^0 \to e^+e^-$ at the CERN $\bar{p}p$ Collider," *Physics Letters B*, vol. 129, pp. 130–140, 1983.

[21] R. Feynman, "Quantum Electrodynamics". A lecture note and reprint series, Basic Books, 1961.

[22] F. Englert and R. Brout, "Broken Symmetry and the Mass of Gauge Vector Mesons," *Physical Review Letters*, vol. 13, pp. 321–323, 1964.

[23] G. Drexlin et al., "Current Direct Neutrino Mass Experiments," *Advances in High Energy Physics*, vol. 2013, p. 293986, Jan. 2013.

[24] A. D. Sakharov, "Violation of CP Invariance, C asymmetry, and baryon asymmetry of the universe," *Journal of Experimental and Theoretical Physics*, vol. 5, pp. 32–35, 1967.

[25] M. Kobayashi and T. Maskawa, "CP Violation in the Renormalizable Theory of Weak Interaction," *Progress of Theoretical and Experimental Physics*, vol. 49, pp. 652–657, 1973.

[26] S. P. Martin, "A Supersymmetry primer," *Advances in High Energy Physics*, vol. 18, pp. 1–98, 1998.

[27] C. Csaki, "The Minimal supersymmetric standard model (MSSM)," *Modern Physics Letters A*, vol. 11, p. 599, 1996.

[28] T. Abe et al. (Belle II Collaboration), *"Belle II Technical Design Report"*. KEK-REPORT-2010-1, 2010.

[29] S. Chatrchyan et al. (CMS Collaboration), "The CMS Experiment at the CERN LHC," *Journal of Instrumentation*, vol. 3, p. S08004, 2008.

[30] G. Aad et al. (ATLAS Collaboration), "The ATLAS Experiment at the CERN Large Hadron Collider," *Journal of Instrumentation*, vol. 3, p. S08003, 2008.

[31] L. Evans and P. Bryant, "LHC Machine," *Journal of Instrumentation*, vol. 3, p. S08001, 2008.

[32] A. Refregier, "Weak Gravitational Lensing by Large-Scale Structure," *Annual Review of Astronomy and Astrophysics*, vol. 41, pp. 645–668, Sept. 2003.

[33] P. Murdin and L. Murdin, "Supernovae". Cambridge University Press, 1985.

[34] A. S. Chou, "Snowmass Cosmic Frontier Report," 2022. `https://arxiv.org/abs/2211.09978`.

[35] Y. Kubota et al. (CLEO Collaboration), "The CLEO II detector," *Nuclear Instruments and Methods in Physics Research Section A: Accelerators, Spectrometers, Detectors and Associated Equipment*, vol. 320, no. 1, pp. 66–113, 1992.

[36] B. Aubert et al. (BaBar Collaboration), "The BaBar detector," *Nuclear Instruments and Methods in Physics Research A: Accelerators, Spectrometers, Detectors and Associated Equipment*, vol. 479, pp. 1–116, 2002.

[37] M. Ablikim et al. (BESIII Collaboration), "Design and construction of the BESIII detector," *Nuclear Instruments and Methods in Physics Research A: Accelerators, Spectrometers, Detectors and Associated Equipment*, vol. 614, no. 3, pp. 345–399, 2010.

[38] A. Abashian et al. (Belle Collaboration), "The Belle Detector," *Nuclear Instruments and Methods in Physics Research Section A: Accelerators, Spectrometers, Detectors and Associated Equipment*, vol. 479, pp. 117–232, 2002.

[39] P. Perret, "Status and expected performance of the LHCb experiment," *Nuclear Physics B - Proceedings Supplements*, vol. 142, pp. 442–447, 2005.

[40] Y. Ohnishi et al., "Accelerator design at SuperKEKB," *Progress of Theoretical and Experimental Physics*, vol. 2013, p. 03A011, Mar. 2013.

[41] F. Abudinen et al., "Precise Measurement of the D^0 and D^+ Lifetimes at Belle II," *Phys. Rev. Lett.*, vol. 127, p. 211801, Nov 2021.

[42] S. L. Glashow, J. Iliopoulos, and L. Maiani, "Weak interactions with lepton-hadron symmetry," *Physical Review D*, vol. 2, pp. 1285–1292, Oct 1970.

[43] A. Lenz and G. Wilkinson, "Mixing and CP Violation in the Charm System," *Annual Review Of Nuclear And Particle Science*, vol. 71, pp. 59–85, 2021.

[44] R. Aaij et al. (LHCb Collaboration), "Observation of D^0–$\overline{D}^0$ Oscillations," *Physical Review Letters*, vol. 110, p. 101802, 2013.

[45] B. R. Ko et al. (Belle Collaboration), "Observation of D^0–$\overline{D}^0$ Mixing in e^+e^- Collisions," *Physical Review Letters*, vol. 112, p. 111801, 2014.

[46] R. Aaij et al. (LHCb Collaboration), "Observation of *cp* violation in charm decays," *Physical Review Letters*, vol. 122, p. 211803, May 2019.

[47] A. Petrov, "CP violation in charm," *eConf*, vol. C070805, p. 11, 2007.

[48] R. L. Workman et al. (Particle Data Group), "Review of Particle Physics," *Progress of Theoretical and Experimental Physics*, vol. 2022, p. 083C01, 2022.

[49] N. K. Nisar et al. (Belle Collaboration), "Search for the rare decay $D^0 \to \gamma\gamma$ at Belle," *Phys. Rev. D*, vol. 93, p. 051102, Mar. 2016.

[50] L. Aggarwal et al., "Snowmass White Paper: Belle II physics reach and plans for the next decade and beyond," 2022. `https://arxiv.org/abs/2207.06307`.

[51] G. Donald, C. Davies, J. Koponen, and G. Lepage, "Prediction of the D_s^* width from a Calculation of its Radiative Decay in Full Lattice QCD," *Physical Review Letters*, vol. 112, May 2014.

[52] H.-Y. Cheng et al., "Corrections to chiral dynamics of heavy hadrons: SU(3) symmetry breaking," *Physical Review D*, vol. 49, pp. 5857–5881, 1994.

[53] P. Cho and M. B. Wise, "Remarks on $D_s^* \to D_s\pi^0$ decay," *Physical Review D*, vol. 49, pp. 6228–6231, 1994.

[54] B. Yang, B. Wang, L. Meng, and S.-L. Zhu, "Isospin violating decay $D_s^* \to D_s\pi^0$ in chiral perturbation theory," *Physical Review D*, vol. 101, p. 054019, 2020.

[55] Y.-L. Luan, X.-L. Chen, and W.-Z. Deng, "Meson electro-magnetic form factors in an extended Nambu–Jona-Lasinio model including heavy quark flavors," *Chinese Physics C*, vol. 39, p. 113103, Nov. 2015.

[56] H.-M. Choi, "Light-Front Quark-Model Analysis of Heavy-Meson Radiative Decays," *Journal of the Korean Physical Society*, vol. 53, p. 1205–1212, Aug. 2008.

[57] J. L. Goity and W. Roberts, "Radiative transitions in heavy mesons in a relativistic quark model," *Physical Review D*, vol. 64, p. 094007, Oct. 2001.

[58] T. M. Aliev, E. Iltan, and N. K. Pak, "Radiative D^* meson decays in QCD sum rules," *Physics Letters B*, vol. 334, pp. 169–174, 1994.

[59] A. Kamal and Q. Xu, "Total width of the D^*," *Physics Letters B*, vol. 284, no. 3, pp. 421–426, 1992.

[60] C.-Y. Cheung and C.-W. Hwang, "Three symmetry breakings in strong and radiative decays of strange heavy mesons," *Eur. Phys. J. C*, vol. 76, p. 19, Jan. 2016.

[61] B. Aubert et al. (BABAR Collaboration), "Measurement of the branching ratios $\Gamma(D_s^{*+} \to D_s^+\pi^0)/\Gamma(D_s^{*+} \to D_s^+\gamma)$ and $\Gamma(D^{*0} \to D^0\pi^0)/\Gamma(D^{*0} \to D^0\gamma)$," *Physical Review D*, vol. 72, p. 091101, 2005.

[62] J. Gronberg et al. (CLEO Collaboration), "Observation of the isospin-violating decay $D_s^{*+} \to {D_s}^+\pi^0$," *Physical Review Letters*, vol. 75, pp. 3232–3236, 1995.

[63] M. Ablikim et al. (BESIII Collaboration), "Measurement of branching fraction of $D_s^{*+} \to D_s^+\pi^0$ relative to $D_s^{*+} \to D_s^+\gamma$," *Physical Review D*, vol. 107, p. 032011, 2023.

Chapter 2

Experimental Setup

The research outlined in this thesis relies on data samples gathered by the Belle II experiment at the SuperKEKB collider. In this chapter, an overview of the design and construction of the SuperKEKB accelerator and the Belle II experiment is provided.

2.1 SuperKEKB Accelerator

2.1.1 Introduction

SuperKEKB is a circular asymmetric electron-positron collider situated at KEK laboratory in Tsukuba, Japan with a circumference of 3 km [1]. The SuperKEKB is an upgrade of the KEKB collider [2, 3] which operated during 1999-2010.

Figure 2.1 illustrates the schematic configuration of the SuperKEKB accelerator, comprising a linear accelerator and beam storage rings. The electrons are generated by a pulse laser directed on the cathode target, then accelerated to 7 GeV in the linear accelerator (linac) before being injected into a High Energy Ring

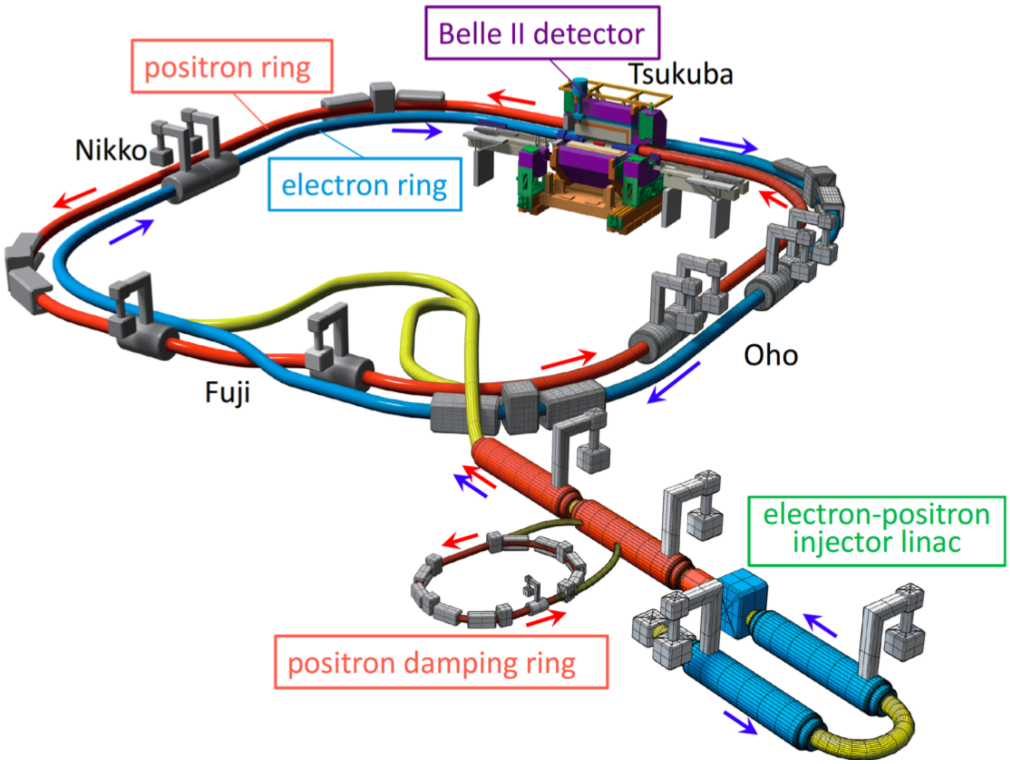

Figure 2.1: Layout view of SuperKEKB asymmetric e^+e^- accelerator situated at KEK laboratory in Tsukuba (Japan). This image shows the linear accelerator where electron and positrons are accelerated, electron ring (HER), positron ring (LER) and the Belle II detector located at the IP of two beams [4].

(HER). Positrons resulting from the collision of electrons with a tungsten target are accelerated to 4 GeV and injected into the Low Energy Ring (LER) of SuperKEKB. These circulating beams collide at the Interaction Point (IP) which is surrounded by the Belle II detector. The area around the IP is designated as the Interaction Region (IR), extending approximately 4 m along the storage rings, where quadrupole magnets facilitate the final focusing of the beams.

With the chosen beam energies, the center-of-mass energy is $\sqrt{s} = \sqrt{4E_{e^+}E_{e^-}}$ $= 10.58$ GeV which is equal to $\Upsilon(4S)$ mass. While the majority of data is collected at this resonance, the flexibility of the beam energies enables tuning the center of mass energy in the small energy regime spanning from the mass of $\Upsilon(1S)$ to $\Upsilon(6S)$. The asymmetry in the energy of electrons and positrons generates a Lorentz boost of $\beta\gamma = 0.28$ in the laboratory frame which helps in vertex determination of short-lived particle decays and increases the detector hermeticity. However, the flight distance of B mesons is reduced from 200 μm to 130 μm compared to KEKB.

Luminosity ($\mathcal{L}$) plays a crucial role in assessing the performance of an experiment. The instantaneous luminosity of a collider can be parametrized as:

$$\mathcal{L} = \frac{\gamma\pm}{2er_e}\left(1+\frac{\sigma_y^*}{\sigma_x^*}\right)\frac{I_\pm\xi_{y\pm}}{\beta_{y\pm}^*}\cdot\frac{R_L}{R_{\xi_y}} \tag{2.1}$$

Here, in the above equation, γ is the relativistic Lorentz factor, e is the elementary electric charge and $r_e = \frac{1}{4\pi\epsilon_0}\frac{e^2}{m_e c^2}$ is the classical radius of the electron. The suffix $\pm$ defines the positron or the electron. R_L and R_{ξ_y} are the reduction factors for the luminosity and the vertical beam-beam parameter, respectively. The ratio of R_L and R_{ξ_y} is closer to the unity. These factors arise from the crossing angle and the hourglass effect. $\sigma_{x,y}^*$, I, β_y^* and ξ_y represent the widths of the bunch at IP on the transverse plane, the beam current, the betatron function at IP and vertical beam-beam parameter at IP, respectively. Additional information regarding the description of parameters can be found in reference [1].

Luminosity mainly depends on three parameters; i.e. the total beam current (I), the vertical beam-beam parameter (ξ_y) and the vertical beta function at the IP (β_y^*). To increase the luminosity at SuperKEKB, larger beam currents and smaller beam dimensions at the IP are used. This is achieved by using the nano-beam scheme [5]. The concept of the nano-beam scheme involves minimizing the vertical betatron function at the IP (β_y^*) while simultaneously minimizing the longitudinal size of the beam overlaps at IP. This approach is implemented through a configuration that utilizes a substantial crossing angle with small horizontal and vertical emittance, as depicted in Figure 2.2.

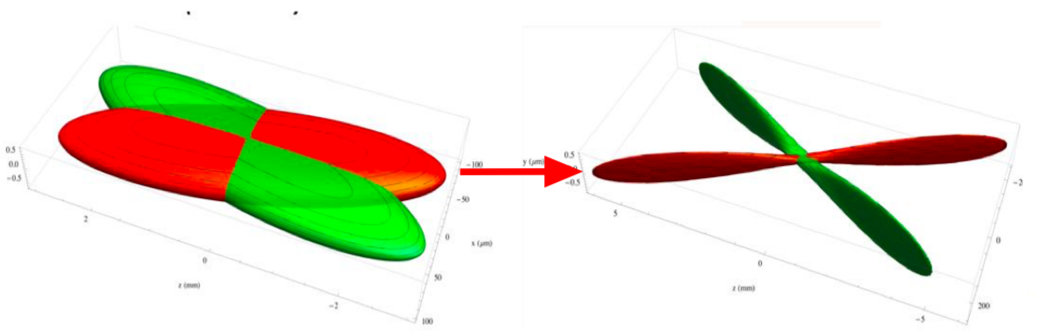

Figure 2.2: Two - dimensional image representing the nano-beam scheme at SuperKEKB (right) as compared to the previous collision scheme at KEKB (left) [4].

The realization of this scheme relies on the superconducting quadrupole magnet system which is made up of magnets, compensation solenoids and corrector coils strategically placed at each longitudinal end of the interaction region. This system results in a 20-fold reduction in the vertical beta function and a doubling of beam currents compared to KEKB, thereby achieving the necessary luminosity. Various modifications have been implemented in the accelerator to enhance luminosity, including adjustments to the electron injection and positron target, the damping ring, the radio-frequency system, optics, the beam pipe and the vacuum system. The target instantaneous luminosity of the SuperKEKB accelerator is 6×10^{35} cm^{-2}s^{-1} a significant improvement over the KEKB accelerator, achieving 30 times greater luminosity. The aim of SuperKEKB is to accumulate 50 times more electron-positron collision data than that of KEKB collider, which collected data corresponding to an integrated luminosity of 1.04 ab^{-1}. Figure 2.3 depicts the luminosity projection plot by end of the year 2035.

The upgrade of SuperKEKB has also led to an increase in beam background by a factor of 10 to 20 compared to KEKB. Single-beam and luminosity-dependent are two types of background in SuperKEKB [7]. Beam backgrounds can originate when the particle of a bunch interacts with residual gas in the beam pipe or with other particles of the same bunch. Luminosity-dependent backgrounds originate during

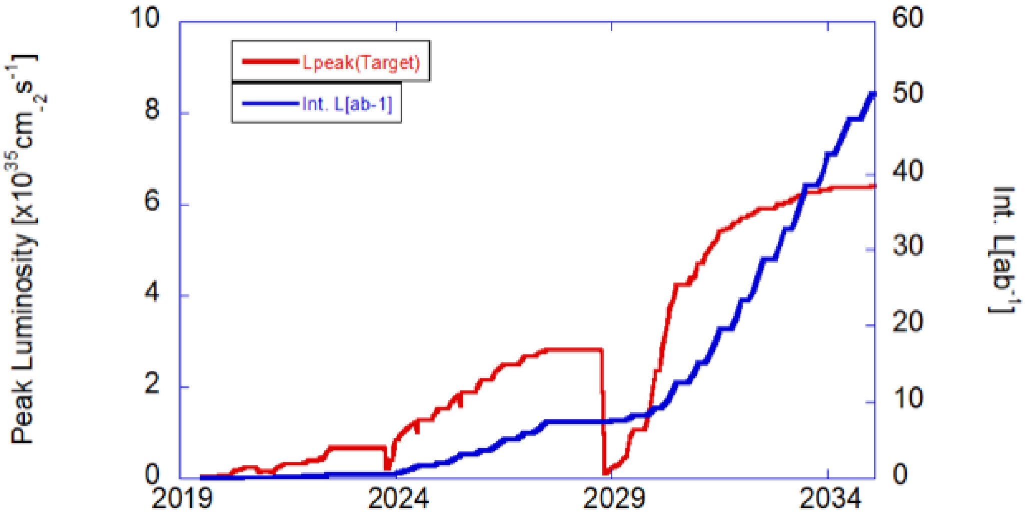

Figure 2.3: Expected projection of instantaneous luminosity delivered by SuperKEKB in red and integrated luminosity in blue, reaching 50 ab^{-1} by end of the year 2035 [6].

beam collisions that include QED processes such as Bhabha scattering $e^+e^- \rightarrow e^+e^-(\gamma)$ or two-photon processes $e^+e^- \rightarrow e^+e^-e^+e^-$. Therefore, it is essential to address the higher background levels to sustain optimal detector performance. The Belle II detector, as briefly discussed in the next subsection, with the SuperKEKB accelerator facility is designed to study the various processes resulting from the electron-positron collisions.

2.2 Belle II Detector

The Belle II detector has been developed as an improvement to the Belle detector [8]. The Belle II detector has a size of 7 m $\times$ 7.5 m which is divided into three acceptance regions: the forward end-cap (FWD), the barrel (BRL) and the backward end-cap (BWD) as illustrated in Figure 2.5. The acceptance region defines the boundaries within which the detector is capable of detecting particles or events. The Belle II detector covers a solid angle equivalent to 91% of 4π, that corresponds to the polar angle of 17^o to 150^o for trackers and extends further for the outer sub-detectors. The Belle II detector is a general-purpose experiment capable of performing efficient tracking of the charged particles, even at low momentum (about 50 MeV/c), precise measurement of γ's energy, separate pions, kaons, protons, electrons and muons over the full kinematic range and it almost covers the full solid angle. The material budget is kept as low as possible to study the low momentum ranges. To deal with the large amount of background in SuperKEKB events, the Belle II detector employs a strategy involving low bias, high-efficiency software and hardware triggers. This approach is achieved by utilizing low track multiplicity, low detector occupancy, and an effective online reconstruction.

Belle II is a hybrid detector with many sub-detectors to efficiently identify and measure different particles originating from electron-positron collisions. Figure 2.4 represents the structure of the Belle II detector and its sub-detectors. The detector exhibits an approximate cylindrical symmetry around the z-axis and notable forward-backward asymmetry to enhance the solid angle acceptance in the boost direction (with the forward direction being the boost direction from the Interaction Point). The Belle II detector consists of multiple sub-detectors as briefly discussed below:

2.2.1 Vertex Detector

The Vertex Detector (VXD) is the innermost sub-detector of the Belle II detector. Two layers of the Pixel Detector (PXD) and four layers of the Silicon Vertex Detector (SVD) form the six-layered VXD. Figure 2.6 represents the geometrical structure of VXD in side and front views. The Pixel detector (PXD) comprises pixelated sensors utilizing DEPFET technology [11], featuring a low material budget that enables the use of very thin sensors (50 microns). The PXD layers are placed at 14 mm and 22 mm from the Interaction Point while the beam pipe radius is about 10 mm. To accommodate the increased hit rate in close proximity to the Interaction Point (IP),

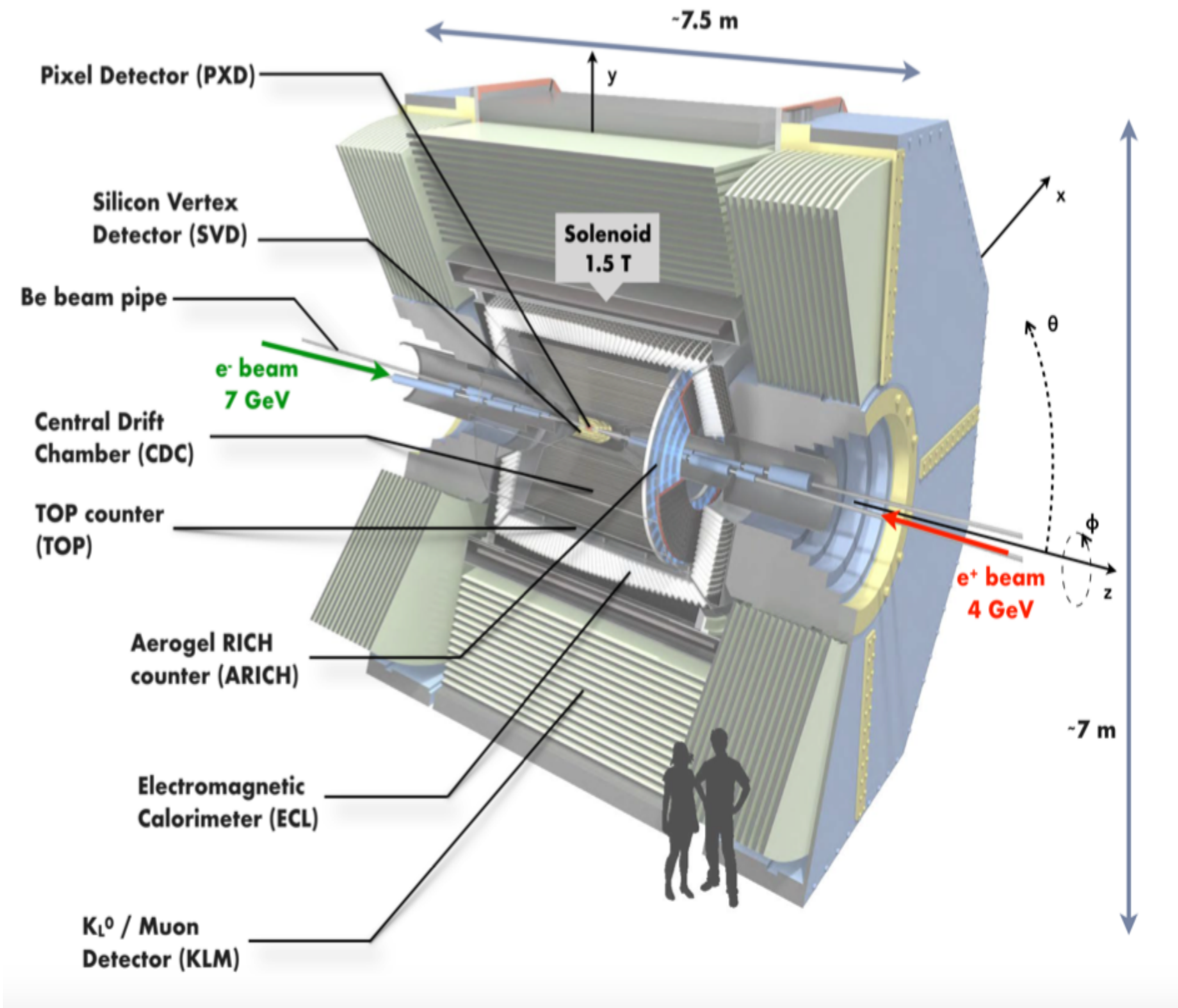

Figure 2.4: Belle II detector and its components [9].

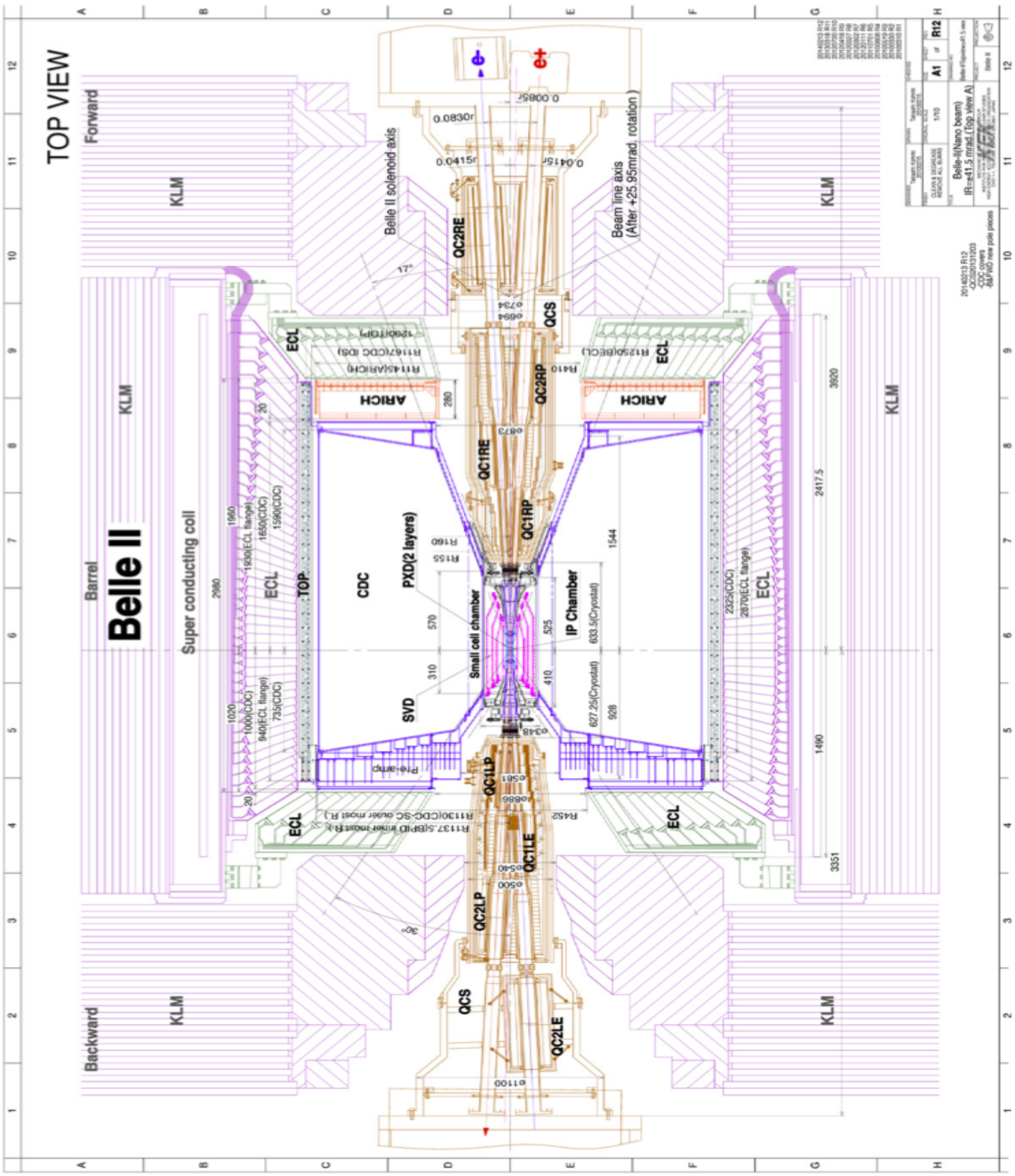

Figure 2.5: Belle II top view [10].

the detector is designed to maintain an occupancy of approximately 3%. Occupancy is defined as the ratio of activated pixels at the same time to the total number of pixels. Pixel detectors prove more advantageous for the innermost layer with low occupancy compared to silicon strip detectors, which experience higher occupancy.

The Silicon Vertex Detector (SVD) is composed of a Double Side Silicon Strip Detector fabricated from six-inch wafers and placed at 38 mm, 80 mm, 115 mm, and 140 mm from the IP. This sensor uses APV25 chips [12], first used in the CMS tracker [13] with a fast sampling shape for the readout of the signal. The polar angular acceptance range of SVD is from 17^o to 150^o and this is asymmetric to take into account the forward boost of the center-of-mass frame. Three types of sensors are used for SVD, out of which two are rectangular and one is trapezoidal. Slanted geometry for the forward sensors is employed to increase the acceptance by reducing the material budget. The SVD incorporates an innovative feature known as the Origami chip-on-sensor concept. This technique is employed to minimize wire connections and streamline cooling. It utilizes a flexible fan-out system to consolidate all readout systems on one side of the module within the detection region. SVD along with PXD provides 2D information which is helpful in the reconstruction of the tracks for B as well as D meson decays. The vertex resolution of Belle II has significantly improved with spatial resolution due to pixel detector layers enhanced by the factor of 2 compared to the Belle experiment. Figure 2.7 illustrates the spatial resolution parameters at the interaction point (in z) of Belle II in comparison to Belle. Furthermore, an increase in the radius coverage of SVD to 135 mm as compared to Belle's configuration, improves the reconstruction of neutral particles such as K_s^0 meson and low momentum particles within SVD itself, which do not reach the outer sub-detectors.

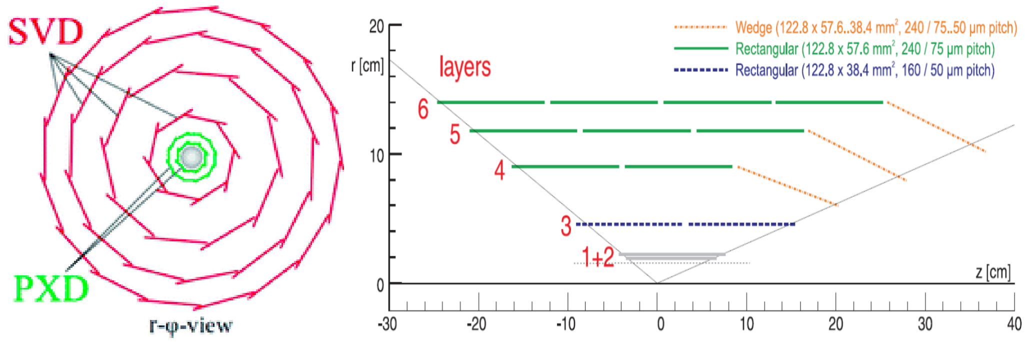

(a) (b)

Figure 2.6: Illustration of the geometric layer structure of VXD, presented in (a) side and (b) front views. The SVD comprises four external layers, while the PXD consists of the innermost two layers. Various sensor types are distinguished by different colors. The beampipe is depicted with a dashed line, and dotted lines in the side view emphasize the angular acceptance of VXD [5].

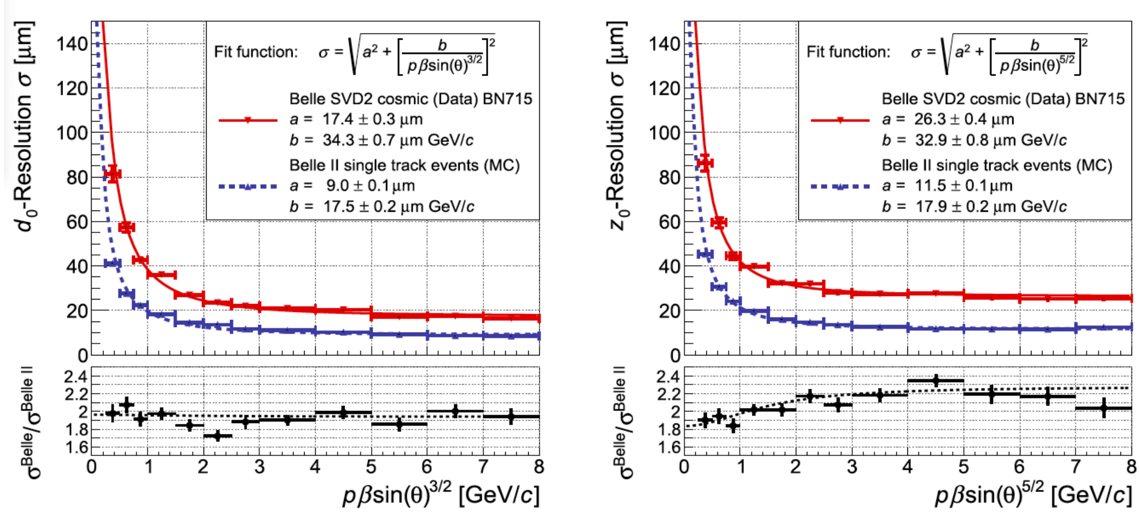

Figure 2.7: Parameters for the spatial resolution of the interaction point (in z) of Belle II compared to Belle [5].

	Belle	Belle II
Radius of inner cylinder (mm)	77	160
Radius of outer cylinder (mm)	880	1130
Number of layers	50	56
Number of sense wires	8,400	14,336
Gas	H_e-C_2H_6	H_e-C_2H_6

Table 2.1: Comparison of main parameters of the Belle CDC and the Belle II CDC.

2.2.2 Central Drift Chamber

The Central Drift Chamber (CDC) is the central tracking device and the large volume wire drift chamber is placed outside the SVD. The main feature of the CDC is to allow the reconstruction of the full 3D helix track and provide precise momentum of the particle. The CDC also helps in providing Particle Identification (PID) information by measuring specific-ionization energy loss (dE/dx) in the gas volume of the chamber.

The CDC has 9 super layers, out of which each 8 super layers are made of six layers of wires and the innermost super layer of CDC is made of eight layers of wires. The CDC structure is filled with 50% of Helium (He) and 50% of Ethane (C_2H_6) gases providing adequate drift velocity and good energy loss resolution. The wires of the CDC are of two types: one, the field wires that produce the accelerating electric field and the second one is the sense wires that collect the released charges. The field wires are made up of aluminum and have 126 μm in diameter while the sense wires are composed of gold-plated tungsten and are thinner than field wires with 30 μm in diameter.

The geometrical acceptance of the CDC is the same as that of the vertex detector ($17^o < \theta < 150^o$). Over the past decades, Belle's CDC had demonstrated excellent performance so there is not much change in the global structure of the Belle II CDC. Table 2.1 provides a comparison of mechanical parameters between the Belle CDC and the Belle II CDC.

The Belle II CDC features a radius extension of 22% more compared to Belle

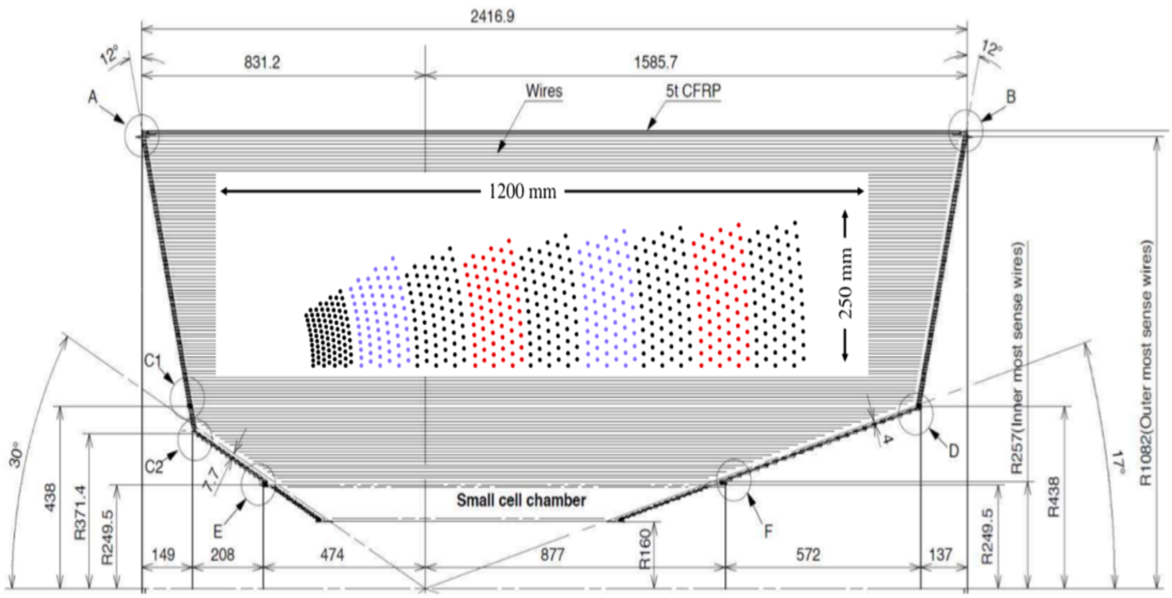

Figure 2.8: Radial (r - z) cross-section of the CDC with an additional r - ϕ section providing insight into the wire configuration [14].

CDC leads to a 5% improvement in the momentum and the dE/dx resolution of CDC. The spatial resolution of CDC on individual hits is about 100 μm while the dE/dx resolution of CDC is around 11.9% for particles with $\theta \sim \pi/2$. Moreover, the number of wires in the CDC has nearly doubled as compared with Belle, enhancing performance in the high luminosity environment and improving the signal to noise ratio. In addition, the readout electronics of Belle CDC have been completely replaced to handle the higher trigger rates with reduced dead time. The introduction of faster readout electronics decreases the dead time from 1-2 μs to 200 ns. Figure 2.8 represents the r - z and r - ϕ cross-sectional structure of the CDC sub-detector.

2.2.3 Particle Identification Devices

In Belle II, the particle identification is composed of two separate devices based on the Cherenkov light detection: the Time of Propagation (TOP) detector in the barrel region and the Aerogel Ring Imaging Cherenkov (ARICH) detector in the forward endcap region. While both detectors are based on Cherenkov light detection, their operating principles differ. The underlying concept for these detectors is that when a charged particle traverses the radiator material, it emits Cherenkov photons. By measuring the angle θ_c of the photons one can determine the particle's β using the following relation:

$$cos\theta_c = \frac{1}{n\beta},$$

where, n is the refractive index of the radiator material. In Belle II, the mass of the particle is determined by combining the momentum measured in the tracking system and the measured β value with energy loss measured in CDC.

The particle identification devices are completely new from the Belle experiment. The material budget of these devices has been reduced due to the expansion in the CDC radius. These detectors are more tolerant to the increase in background level contributing to an overall better performance. They achieved $K(\pi)$ efficiency $> 90\%$ with $\pi(K)$ fake rate $< 10\%$ compared to Belle's 88% efficiency.

2.2.3.1 Time of Propagation Counter

Figure 2.9 represents the structure of the TOP detector. A single TOP module consists of the quartz bar with a focusing mirror and an array of photomultiplier tubes (PMT) in the forward and backward regions, respectively.

In the TOP detectors, the angle θ_c is obtained from the combined information of the time of arrival of Cherenkov photons t_{TOP}, the angle of Cherenkov cone ϕ, the direction of the particle and the impact position of Cherenkov photons at the photodetector at one end quartz bar. Complete details of the operating principle can be found in reference [15].

In the quartz bar of the TOP detector, the emitted photons are reflected internally and after that they reach the focusing mirror located at the forward region. The function of the focusing mirrors is to preserve the information of the angle ϕ and also helps to reflect the photons to specific PMT that measure t_{TOP}. Thus, the measurement of the angle ϕ depends on the activated channel of the PMT. Photons that are emitted in the backward directions are first reflected by the mirror present at the end of the bar and then these are directed to the focusing mirror.

In the TOP detector, the quartz radiators are arranged in 16 modules around the CDC with a radius of 1.2 m from the IP. The geometrical acceptance of the TOP detector is $31^o < \theta < 128^o$. The dimensions of the quartz bar are 0.45 m $\times$ 0.02 m $\times$ 2.75 m. The TOP detector has a time resolution lower than 50 ps, which means that the detector can distinguish between pions and kaons with a photon arrival time difference of about 100 ps at 2 GeV/c. For the K/π separation, the efficiency of the TOP detector is about 85% with a 10% pion misidentified rate [16].

2.2.3.2 Aerogel Ring-Imaging Cherenkov counter

The ARICH is a proximity focusing Ring-Imaging detector located at the forward endcap region where the ring of aerogel is used as the radiator. The structure of the ARICH is represented in the Figure 2.10. The ARICH plays a crucial role in distinguishing between kaons and pions across a broad momentum range and in differentiating muons, electrons, and pions for momenta below 1 GeV/c^2.

In ARICH the radiators are made of silica aerogel which is highly transparent to minimize the photon loss that occurs due to Rayleigh scattering or absorption. Two separate layers of aerogels with 20 mm thickness with refractive indices of 1.045 and 1.055 are used in ARICH. The specific values of refractive indices are chosen so that the Cherenkov rings that are produced in these layers can overlap each other on the detection plane. It incorporates an array of position-sensitive photon detectors called Hybrid Avalanche Photo Detectors (HAPD), which are read by integrated cir-

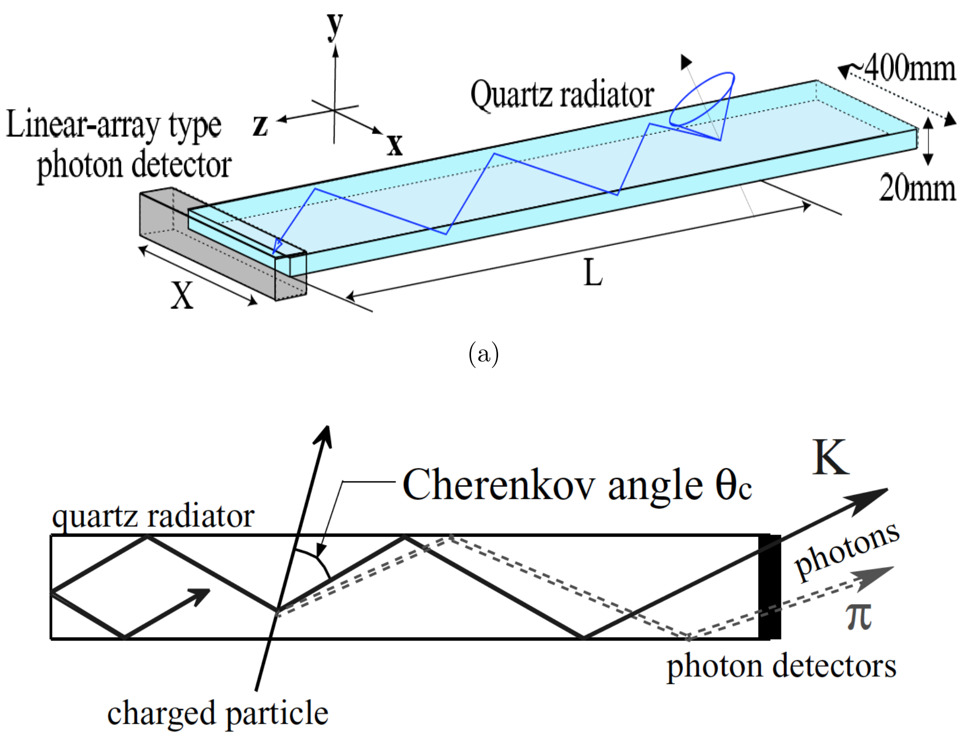

(a)

(b)

Figure 2.9: Illustration of (a) Schematic representation of a TOP radiator element and (b) Side-view representing the operational principle of the TOP counter [10].

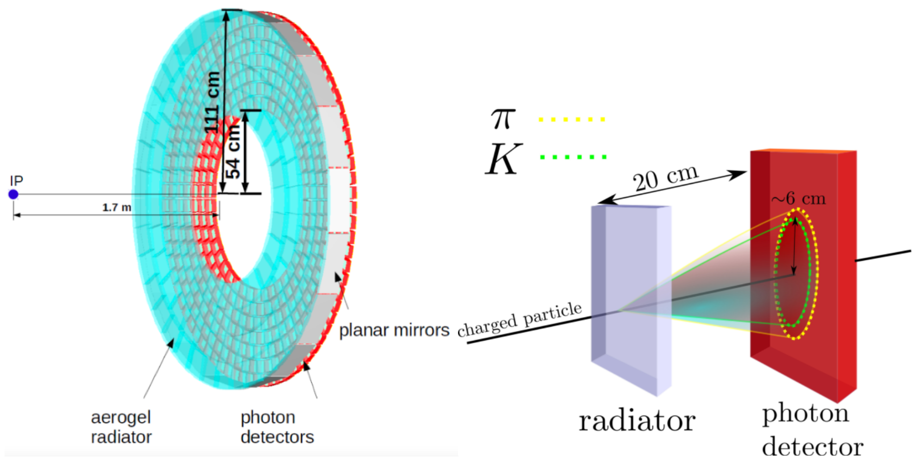

(a) (b)

Figure 2.10: Illustration of the (a) Schematic depiction of the ARICH detector, highlighting its key characteristics and (b) Operational principle of the ARICH [18].

cuit chips. These detectors capture photons generated after traversing an expansion volume of 20 cm, offering excellent 2D resolution and high efficiency. The angular acceptance region of the ARICH lies between $15^o < \theta < 30^o$. The separation efficiency for distinguishing kaons from pions using the ARICH is approximately 93%, with a pion misidentification rate of about 10% [17].

2.2.4 Electromagnetic Calorimeter

The Electromagnetic Calorimeter (ECL) plays several crucial roles in the Belle II. First of all, is the detection of the photons in the wide energy range ($2 \times 10^{-2} \sim 4$ GeV) and efficiently measuring their energy and angle. It also contributes to the identification of electrons and helps in the identification of K_L^0 with KLM sub-detectors. In addition, the online and offline luminosity of the SuperKEKB detector is also monitored by ECL. The ECL also generates software and hardware photon triggers.

The crystal configuration of Belle II ECL remains the same as that of the Belle calorimeter. The forward, backward and barrel region are three regions in which ECL is divided which almost covers 90% of the solid angle in the center-of-mass system. The angular acceptance range of ECL is $12.4^\circ < \theta < 155.1^\circ$. The inner radius of the barrel region is 1.25 m with an extension of 3 m. z = 1.96 m and z = -1.02 m are the values of the internal base from IP for the forward and backward endcap regions, respectively. A gap of 1° exists on both sides between the barrel and the endcaps regions to facilitate the passage of cables for internal sub-detectors [19]. Figure 2.11 represents the structure of ECL showing three regions of the sub-detector.

The ECL constitutes a uniform and extensively segmented calorimeter, comprised of 8736 CSI(Tl) crystals (Cesium Iodide Thallium-doped). These crystals are of truncated pyramid shape, measuring 30 cm in length with a base area of 6×6 cm ^{2}, corresponding to 16.1 radiation lengths (X_0). The crystals are organized into 8 cells, separated by 0.5 mm thick aluminum septum walls and enclosed by two cylinders. Each cell ensures an optimal operating environment for the crystals in terms of humidity and temperature through a dry air flushing and water cooling system.

Hamamatsu Photonics s2744-08 photodiodes, with dimensions 10×20 mm^2, are affixed to the external bases of the crystals using a 1 mm plexiglass plate. These photodiodes collect light emitted by the scintillating material. To monitor optical stability, each photodiode is equipped with a LED that injects light pulses into the crystal volume.

The relatively long decay time of CSI(Tl) (~ 1 μs) along with the higher background levels in the Belle II increase the overlapping of the pulses from the neighboring events. While the Belle's readout electronics were designed to handle a 300 Hz trigger rate, the Belle II operates at a 100 times higher rate. To mitigate the challenge of a large pile-up background, waveform sampling together with pipelined readout has been employed. Waveform sampling helps discriminate off-timing hits using timing information, while pipelined readout effectively eliminates

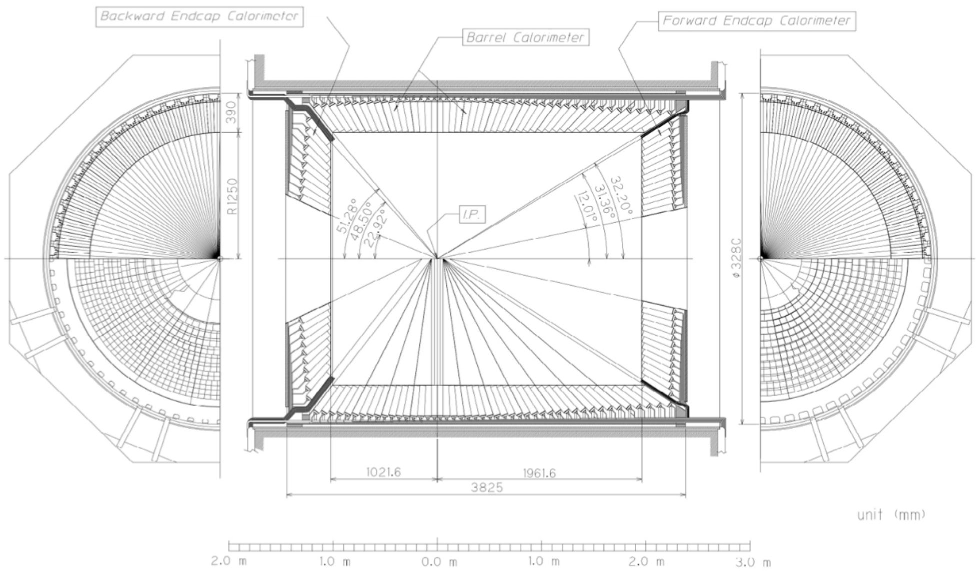

Figure 2.11: Schematic representation of the ECL detector, delineating the three regions: barrel and both endcap regions [21].

readout dead time. This new "Shaper-DSP board" shortens the shaping time to 0.5 μs from 1 μs.

When the cosmic muons pass through the crystals, the crystals produce an average signal of around 5000 photoelectrons for each MeV of energy deposited by the muons with the noise level of the crystals is approximately 200 keV. The intrinsic energy resolution of ECL using prototype test [20] is given as:

$$\frac{\sigma_E}{E} = \sqrt{\left(\frac{0.066\%}{E}\right)^2 + \left(\frac{0.81\%}{\sqrt[4]{E}}\right)^2 + (1.34\%)^2}$$

with E is the energy in GeV. In Belle experiment, the energy resolution observed with ECL was $\sigma_E/E = 4\%$ at 100 MeV, 1.6% at 8 GeV, and the angular resolution was 13 mrad (3 mrad) at low (high) energies. The π^0 mass resolution was 4.5 MeV/c^2. Belle II aims to achieve a similar performance in the absence of backgrounds.

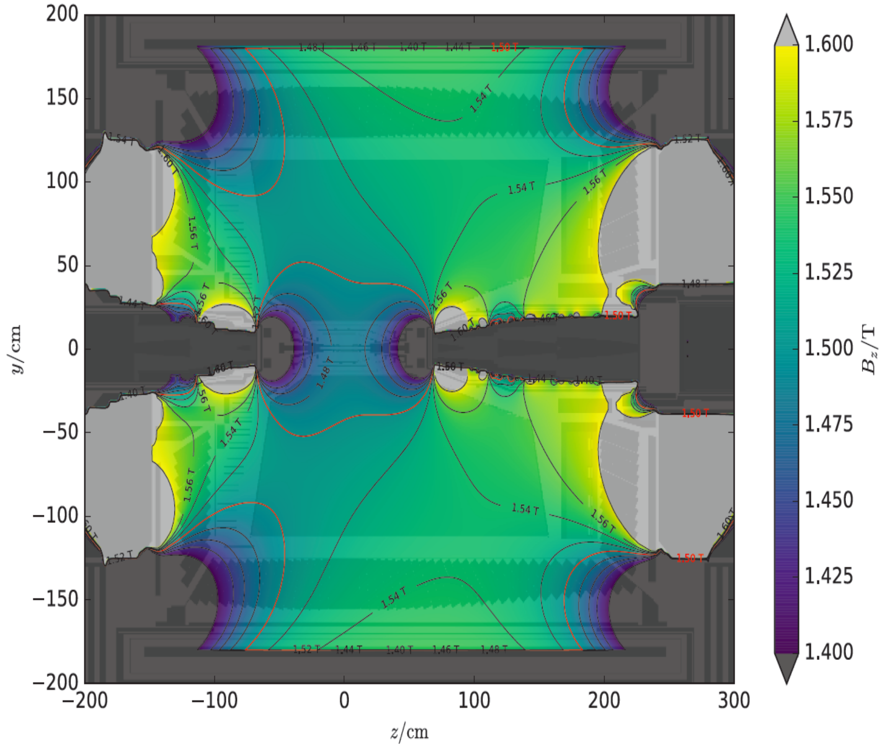

Figure 2.12: Representation of map of magnetic field used in Belle II software [10].

2.2.5 Magnet

In Belle II, the homogenous magnetic field of 1.5 T, aligned parallel to the beam direction, is generated by a superconducting coil within a cylindrical volume. The superconducting coil, composed of NbTi/Cu alloy, measures 4.4 m in length and 3.4 m in diameter. A liquid helium cryogenic system and a current of 4400 A are used to operate the coil. Since the KLM has an iron structure it provides a return yoke to the magnetic field and the direction of the magnetic field is inverted in the KLM region lies outside the coil.

Commercial Hall sensors are used to map the magnetic field with a precision of 0.1%. Figure 2.12 represents the field map used in Belle II software, *basf2* [22]. The edge effects and the final focus system magnets of the accelerator create some inhomogeneities in the field.

2.2.6 Kaons and Muons System

The Kaons and Muons system, KLM, is made by alternating iron plates and the active material detector and located outside of the superconducting coil. The barrel region of KLM lies in the range $45^o < \theta < 125^o$ while the endcaps of KLM have a range of $\theta = 20^o$ to $\theta = 155^o$. There are 15 iron plates and 15 detector layers in the barrel region while there are 14 iron plates and 14 detector layers in the endcap region [23]. The thickness of iron plates is about 4.7 cm and provides the magnetic flux return for the solenoid. They provide a 3.9 interaction length (λ_0) along with 0.8 λ_0 of the ECL, in which K_L^0 mesons can shower hadronically.

Muon tracks in the KLM detector can be identified by measuring the penetration depth in the iron. In the KLM detector, the long-lived kaons can be reconstructed with the help of combined information from the ECL and the hadronic KLM showers.

In the barrel region, Resistive Plate Chambers (RPC) are chosen as the detector layers. RPC is a proportional gas chamber that is used in the steamer mode and a dielectric plate is inserted between the electrodes which helps to prevent the propagation of sparks and increase the spatial resolution. Metallic strips which are present on one side of the chamber are used to read the signal. The coupled RPC with orthogonal strips configuration along with an independent power supply made the KLM module; this pair of RPC is known as the super layer of the KLM. Figure 2.13 represents the structure of RPC super layer.

In the barrel region, the same detector layers and iron structure employed in the Belle experiment are utilized, as the event rate remains sustainable despite an increased luminosity. In the innermost barrel superlayer and the endcap region of the KLM, two orthogonal layers of scintillator strips, coupled with silicon photomultipliers, replace the RPCs. This substitution is made because the RPCs introduce

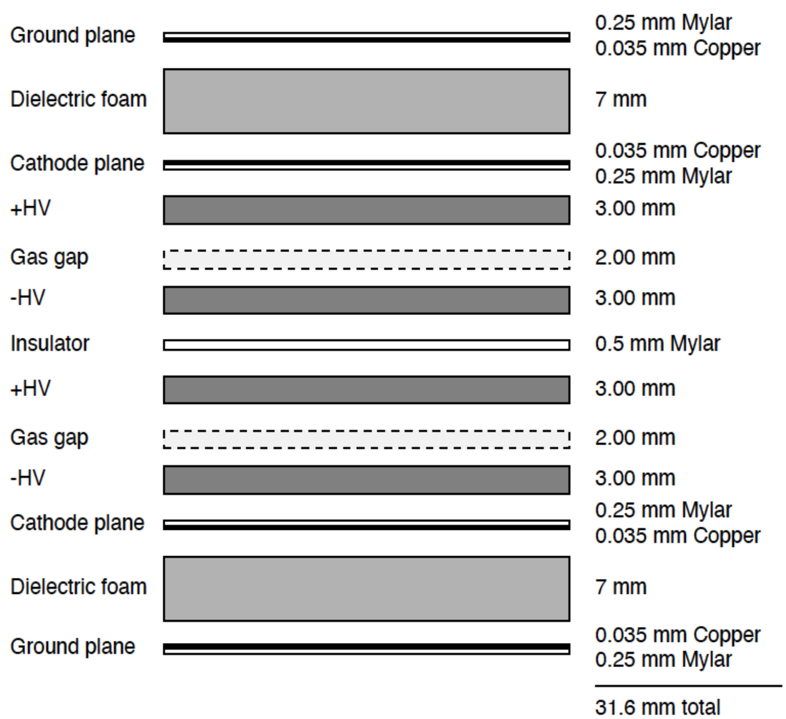

Figure 2.13: Cross-sectional view of an RPC super layer. A KLM module comprises two super layers on each side of an iron plate [10].

excessive dead time in this area, posing challenges in maintaining the background rate.

For tracks with a momentum above 1 GeV/c, the muon detection efficiency stands at approximately 89%, with a hadron fake rate of 1.3%. Regarding K_L^0, the detection efficiency is around 80% for momenta above 3 GeV/c, gradually decreasing linearly for lower momentum ranges.

2.2.7 Trigger System

The Belle II trigger system helps in selecting the events of interest and rejecting the background from Bhabha scattering and intra-beam scattering. Several requirements need to be satisfied so that the system performs adequately at the SuperKEKB luminosity. It should be capable of handling the data acquisition load by limiting the trigger rate to 30 kHz to accommodate the expected collision rate at nominal luminosity. Also, trigger should have $\sim 100\%$ efficiency to select hadronic events from $\Upsilon(4S) \rightarrow B\bar{B}$ and $e^+e^- \rightarrow q\bar{q}$. In addition to this, timing precision needs to be better than 10 ns and at least 200 ns of the minimum separation power between two events is required.

The Belle II trigger system follows the same scheme as the Belle detector but all the components have been replaced to take care of the increased event rate. The trigger system is subdivided into two main stages: one is hardware based level 1 (L1) that uses detector level information to remove the background and the second one is software based High Level Trigger (HLT) that uses reconstructed event information to reduce the data.

2.2.7.1 Level 1 trigger

The L1 trigger serves the purpose of rejecting background events and selecting events of interest by extracting raw data from the Belle II sub-detectors through sub-trigger systems. This information undergoes processing by a Global Reconstruction Logic (GRL), which conducts a low-level reconstruction and transmits its results to a centralized Global Decision Logic (GDL), responsible for making the final decision. Each component of the L1 is equipped with a Field Programmable Gate Array (FPGA) that facilitates the configuration of trigger logic.

At the core of the L1 trigger system is the CDC sub-trigger, providing details on charged tracks, and the ECL sub-trigger, associated with energy clusters in the calorimeter. The CDC sub-trigger incorporates a 2D trigger based on track reconstruction in the (x, y) plane, followed by a 3D trigger that estimates the z coordinate of the event's primary vertex. This enables the rejection of machine background contributions originating away from the interaction point (IP). Meanwhile, the ECL sub-trigger generates rapid signals based on the total energy deposited in the calorimeter and the number of clusters for events involving both charged and

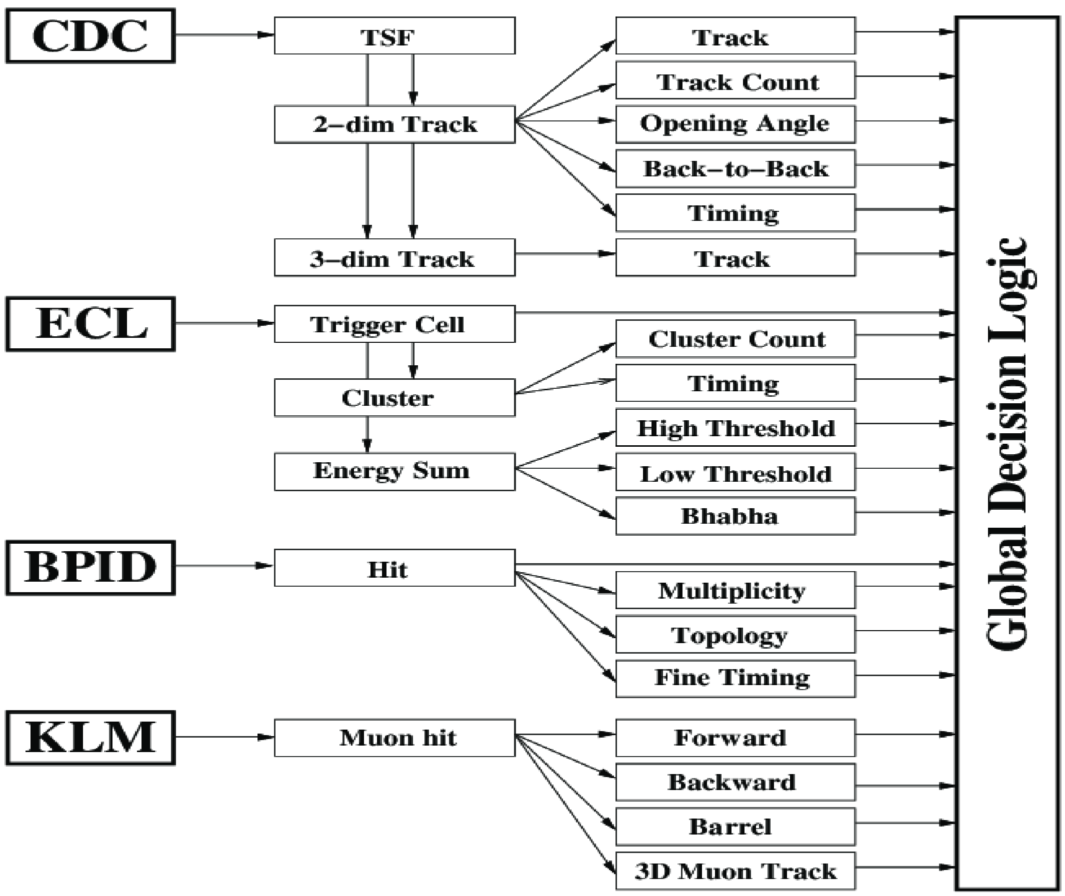

Figure 2.14: Overview of the L1 trigger, where the outputs from various sub-systems are transmitted to the GDL, which ultimately determines the final trigger decision [24].

neutral particles. The trigger signals from CDC and ECL are merged with information from the KLM and TOP by the GRL and then transmitted to the GDL, which makes a trigger decision based on the combined output from the various sub-systems as represented in Figure 2.14.

2.2.7.2 High Level Trigger (HLT)

The High-Level Trigger (HLT) relies on a real-time reconstruction of the event using information from all detectors except PXD. To maintain consistency and avoid introducing additional systematic uncertainties, the reconstruction software employed is the same that utilized for offline reconstruction as well.

Operated on a dedicated server farm, the software trigger makes the final decision to store or discard events based on event topology. Additionally, the physics trigger facilitates the classification of events into categories (e.g., hadronic events, low multiplicity), enabling the restriction of collected data to the processes of interest.

Due to the substantial number of pixels in the PXD, performing a full readout for each event is impractical. A tenfold reduction in PXD data is necessary before combining it with other sub-systems. To achieve this, the HLT extrapolates information from the CDC and SVD to define Regions of Interest (ROIs) within the PXD, where particle hits are then recorded.

2.2.8 Data Acquisition (DAQ) System

Upon the Level-1 (L1) trigger decision provided by the trigger system, the detector signals can be retrieved using the Data Acquisition (DAQ) system. This system facilitates the transfer of data from the front-end electronics, and after undergoing various data processing steps, the information is ultimately transmitted to the storage system. The primary components of the data flow include the Belle2Link, serving as the unified data link, the event builder system, the Common Readout Platform known as COPPER, and the High-Level Trigger (HLT) system.

The Belle II DAQ is specifically designed to handle trigger rates of up to 30 kHz. This value is estimated based on the full luminosity and takes into account both beam-related background and all physics processes.

2.3 Chapter in a Nutshell

This chapter provides an in-depth focus on the SuperKEKB accelerator. An overview of the accelerator's performance in comparison to its predecessor is presented. The innovative Nano Beam scheme, a key feature to increase luminosity in SuperKEKB is discussed in details.

Subsequently, the chapter digs into the detailed architecture and functionality of the Belle II detector. Working of each sub-detector and their role in collecting data is explained. Also, the trigger system and methodology employed to identify and select events of interest are discussed. The Data Acquisition (DAQ) System, a critical component in the data collection process, is thoroughly examined. Together, these components constitute the robust experimental setup that forms the foundation for the subsequent physics analysis.

Bibliography

[1] Y. Ohnishi et al., "Accelerator design at SuperKEKB," *Progress of Theoretical and Experimental Physics*, vol. 2013, p. 03A011, Mar. 2013.

[2] S. Kurokawa and E. Kikutani, "Overview of the KEKB accelerators," *Nuclear Instruments and Methods in Physics Research Section A: Accelerators, Spectrometers, Detectors and Associated Equipment*, vol. 499, pp. 1–7, 2003.

[3] A. J. Bevan et al., "The physics of the B factories," *The European Physical Journal C*, vol. 74, Nov. 2014.

[4] K. Akai et al. (SuperKEKB Collaboration), "SuperKEKB collider," *Nuclear Instruments and Methods in Physics Research Section A: Accelerators, Spectrometers, Detectors and Associated Equipment*, vol. 907, pp. 188–199, Nov. 2018.

[5] E. Kou et al., "The Belle II physics book," *Progress of Theoretical and Experimental Physics*, vol. 2019, Dec. 2019.

[6] P. Krizan, "The Belle II Upgrade Program," *Proceedings of Science*, vol. ICHEP2022, p. 355, Nov. 2022.

[7] P. Lewis et al., "First measurements of beam backgrounds at SuperKEKB," *Nuclear Instruments and Methods in Physics Research Section A: Accelerators, Spectrometers, Detectors and Associated Equipment*, vol. 914, pp. 69–144, Jan. 2019.

[8] A. Abashian et al. (Belle Collaboration), "The Belle Detector," *Nuclear Instruments and Methods in Physics Research Section A: Accelerators, Spectrometers, Detectors and Associated Equipment*, vol. 479, pp. 117–232, 2002.

[9] D. Matvienko, "The Belle II experiment: status and physics program," *EPJ Web of Conferences*, vol. 191, p. 02010, Jan. 2018.

[10] T. Abe et al. (Belle II Collaboration), *"Belle II Technical Design Report"*. KEK-REPORT-2010-1, 2010.

[11] J. Kemmer et al., "Low capacity drift diode," *Nuclear Instruments and Methods in Physics Research Section A: Accelerators, Spectrometers, Detectors and Associated Equipment*, vol. 253, no. 3, pp. 378–381, 1987.

[12] M. J. French et al., "Design and results from the APV25, a deep sub-micron CMOS front-end chip for the CMS tracker," *Nuclear Instruments and Methods in Physics Research Section A: Accelerators, Spectrometers, Detectors and Associated Equipment*, vol. 466, no. 2, pp. 359–365, 2001.

[13] S. Chatrchyan et al. (CMS Collaboration), "The CMS Experiment at the CERN LHC," *Journal of Instrumentation*, vol. 3, p. S08004, 2008.

[14] T. Bilka et al., "Simultaneous Global and Local Alignment of the Belle II Tracking Detectors," *EPJ Web of Conferences*, vol. 251, p. 03028, 2021.

[15] M. Akatsu et al., "Time-of-propagation Cherenkov counter for particle identification," *Nuclear Instruments and Methods in Physics Research Section A: Accelerators, Spectrometers, Detectors and Associated Equipment*, vol. 440, pp. 124–135, 2000.

[16] K. Kojima, "The operation and performance of the TOP detector at the Belle II experiment," *Proceedings of Science*, vol. EPS-HEP2021, p. 803, 2022.

[17] M. Yonenaga et al., "Performance evaluation of the aerogel RICH counter for the Belle II spectrometer using early beam collision data," *Progress of Theoretical and Experimental Physics*, vol. 2020, p. 093H01, 2020.

[18] K. Uno, "Operation and performance of the Belle II Aerogel RICH detector," *Nuclear Instruments and Methods in Physics Research Section A: Accelerators, Spectrometers, Detectors and Associated Equipment*, vol. 1056, p. 168635, 2023.

[19] V. Aulchenko et al., "Electromagnetic calorimeter for Belle II," *Journal of Physics: Conference Series*, vol. 587, p. 012045, Feb. 2015.

[20] H. Ikeda et al. (Belle Collaboration), "A detailed test of the CsI(Tl) calorimeter for BELLE with photon beams of energy between 20 MeV and 5.4 GeV," *Nuclear Instruments and Methods in Physics Research Section A: Accelerators, Spectrometers, Detectors and Associated Equipment*, vol. 441, no. 3, pp. 401–426, 2000.

[21] I. Adachi et al., "Detectors for extreme luminosity: Belle II," *Nuclear Instruments and Methods in Physics Research Section A: Accelerators, Spectrometers, Detectors and Associated Equipment*, vol. 907, pp. 46–59, 2018.

[22] N. Braun et al., "The Belle II Core Software," *Computing and Software for Big Science*, vol. 3, Nov. 2018.

[23] T. Aushev et al., "A scintillator based endcap K_L and muon detector for the Belle II experiment," *Nuclear Instruments and Methods in Physics Research Section A: Accelerators, Spectrometers, Detectors and Associated Equipment*, vol. 789, pp. 134–142, 2015.

[24] Y. Iwasaki, B. Cheon, E. Won, and G. Varner, "Level 1 Trigger System for the Belle II Experiment," *IEEE Transactions on Nuclear Science*, vol. 58, pp. 1–9, 06 2010.

Chapter 3

Dataset, Reconstruction and Analysis Overview

For this research, it is essential to have the knowledge and tools to effectively handle, process and analyze the data from the Belle II experiment. This chapter provides an overview of the data management in the Belle II experiment and tools and techniques to convert raw data into meaningful quantities for the analysis. Additionally, it introduces the Belle II framework, discusses simulated data and explains various types of backgrounds, all of which are crucial for understanding the experimental environment and data analysis methods.

The data analysis involves a number of steps, starting from the data collection, processing and generating corresponding simulated events. Figure 3.1 represents the experimental framework from the data collection to data analysis. Starting from the end, it is evident that the analysis is input by reconstructed and skimmed events either from the real data or from the generation of simulated events. Skimming is used to reduce the dataset's size so that the analysis process can be simplified and speed up. The reconstruction procedure remains similar for both real and simulated

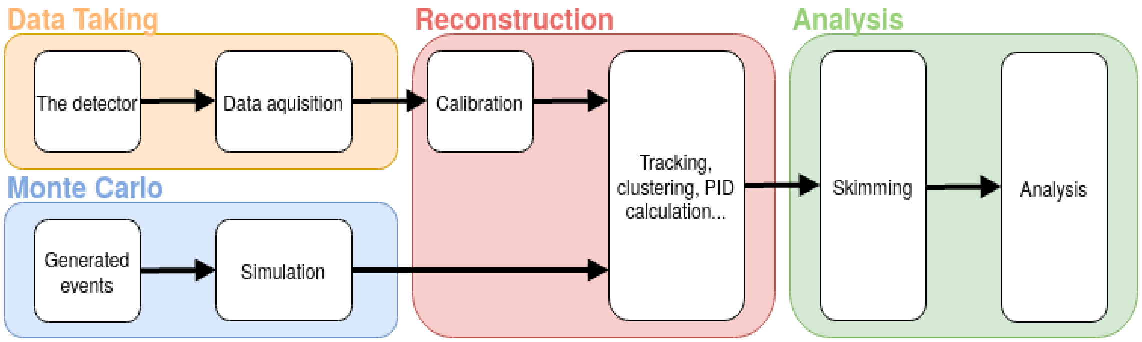

Figure 3.1: Overview of the experimental framework from data collection to data analysis [1].

data so that differences between the two can be minimized but calibration for the initial processing of real data is required.

3.1 Dataset

One of the crucial and fundamental steps is the collection of the data that has to be analyzed. To produce B mesons, electrons and positrons collide at the center-of-mass energy of $\sqrt{s} = 10.58$ GeV corresponding to the $\Upsilon(4S)$ resonance mass. At $\sqrt{s}$ $= 10.58$ GeV, the $e^+e^- \to \Upsilon(4S) \to B\bar{B}$ process is not the exclusive occurrence. The production of light and charm quark pairs in $e^+e^- \to u\bar{u}, d\bar{d}, s\bar{s}, c\bar{c}$ has a total cross-section of approximately 3.7 nb [2], more than three times larger than B meson production. However, the SuperKEKB accelerator [3] can also run beyond this energy and the Belle II experiment [4] can have multiple datasets. A specialized dataset is collected below the $\Upsilon(4S)$ where no B mesons are produced, providing a pure sample of off-resonance (or continuum) events. These special datasets are listed as follows:

- **Cosmic**

  During each run period, the Belle II experiment collects the cosmic muons at the beginning and end of each period. These muon events are mainly used for performance evaluations, calibration purposes and it provides a unique dataset to align the detectors with each other. To ensure muons cross the sub-detectors in a straight path, a part of the cosmic dataset is collected by deactivating the solenoid. During the downtime of the SuperKEKB accelerator that lasts for several days, the cosmic dataset is also collected to maintain the operation of the Belle II system.

- **Beam**

  Beam runs are the special small data takings that are collected to explore the beam-induced backgrounds for the inner sub-detectors. These runs are collected when the beams are circulating without colliding to eliminate processes associated with hard scattering in e^+e^- collisions.

- **Scan**

  A scan is composed of relatively short periods of data collection that lasts for hours or a few days and is performed at slightly different energies (usually 10–50 MeV apart). The scan dataset is used to measure the line shape of the e^+e^- cross-section either to confirm data collection on the resonance peak (short scans) or to perform actual physics measurements such as the search for exotic vector resonances (long scans above the $\Upsilon(4S)$ energy).

- **Non-$\Upsilon(4S)$**

  SuperKEKB can operate across the entire spectrum of bottomonia that ranges from the $\Upsilon(1S)$ at energy 9.460 GeV to slightly above the $\Upsilon(6S)$ at energy around 11.00 GeV. It can be utilized for all non-B aspects of the Belle II physics program. Also, these datasets are significant for spectroscopy, hadronic physics and dark sector studies.

Figure 3.2 represents the cross-section around the $\Upsilon(4S)$ resonances showing the difference between on- and off-resonance.

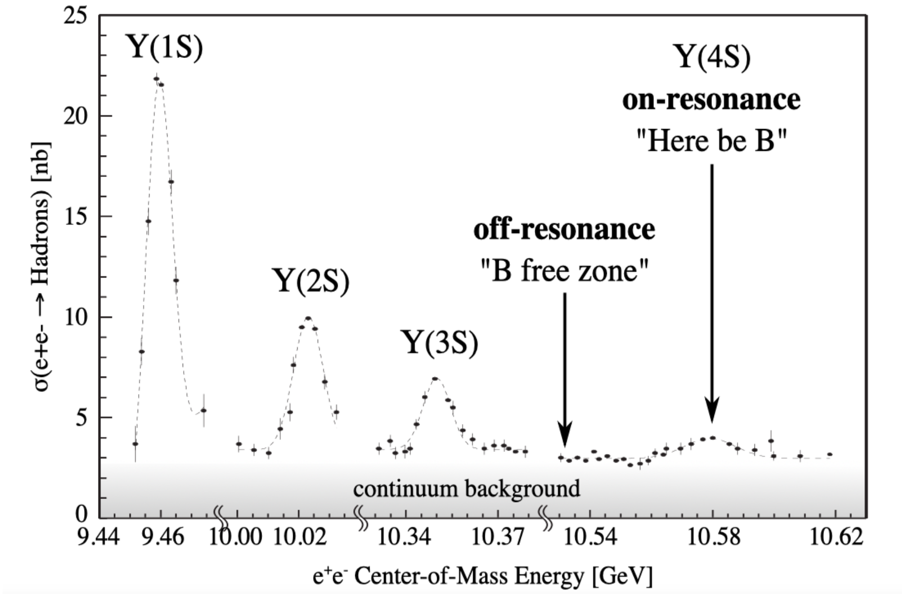

Figure 3.2: Cross-section around the $\Upsilon(4S)$ resonances showing the difference between on- and off-resonance [1].

3.1.1 Belle II dataset

The data undergoes two stages of processing: prompt processing and reprocessing. The difference between both processing is due to the calibration which is applied at the stage of processing. Prompt processing is like organizing and calibrating the data right after it collected and each chunk is called "bucket". Prompt data is obtained using the latest major software release. The calibration of prompt processing is completed with quality that is hardly different from the reprocessed data [5]. For analysis, prompt dataset is available within two months after processing.

Reprocessing is done by taking all the data collected up to a certain point and giving it a makeover. A reprocessing campaign, labeled with the prefix "proc" is done every year or every two years. Whether it's the prompt or reprocessed data, both can be accessed on the grid [6] using specific collections listed on the Data Production web page. Figure 3.3 shows the relationship between the data collected, prompt dataset and reprocessed dataset.

For the analysis described in this thesis, e^-e^+ collision data corresponding to

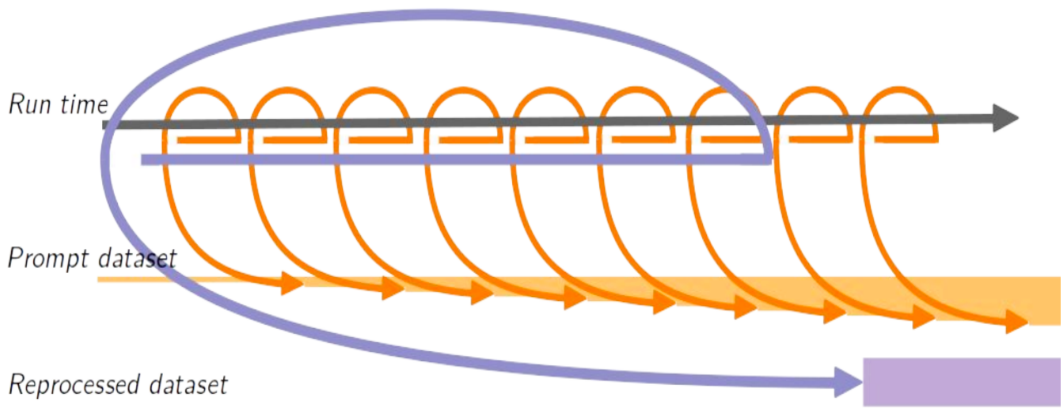

Figure 3.3: Relationship between the data collected, prompt dataset and reprocessed dataset [1].

426 fb^{-1} of luminosity have been used. This dataset includes proc13 data from experiments 7 to 18 and a prompt dataset from experiments 20 to 26, corresponding to $\Upsilon(4S)$, below the $\Upsilon(4S)$ and above the $\Upsilon(4S)$ energy at an integrated luminosity of 363 fb^{-1}, 42 fb^{-1} and 19 fb^{-1} luminosity, respectively [7]. The data was collected from 2019-2022 before the experiment entered its first long shutdown.

3.1.2 Simulated Data

Monte Carlo (MC) data plays a crucial role in High Energy Physics, providing a simulated representation of the events that occur within the Belle II detector post-collisions. This simulation provides an understanding of experimental conditions and performance. In both reconstruction and physics analyses, MC data undergo processing similar to real data with the advantage of knowing the "truth" behind each observation such as identifying whether a track originated from a muon or a pion in the CDC. Using MC simulated data has the advantage of containing both information with and without detector effects [8]. These simulations, known as generic MC events include all possible outcomes of an e^+e^- collision based on the current physical theories. The production of generic MC samples occurs in two successive steps: event generation and simulation.

3.1.2.1 Event generation

Event generation is the physics part where events are generated according to physics predictions by giving the initial conditions of electrons and positrons. These physics predictions could be both; advanced physics models such as SUSY or dark matter or it could be basics Standard Model processes. There are two types of events first one is "Signal MC" which represents the simulated data for a specific decay mode of the analysis. These signal events are particularly valuable for determining the reconstruction efficiency of a given process. Second, there are "Generic MC" samples that are based on the basic Standard Model processes. Generic samples are collected by repeating these procedures of event generations for individual processes and combining them based on their world-average branching fractions. Both the generic and signal MC are crucial in increasing our understanding of detector performance and refining selection criteria in the analysis of experimental data. Different event generators are used for different cases [9]. The main event generators used by the Belle II experiment are listed as follows:

- EvtGen [10]: EvtGen is the MC generator designed to simulate B and D decays initially developed for BaBar [11] and CLEO [12] and used within Belle. The Belle II collaboration currently collaborates closely with the EvtGen development team which is primarily based in LHCb to collectively develop the EvtGen package. EvtGen generator is controlled by a decay table that lists all possible decay processes, their branching ratios and the model used to decay them.

- KKMC [13]: It is the FORTRAN-based generator used to generate two fermion final state; $\mu^+\mu^-$, $\tau^+\tau^-$, $\nu^+\nu^-$ and $q\bar{q}$ for beam energies at and above the $\Upsilon(4S)$ resonance.

- MadGraph [14]: MadGraph is a framework designed to provide all the elements necessary for both Standard Model and Beyond Standard Model phenomenology.

- PHOKHARA [15]: PHOKHARA is the FORTRAN based generator used to generate eleven different leptonic and hadronic final states. These simulations cover scenarios both with and without photon emission, referred as radiative return (with photon emission) and scan mode (without photon emission), respectively.

- CRY [16]: The CRY software generates the distributions of cosmic-ray particle showers at three different elevations: sea level, 2100 meters, and 11300 meters. It generates output based on pre-tabulated data for muons, neutrons, protons, electrons, photons, and pions originating from primary protons with energies ranging from 1 GeV to 100 TeV.

- BABAYAGA.NLO [17]: BABAYAGA.NLO is a default generator used to simulate large-angle e^+e^- collisions that result in the $e^+e^- \to e^+e^-(\gamma)$ and $e^+e^- \to \gamma\gamma(\gamma)$ final states. It generates multiphoton initial-state radiation (ISR), final-state radiation (FSR), and the interference of initial and final-state radiation (IFI) based on the exact next-to-leading order (NLO) corrections matched with a parton shower algorithm. The generator claims a theoretical precision of about 0.1% for both cross-section and inclusive differential distributions within the detector acceptance.

- AAFH [18]: For non-radiative four-fermion final states like $e^+e^- \to e^+e^-e^+e^-$ and $e^+e^- \to e^+e^-\mu^+\mu^-$ AAFH is used which includes leading-order (LO) QED diagrams and their interference but no higher-order QED corrections or weak corrections. The LO calculation is exact and includes final-state mass kinematics with the LO divergence controlled by a minimum invariant secondary fermion pair mass, typically with $W_{ll} > 0.5$ GeV/c^2.

3.1.2.2 Simulation

Once the four-vectors of the event are generated, the next step is to simulate the events to make it look like output from the real detector. The detector measures the interaction of these particles with its material including processes like ionization, scintillation, bremsstrahlung, pair production and Cherenkov radiation. These well known processes can be simulated using Geant4 simulating software [19]. Geant4 uses the four-vectors to simulate how particles interact with the virtual Belle II detector. This simulation provides information on the energy deposited and the particles detected by each sub-detector. Additionally, custom software is used to translate the results from Geant4 into signals that mimic what is observed from the actual detector. For the Belle II experiment, the simulation of the entire detector takes approximately one second.

After simulation, the data obtained looks like the real data observed from the actual detector and allows to compare predictions with real measurements. However, Geant4 relies on an ideal description of the detector, but in reality, the detector comprises thousands of tons of hardware to measure positions with micrometer precision. Since every detail of the detector's material composition and placement cannot be perfectly known so there are unavoidable differences in the simulation. Minimizing these differences is important at the early stage of the experiments and efforts are made to improve the accuracy of the simulation by studying specific samples and conducting analyses.

3.2 Belle II Framework

$Basf2$ [20] is used as the software framework for the Belle II experiment. From generating simulated data to reconstruction and high-level analysis, $basf2$ is used in all aspects of the data processing chain at Belle II. $Basf2$ is a command line interface and this package contains Python functions and C++ modules that help

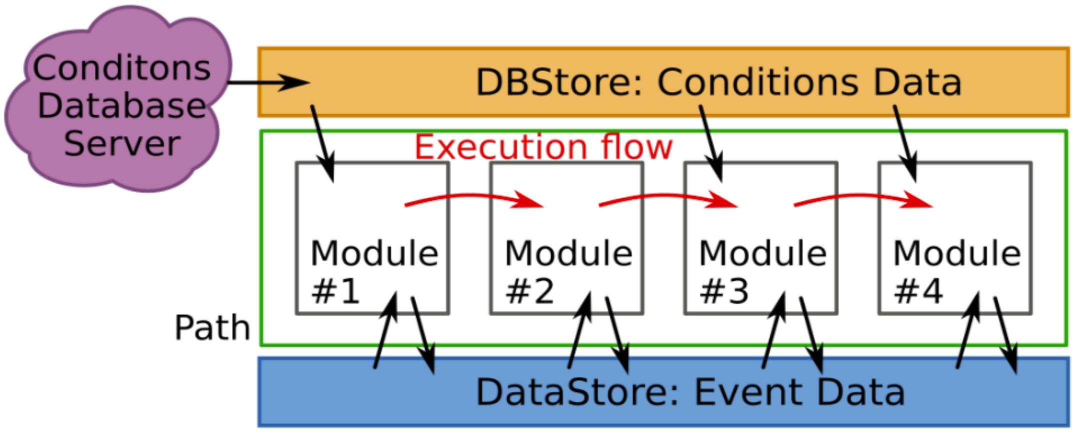

Figure 3.4: Schematic view of the processing flow in the Belle II Software (basf2) [1].

to perform the specific analysis. In the $basf2$ system, modules play a very important role in carrying out various tasks necessary for analyzing the data. The modules are like small units of work each designed to perform a specific function such as reading data from a file, simulating the detector's behavior or tracking particles. These modules act as building blocks of the data processing where each module contributes its part to the overall analysis. Modules are organized within a path which serves as a container for arranging them in a specific order. When it comes to processing the data, the framework follows the path and executes each module in the order it appears. Furthermore, modules are equipped with conditions that dictate the processing flow based on certain criteria. As data is processed, it is stored and accessed in a common storage area known as the Data Store. This allows modules to read from and write to the data as needed during the processing pipeline. Additionally, there are non-event data elements called conditions which provide additional information about the experimental conditions or the settings. These conditions are loaded from a central database known as the DBStore and are available for modules to access when necessary [21]. Figure 3.4 represents a schematic view of the processing flow in the Belle II Software.

Overall, the use of modules within paths forms the backbone of the Belle II data processing system, enabling efficient and organized analysis of experimental data while providing flexibility for different analysis tasks.

3.3 Object Reconstruction in Belle II

After collecting data and simulating events, there is a huge amount of information in the form of raw detector responses but it's not ready for analysis yet. This information needs to be processed to make it easier to understand. This is done to figure out which particles were involved in the interaction and get their original properties. However, it's hard to identify all the particles because some particles decay quickly before reaching the detector. Also, there are some unwanted signals in the detector, like random noise or background signals from other particles nearby. So, algorithms are used to find the set of most likely particles to be involved in the interaction and then later use statistical methods to study the events more closely. The reconstruction is the process where raw detector signals are processed to identify particle trajectories, ECL clusters and PID likelihoods.

The same reconstruction is performed for both simulated data and the real data by using the same algorithms for both. However, the advantage of simulated data is that it is known which particles are involved in the interaction. In addition to processing the data, track of the accuracy of reconstruction is kept which is known as "MC Truth". Following are the subsequent steps of the reconstruction:

3.3.1 Clustering

Clustering is the first step in the reconstruction of the raw data. It is a process to group detector responses from each sub-detector if they seem related. For example, if a particle passes through the pixel detector, it might trigger more than one pixel because it didn't go exactly through the center of one. These neighboring pixels are grouped into clusters by taking into account the detector's intrinsic properties such as noise. The size, shape and center of the clusters can be figured out. Analog readout of the pixel detector can measure the amount of ionization per pixel so the weighted average method can be used to figure out the central position. A

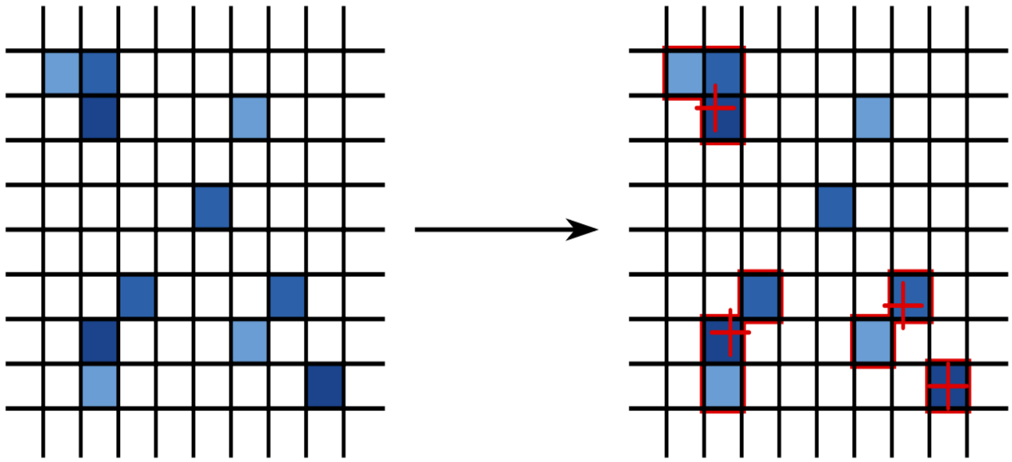

Figure 3.5: Simplified example of 2D clustering with analog signals [1].

similar principle is used in other sub-detectors too like in the strip detector and the calorimeter where nearby crystals are grouped in clusters. Figure 3.5 represents the example of 2D clustering with analog signals.

In calorimeters, the shape of clusters is different, the shape depends on the particle that causes clustering whether it is a photon or hadron. This makes it a bit difficult to define clusters in the calorimeter but the basic idea is the same to find all the signals caused by a particle and group them into clusters.

3.3.2 Tracking

Tracking is one of the major parts of the reconstruction of raw data. It is the process of identifying the trajectory of the particles known as tracks with the help of tracking detectors. Track finding and track fitting are two main parts of the tracking.

3.3.2.1 Track finding

Track finding is the process where detector hits that belong to a single track are grouped into a track candidate. The track finding process uses algorithms to figure out the tracks of the particles in the detector. There is a difference in the features

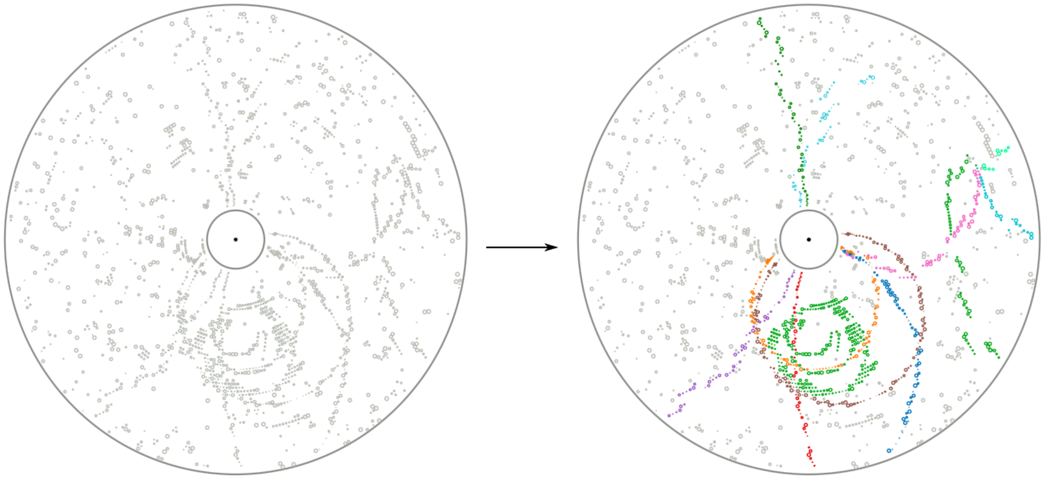

Figure 3.6: Illustration of the simulated event in an x-y cross-section of the CDC. The CDC hits displayed here originate from either charged particles associated with the event or beam-induced background noise. Hits that remain grey are rejected as background noise [1].

of detector hits in CDC [22] and VXD [23] so different algorithms are used for each. For VXD, a cellular automation model [24], [25] is used that connects the pairs of hits in adjacent layers to form track segments. These segments are then combined into track candidates using a lookup table called sector maps and geometrical requirements. The CDC uses two algorithms, the first is a global one that considers all hits simultaneously using a Hough transformation [26] and the second is a local one which searches for tracks based on neighboring hits. After finding tracks in both the detectors, they are merged based on the distance between the VXD and CDC track candidates extrapolated to the CDC's outer wall. Figure 3.6 represents the simulated event in an x-y cross-section of the CDC.

3.3.2.2 Track fitting

In Belle II, track fitting involves the determination of the best estimate of the kinematic variables that describe the particle trajectories associated with each found hit/cluster pattern to figure out particle position and momentum close to the interaction region as precisely as possible. The trajectory is described by five parameters that include the distance from the origin in the transverse plane (d_0), the longitudinal distance from the origin (z_0), the angle with respect to the x-axis (ϕ_0), the tangent of the angle between the momentum and the transverse plane ($\tan\lambda$), and the curvature (ω). However, the actual trajectories of particles are not perfect helices due to interactions with detector material and variations in the magnetic field. To account for these factors, Belle II uses algorithms like the deterministic annealing filter (DAF) [27], which is based on the Kalman filter (KF) [28]. The DAF considers interactions with material and adjusts the weights of points based on their deviation from the expected track, suppressing hits with large deviations.

3.3.3 Particle Identification

After identifying the tracks, the next task is to figure out the likelihoods of the tracks belonging to different types of particles. The contributions from various sub-detectors are examined to verify if they detect any relevant signal corresponding to each track. For example, in CDC total energy loss along the track is calculated and compared with expected values for different particle types. In ARICH [29], the area where track enters is examined to look for Cherenkov rings around this. The same approach is used for TOP [30], ECL [31] and KLM [32] where the likelihood of signals from different particle types is determined based on the track's entry point. Subsequently, these detectors calculate likelihoods for the signal from different types of the particles and then information is combined with the track information for use further analysis.

3.3.4 Data Formats

When electrons and positrons collide in the Belle II detector, they produce signals in the sub-detectors. These signals are collected, matched and stored in a binary format on disk. To reconstruct this data, there are several steps: unpacking, calibration, reconstruction and analysis. Each step involves reading and writing different types of objects and producing files in various formats.

These data objects are categorized in four groups: raw, low-level, reconstruction-level, and analysis-level. Raw objects are the initial outputs from the subsystems while low-level objects are abstracted versions after unpacking. Reconstruction-level objects result from running algorithms on these signals to generate useful quantities like tracks and PID likelihood. Finally, analysis-level objects are used for physics analysis, representing charged particles, photons and other relevant quantities.

There are four data formats in Belle II:

- Raw: Raw is the basic data format that contains un-processed and un-calibrated detector output. Since it cannot be used for analysis, this data serves as a base to produce other data formats.
- cDST (calibration Data Summary Table): cDST data contains same objects as of the raw data along with results from the tracking so reconstruction can be performed using this data format. To execute low-level detector studies and to measure calibration constants, cDST data format is used.
- mDST (mini Data Summary Table): mDST is the basic format for the data analysis that contains high-level information that is used to carry out the physics analysis.
- uDST (user Data Summary Table): uDST is the main format for the data analysis which contains output from the skim analysis. The skimming procedure selects only a few events from mDST which are useful for certain analyses. The content of the cDST format is the same as mDST along with reconstructed particles used in the skimming procedure.

Figure 3.7 represents the data modeling scheme in Belle II with data formats.

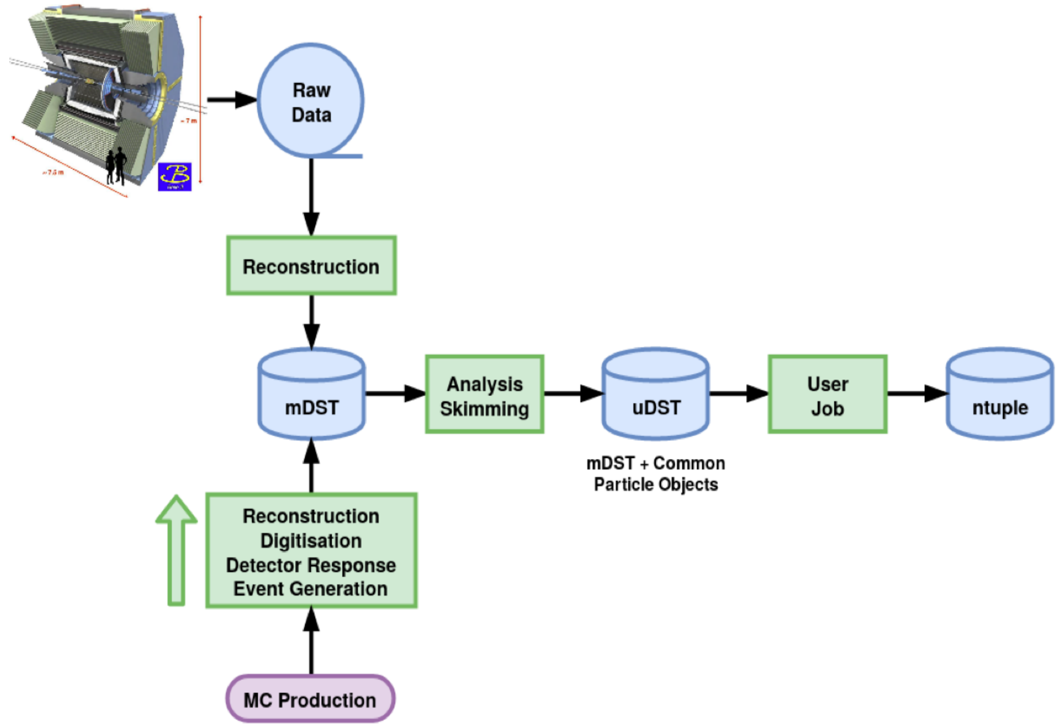

Figure 3.7: Simplified data model in Belle II experiment [33].

3.4 Analysis overview

In e^+e^- collisions, many states emerge that include bound states of quarks and antiquarks as well as free leptons. These states include heavy resonances, mesons and baryons. The Belle II detector provides the momentum, energy and Particle Identification (PID) information of particles produced in e^+e^- collisions. However, not all particle yields all three types of information. The bound states are short-lived and do not leave signals directly in the detector. These states typically decay into stable particles that leave their traces as hits in various sub-detectors of the detector. The charged particles including $e^\pm$, $\mu^\pm$, $\pi^\pm$, $K^\pm$ and $p(\bar{p})$ and neutrals, γ and K_L are the only particles detected by the detectors while everything else is short-lived to be detected. Unstable particles can be reconstructed from the stable decay particles known as daughters and combining these stable particles to reproduce an e^+e^- event is known as an event reconstruction. The distinction between "measured particles" that are reconstructed directly from detector signals and the "combined particles" that are reconstructed as a sum of measured particles is a crucial distinction. Reconstructed particles are also known as final state particles because they are the final products of the decay chain that are require for any analysis.

- **Reconstructed Particles**
  Reconstructed particles originate from the reconstruction of the charged particles from tracks and photons or neutral kaons (K_L) from clusters in the ECL or KLM. For charged particles, tracks are reconstructed from the paths left by particles as they pass through the detector. However, tracks only provide information about the particle's momentum in three dimensions so to calculate the full four-momentum assumptions are made about its mass. These mass assumptions often rely on the output of the PID detectors. On the other hand, clusters only provide information about the energy but not about the momentum. To obtain the momentum, assumptions are made not only about the particle's mass but also about its production point. It is assumed that photons and K_L originate at the primary interaction point. Reconstructed particles serve as the basic building block of the analysis. Tracks and clusters are created during the reconstruction step with the mass assignment being the only operation left for the final user at the analysis level.

- **Combined Particles**
  Combined particles are reconstructed by summing the four-momentum vectors of the reconstructed particles. This allows the reconstruction of any resonance but all their decay products must be measured properly. These combined particles can further be combined to move upward towards the decay tree until the final desired step is reached. Unlike reconstructed particles, creating combined particles is left to the final user at the analysis level. Belle II provides tools within the $basf2$ package to reconstruct this process.

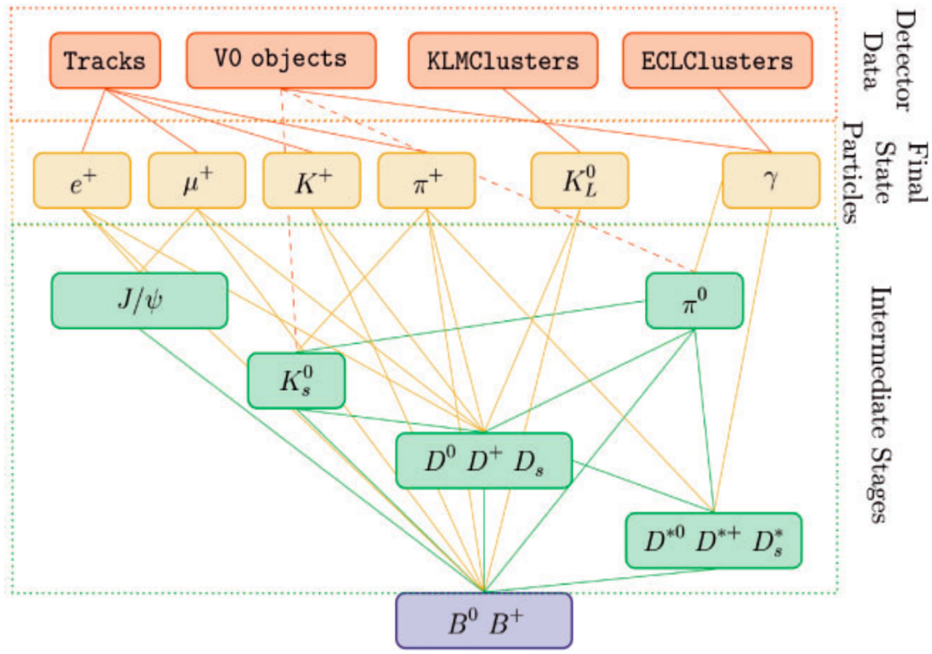

Figure 3.8: Illustration of the detector's data, final state particles and intermediate particles to reconstruct B mesons in Full event interpretation algorithm [1].

- **V0 Particles**

  Lastly, there exists a unique category of combined particles known as V0 particles. These are neutral particles that decay into two charged particles far from the interaction point, leaving a distinct V-shaped signature and are provided by the reconstruction procedure. While they can be reconstructed by combining the four-momenta of their daughters but if the decay happens outside the beam pipe, it's better to re-run tracking before doing so. This is because tracks originating outside the interaction point cross less material than expected, requiring updates to the multiple scattering corrections.

In conclusion, Belle II's approach of handling particles involves reconstructing both measured and combined particles, with special attention to V0 particles due to their unique characteristics. These processes are essential for extracting meaningful physics results from the detector data. Figure 3.8 represents the final state particles and the intermediate particles to reconstruct final B mesons.

3.4.1 Background Contribution

Numerous processes or interactions can affect signal identification either by producing the same final state as the signal or by producing particles that overlap with signal events, thereby altering the composition of the final state. These are commonly referred to as backgrounds. Belle II analyses categorize backgrounds into the following types:

1. **Trigger Backgrounds:** Processes such as $e^+e^- \to e^+e^-$ that can be rejected at the trigger stage or by implementing simple cuts are identified as trigger backgrounds [34].

2. **Physics Backgrounds:** These types of backgrounds arise from physics processes that mimic the signal, for examples in the $D^0 \to \gamma\gamma$ analysis, $D^0 \to \pi^0\pi^0$ act as a major physics background. These types of backgrounds can be rejected with the help of various selection cuts within the analysis.

3. **Radiative Bhabha process:** Photons produced in the radiative Bhabha scattering interact with the iron of the magnets and generate neutrons that act as a significant background source for the KLM detector. In KEKB, shared QCS magnets over-bent the scattered particles and caused them to hit the magnet walls and create the electromagnetic showers. However, in SuperKEKB separate quadrupole magnets are used which reduces this background [38].

4. **Two-photon process:** The fifth beam background comes from low-momentum electron-positron pairs created by a two-photon process $ee \to eeee$. These pairs can spiral along the solenoid's field lines and cause multiple hits in Belle II's inner detectors. Additionally, primary particles that lose significant energy or scatter at large angles can also be lost in the detector.

5. **Continuum Background:** This type of background arises from non-resonant $e^+e^- \to q\bar{q}$ hadronic events and these events not only include $B\bar{B}$ production but also the hadronization of light quarks (uds) and charm quarks that mimics signals for many physics measurements. These events generate multiple tracks per event so there are chances to find the signal like tracks and clusters. While some background can be reduced but many analyses retain some of it because tighter cuts on continuum suppression variables can significantly reduce the efficiency of the signal. $e^+e^- \to c\bar{c}$ events contain both the signal and background for the present analysis. The signal and background contributions in $e^+e^- \to c\bar{c}$ are separated using truth matching information.

6. **Beam-Induced Background:** Beam-Induced Background consists of tracks and clusters that did not originate from primary e^+e^- collisions but from other interactions within the beam itself. Beam-induced backgrounds, primary, provide additional particles which changes the final state of the signal event and make it difficult to identify. Compared to previous experiment Belle, these backgrounds are more common in Belle II due to the more tightly focused beams at SuperKEKB. The presence of such tracks and clusters is usually acceptable and can be rejected at the final stage of the analysis [35]. At SuperKEKB, following are the five main types of beam backgrounds:

   - **Touschek scattering:** At SuperKEKB Touschek scattering [36] takes place when particles in the same bunch of the beam go through Coulomb scattering which causes some particles to gain more energy while some of the particles lose energy. Special devices called collimators and shields are used to stop these scatter particles from reaching Belle II.
   - **Beam-gas scattering:** This happens when particles in the beam hit gas molecules left over in the beam pipe. It occurs in two ways: first is Coulomb scattering, where the beam particles change the direction

and second is bremsstrahlung scattering [37], where they lose the energy. At SuperKEKB, this is expected to be 100 times more than at KEKB because of the smaller beam pipe and larger vertical beta function. This background can also be reduced by using collimators and shields [35].

- **Synchrotron radiation:** Another background source is synchrotron radiation (SR) emitted by the beam. HER is the main source of this background. SR emits X-ray-like photons that can damage the detectors. To prevent this, the inner surface of the beam pipe is coated with gold and the pipe's shape is designed in such a way to avoid direct hits on the detectors.

3.5 Chapter in a Nutshell

This chapter provides an overview of the dataset used in the Belle II experiment and provides the details of the process from data collection to the analysis. It starts with an explanation of the data collection framework in the Belle II experiment with the focus on the differences between prompt and reprocessed data, luminosity and the various types of on-resonance and off-resonance data. The chapter also highlights the importance of simulated data and discusses the event generators used for producing Monte Carlo samples. The section on object reconstruction in Belle II covers tracking, clustering and particle identification in raw data and describes the different formats used for storing processed data for analysis. The analysis review section outlines the reconstruction chain by explaining reconstructed, intermediate and V0 particles. Lastly, the chapter concludes with the different background sources at SuperKEKB and the strategies to mitigate them.

Bibliography

[1] Belle II Collaboration, "Belle II Software Documentation," https://software.belle2.org/development/sphinx/index.html.

[2] E. Kou et al., "The Belle II physics book," *Progress of Theoretical and Experimental Physics*, vol. 2019, Dec. 2019.

[3] Y. Ohnishi et al., "Accelerator design at SuperKEKB," *Progress of Theoretical and Experimental Physics*, vol. 2013, p. 03A011, Mar. 2013.

[4] A. Abashian et al. (Belle Collaboration), "The Belle Detector," *Nuclear Instruments and Methods in Physics Research Section A: Accelerators, Spectrometers, Detectors and Associated Equipment*, vol. 479, pp. 117–232, 2002.

[5] D. Dossett and M. Sevior, "Prompt calibration automation at Belle II," *EPJ Web of Conferences*, vol. 245, p. 02016, 2020.

[6] V. Bansal, "Grid computing at belle ii," *arXiv: Computational Physics*, 2015.

[7] T. B. I. Collaboration, "Measurement of the integrated luminosity of data samples collected during 2019-2022 by the Belle II experiment," 2024. https://arxiv.org/abs/2407.00965.

[8] Sato, Yo, Cunliffe, Sam, Meier, Frank, and Zupanc, Anze, "Monte Carlo matching in the Belle II software," *EPJ Web Conf.*, vol. 251, p. 03021, 2021.

[9] T. Ferber and P. Urquijo, "Overview of the Belle II Physics Generators," Jun 2015. https://docs.belle2.org/record/282?ln=en.

[10] D. Lange, "The EvtGen particle decay simulation package," *Nuclear Instruments and Methods in Physics Research Section A: Accelerators, Spectrometers, Detectors and Associated Equipment*, vol. 462, pp. 152 – 155, 2001.

[11] B. Aubert et al. (BaBar Collaboration), “The BaBar detector,” *Nuclear Instruments and Methods in Physics Research A: Accelerators, Spectrometers, Detectors and Associated Equipment*, vol. 479, pp. 1–116, 2002.

[12] Y. Kubota et al. (CLEO Collaboration), “The CLEO II detector,” *Nuclear Instruments and Methods in Physics Research Section A: Accelerators, Spectrometers, Detectors and Associated Equipment*, vol. 320, no. 1, pp. 66–113, 1992.

[13] S. Jadach et al., “Multi-photon Monte Carlo event generator KKMCee for lepton and quark pair production in lepton colliders,” *Computer Physics Communications*, vol. 283, p. 108556, Feb. 2023.

[14] M. Herquet and F. Maltoni, “MadGraph/MadEvent: A multipurpose event generator,” *Nuclear Physics B - Proceedings Supplements*, vol. 179-180, pp. 211–217, Aug. 2008.

[15] H. Czyz, M. Gunia, and J. Kuhn, “Simulation of electron-positron annihilation into hadrons with the event generator PHOKHARA,” *Journal of High Energy Physics*, vol. 2013, no. 8, 2013.

[16] C. Hagmann, D. Lange, and D. Wright, “Cosmic-ray shower generator (CRY) for Monte Carlo transport codes,” *2007 IEEE Nuclear Science Symposium Conference Record*, vol. 2, pp. 1143–1146, 2007.

[17] C. Calame, G. Montagna, O. Nicrosini, and F. Piccinini, “Status of the BabaYaga event generator,” *EPJ Web of Conferences*, vol. 218, p. 07004, Jan. 2019.

[18] F. A. Berends, P. H. Daverveldt, and R. Kleiss, “Monte Carlo Simulation of Two Photon Processes. 2. Complete Lowest Order Calculations for Four Lepton Production Processes in electron Positron Collisions,” *Computer Physics Communications*, vol. 40, pp. 285–307, 1986.

[19] S. Agostinelli *et al.*, “GEANT4: A Simulation toolkit,” *Nuclear Instruments and Methods in Physics Research Section A: Accelerators, Spectrometers, Detectors and Associated Equipment*, vol. 506, pp. 250 – 303, Jan. 2003.

[20] N. Braun et al., “The Belle II Core Software,” *Computing and Software for Big Science*, vol. 3, Nov. 2018.

[21] L. Wood et al., “Performance of the Belle II Conditions Database,” *EPJ Web of Conferences*, vol. 214, p. 04050, Jan. 2019.

[22] N. Taniguchi, “Central drift chamber for belle-ii,” *Journal of Instrumentation*, vol. 12, no. 06, p. C06014, 2017.

[23] T. Abe et al. (Belle II Collaboration), *“Belle II Technical Design Report”*. KEK-REPORT-2010-1, 2010.

[24] T. Bilka et al., “Demonstrator of the Belle II online tracking and pixel data reduction on the High Level Trigger system,” *IEEE Transactions on Nuclear Science*, vol. 62, pp. 1155–1161, 2015.

[25] T. Bilka et al., “The track finding algorithm of the Belle II vertex detectors,” *EPJ Web of Conferences*, vol. 150, p. 00007, Jan. 2017.

[26] P. V. Hough, “METHOD AND MEANS FOR RECOGNIZING COMPLEX PATTERNS,” *U.S. Patent 3069654*, Dec. 1962.

[27] R. Frühwirth and A. Strandlie, “Track fitting with ambiguities and noise: A study of elastic tracking and nonlinear filters,” *Computer Physics Communications*, vol. 120, pp. 197–214, 1999.

[28] R. Fruhwirth, “Application of Kalman filtering to track and vertex fitting,” *Nuclear Instruments and Methods in Physics Research Section A: Accelerators, Spectrometers, Detectors and Associated Equipment*, vol. 262, pp. 444–450, 1987.

[29] K. Uno, "Operation and performance of the Belle II Aerogel RICH detector," *Nuclear Instruments and Methods in Physics Research Section A: Accelerators, Spectrometers, Detectors and Associated Equipment*, vol. 1056, p. 168635, 2023.

[30] M. Akatsu et al., "Time-of-propagation Cherenkov counter for particle identification," *Nuclear Instruments and Methods in Physics Research Section A: Accelerators, Spectrometers, Detectors and Associated Equipment*, vol. 440, pp. 124–135, 2000.

[31] V. Aulchenko et al., "Electromagnetic calorimeter for Belle II," *Journal of Physics: Conference Series*, vol. 587, p. 012045, Feb. 2015.

[32] T. Aushev et al., "A scintillator based endcap K_L and muon detector for the Belle II experiment," *Nuclear Instruments and Methods in Physics Research Section A: Accelerators, Spectrometers, Detectors and Associated Equipment*, vol. 789, pp. 134–142, 2015.

[33] D. Dossett, "Computing and Software at Belle II," *EPJ Web of Conferences*, vol. 245, p. 11007, 2020.

[34] S. Skambraks, S. Neuhaus, and C. Kiesling, "Background Suppression with the Belle II Neural Network Trigger," *Journal of Physics: Conference Series*, vol. 1085, p. 042026, Sept. 2018.

[35] A. Natochii et al., "Measured and projected beam backgrounds in the Belle II experiment at the SuperKEKB collider," *Nuclear Instruments and Methods in Physics Research Section A: Accelerators, Spectrometers, Detectors and Associated Equipment*, vol. 1055, p. 168550, 2023.

[36] A. Piwinski, "The Touschek effect in strong focusing storage rings," Nov. 1998. `https://arxiv.org/abs/physics/9903034`.

[37] H. W. Koch and J. W. Motz, "Bremsstrahlung Cross-Section Formulas and Related Data," *Reviews of Modern Physics*, vol. 31, pp. 920–955, Oct. 1959.

[38] J. Schueler et al., “Application of recoil-imaging time projection chambers to directional neutron background measurements in the SuperKEKB accelerator tunnel,” *Nuclear Instruments and Methods in Physics Research Section A: Accelerators, Spectrometers, Detectors and Associated Equipment*, vol. 1040, p. 167291, 2022.

Chapter 4

Measurement of the $\mathcal{B}(D_s^{*+} \to D_s^+\pi^0)/\mathcal{B}(D_s^{*+} \to D_s^+\gamma)$

This research work is based on the measurement of the branching fraction, $\mathcal{B}(D_s^{*+} \to D_s^+\pi^0)$ with respect to $\mathcal{B}(D_s^{*+} \to D_s^+\gamma)$. The measurement requires reconstruction of $D_s^{*+} \to D_s^+\pi^0$ and $D_s^{*+} \to D_s^+\gamma$ decay modes. This chapter gives an overview of the analysis methodology to reconstruct $D_s^{*+} \to D_s^+\pi^0$ and $D_s^{*+} \to D_s^+\gamma$ decay modes and subsequently measure the ratio of branching fractions using Belle II data.

4.1 Introduction

The branching fraction of $D_s^{*+} \to D_s^+\pi^0$ with respect to $D_s^{*+} \to D_s^+\gamma$ has been previously measured by CLEO [1], BaBar [2] and BESIII [3] experiments. Figure 4.1 illustrates the $\mathcal{B}(D_s^{*+} \to D_s^+\pi^0)/\mathcal{B}(D_s^{*+} \to D_s^+\gamma)$ measured by different experiments. The present analysis uses a methodology similar to the CLEO [4] and BaBar [5] analysis, with the inclusion of an additional decay mode ($D_s^+ \to K^+ \bar{K}^{*0}$) to enhance the sensitivity of the measurement. The recent measurements from BESIII [6] adopted a different approach based on inclusive analysis. The present measurement benefits from the larger statistics as compared to previous studies. A reduction in systematic uncertainties associated with fitting procedure, a better γ/π^0 efficiency corrections and the dependence on $p^*(D_s^{*+})$ is also anticipated.

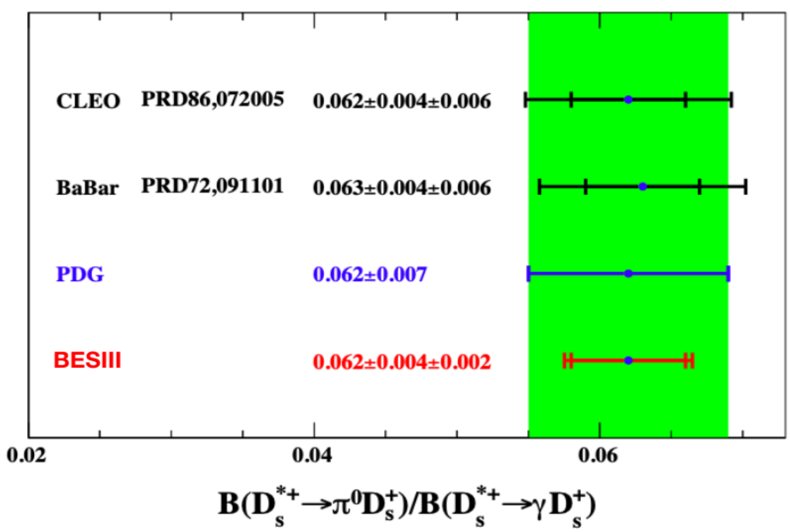

Figure 4.1: Comparison of $\mathcal{B}(D_s^{*+} \to D_s^+\pi^0)/\mathcal{B}(D_s^{*+} \to D_s^+\gamma)$ measured by different experiments [6].

The decay modes $D_s^{*+} \to D_s^+\pi^0$ and $D_s^{*+} \to D_s^+\gamma$ are reconstructed as:

- $D_s^{*+} \to D_s^+\pi^0$
  - $D_s^+ \to \phi\pi^+$

    $\phi \to K^+K^-$
  - $D_s^+ \to \bar{K}^{*0}K^+$

    $\bar{K}^{*0} \to \pi^+K^-$

- $D_s^{*+} \to D_s^+\gamma$
  - $D_s^+ \to \phi\pi^+$

    $\phi \to K^+K^-$
  - $D_s^+ \to \bar{K}^{*0}K^+$

    $\bar{K}^{*0} \to \pi^+K^-$

Charge conjugate decay modes are implied throughout the text. The effective branching ratios $\mathcal{B}(D_s^+ \to \phi\pi^+)\times\mathcal{B}(\phi \to K^+K^-)$ and $\mathcal{B}(D_s^+ \to K^+\bar{K}^{*0})\times\mathcal{B}(\bar{K}^{*0} \to K^-\pi^+)$ of the decay modes, under considerations, are 2.24 ± 0.06 % and 2.58 ± 0.06 %, respectively [7].

The ratio of branching fraction for decay modes $D_s^{*+} \to D_s^+\pi^0$ and $D_s^{*+} \to D_s^+\gamma$ is defined as:

$$\frac{\mathcal{B}(D_s^{*+} \to D_s^+\pi^0)}{\mathcal{B}(D_s^{*+} \to D_s^+\gamma)} = \frac{N(D_s^{*+} \to D_s^+\pi^0)}{N(D_s^{*+} \to D_s^+\gamma)} \times \frac{\epsilon(D_s^{*+} \to D_s^+\gamma)}{\epsilon(D_s^{*+} \to D_s^+\pi^0)}. \tag{4.1}$$

Here, $N(D_s^{*+} \to D_s^+\pi^0)$ and $N(D_s^{*+} \to D_s^+\gamma)$ represent the signal yields and $\epsilon(D_s^{*+} \to D_s^+\pi^0)$ and $\epsilon(D_s^{*+} \to D_s^+\gamma)$ represent the signal selection efficiencies for the decay modes $D_s^{*+} \to D_s^+\pi^0$ and $D_s^{*+} \to D_s^+\gamma$, respectively. The measurement of these signal yields and selection efficiencies require a detailed analysis of data and Monte Carlo samples as discussed in the subsequent sections.

4.2 Data and Monte Carlo samples

The present analysis is performed using electron-positron collision data collected with the Belle II detector. The analyzed data corresponds to an integrated luminosity of 424 fb^{-1} taken from experiments 7 to 26. This data includes collisions at $\Upsilon(4S)$ peak and also off the $\Upsilon(4S)$ peak with respective luminosity of 363 fb^{-1} and 61 fb^{-1} [8]. The data was collected during 2019-2022 before the experiment entered its first long shutdown. This dataset is sufficient to perform statistically robust measurements.

It is essential to use Monte Carlo samples to establish the robustness of the measurement. The MC samples are crucial to optimize the selection criteria, extract signal efficiency and evaluate the systematic uncertainties [9]. The signal events are generated using event generators [10] such as EvtGen [11], KKMC [12], etc. One million centrally produced signal MC events have been used for this measurement. The background process i.e. $c\bar{c}$, $u\bar{u}$, $d\bar{d}$, $s\bar{s}$, $B^0\bar{B}^0$ and $B\bar{B}$ production at $\Upsilon(4S)$ are produced with a run-independent generic MC samples corresponding to an integrated luminosity of 1 ab^{-1}. The $c\bar{c}$ production includes both signal as well as background events. The detector effects are simulated in the MC events using GEANT4 package [13].

4.3 Selection Criteria

As discussed earlier, the signal processes have charged and neutral particles in the final state. The clean identification of the signal processes requires efficient reconstruction and identification of these particles. This analysis process involves a combination of selection criteria to suppress the contribution of background processes to an acceptable level.

4.3.1 Charged particle selection

There are three charged tracks (K^+, K^-, π^+) in the final state of $D_s^{*+} \to D_s^+\pi^0$ and $D_s^{*+} \to D_s^+\gamma$ decay channels. To reduce the background contribution from off Interaction Point, a cut on the transverse (dr) and longitudinal (dz) impact parameters are applied. The parameters dr and $|dz|$ are required to be smaller than 1 cm and 3 cm, respectively.

After passing through the detector, it is possible that the pion track is misidentified as the kaon track or vice-versa. This misidentification of particles is suppressed by using particle identification variables that assess the likelihood of a particle being a pion compared to a kaon and a particle being a kaon compared to a pion [14]. Various particle ID variables are accessible for identifying six charged particle types (electron, muon, pion, kaon, proton, or deuteron). The specific variables used in this analysis are explicitly defined as follows:

$$PionID = \frac{\mathcal{L}_\pi}{\mathcal{L}_\pi + \mathcal{L}_K} \tag{4.2}$$

and

$$KaonID = \frac{\mathcal{L}_K}{\mathcal{L}_\pi + \mathcal{L}_K} \tag{4.3}$$

$PionID$ cut returns the probability of pions with respect to kaons and $KaonID$ returns the probability of kaons with respect to pions, by using particle identification information from all sub-detectors to identify tracks as pions and kaons, respectively. $\mathcal{L}_K(\mathcal{L}_\pi)$ is the likelihood of a charged track being attributed to a kaon (pion). A loose cut of $PionID > 0.4$ and $KaonID > 0.4$ is applied to suppress the contribution of misidentified particles.

4.3.2 γ reconstruction

In the final state of the signal, there are γ and π^0. The π^0 also decays to two γ with a 98% branching fraction [7]. At first it is important to efficiently reconstruct photons using ECL [15]. This identification requires the usage of multiple ECL based variables as discussed below:

- An ECL cluster is treated as a γ candidate if it is isolated from the extrapolated charged tracks. To eliminate γs from the beam background and detach hadronic shower fragments, the γs are required to have minimal energy value. For π^0, in $D_s^{*+} \rightarrow D_s^+\pi^0$ mode, the energy of γ candidates is required to $E_\gamma^{barrel} > 30$ MeV, $E_\gamma^{forward} > 120$ MeV and $E_\gamma^{backward} > 80$ MeV for barrel, forward endcap and backward endcap, respectively. For the $D_s^{*+} \rightarrow D_s^+\gamma$ mode, γs are expected with higher energy, therefore, a stringent condition is applied to the energy i.e. $E > 300$ MeV.

- A real photon is expected to deposit most of its energy in a single crystal. To suppress the fake photon contribution, the relative energy distribution of the surrounding crystals is taken into account using a variable called **clusterE1E9**. This variable is defined as the ratio of the highest energy crystal and the sum of energy deposit in 9 (3×3) crystals surrounding the highest energy crystal. The **clusterE1E9** should be greater than 0.4 for the $D_s^{*+} \rightarrow D_s^+\pi^0$ decay mode and a tighter cut, greater than 0.6, is applied for the $D_s^{*+} \rightarrow D_s^+\gamma$ mode to address the higher background levels.

- **ClusterTheta** is defined as the polar angle of the ECL cluster and the requirement on clusterTheta is; $0.5 <$ clusterTheta < 2.6180.

- **ClusterNHits** is defined as the sum of weights of all crystals in an ECL cluster and it is required to be larger than 1.5 for both $D_s^{*+} \rightarrow D_s^+\pi^0$ and $D_s^{*+} \rightarrow D_s^+\gamma$ decay modes.

4.3.2.1 π^0 reconstruction

To reconstruct π^0 candidates in the mode $D_s^{*+} \rightarrow D_s^+\pi^0$, the invariant mass of the two photons, $M(\gamma\gamma)$ is required to lie between 0.121 GeV/c^2 and 0.142 GeV/c^2.

This cut effectively eliminates incorrectly paired photons not originating from a parent π^0. The azimuthal angle difference, $\Delta\phi(\gamma\gamma)$, between the two photons coming from π^0 decay is constrained within the range of [-1.2, 1.2], which selects 73% of the signal while rejecting approximately 50% of the background. Additionally, the angle between the momenta of the pair of photon candidates, $\Delta\theta(\gamma_1\gamma_2)$, is required to be less than 1. This cut retains 52% of the signal while significantly reducing background contributions by about 72%. Furthermore, a constraint is applied to the nominal π^0 mass to enhance the overall resolution of the decay. More details about these cuts can be found at the reference [16].

4.3.3 D_s^+ and D_s^{*+} reconstruction

D_s^+ is reconstructed using $D_s^+ \to \phi(K^+K^-)\pi^+$ and $D_s^+ \to \bar{K}^{*0}(\pi^+K^-)K^+$ D_s^{*+} modes. Here, the ϕ candidate is reconstructed using K^+ and K^- candidates with an invariant mass lies between 1.01 - 1.03 GeV/c^2. The π^+ candidates combined with K^- candidates to reconstruct $\bar{K}^{*0}$ candidates with an invariant mass between 0.84 GeV/c^2 and 0.94 GeV/c^2. Figure 4.2 (a) and 4.2 (b) represents the invariant of mass ϕ and $\bar{K}^{*0}$ candidates, respectively. The signal and background are extracted from generic MC samples while signal is identified using truth matching information and background is obtained by removing the signal component. These selected ϕ and $\bar{K}^{*0}$ candidates recombined with π^+ and K^+ candidates, respectively to form D_s^+ candidates with an invariant mass lies between 1.93 GeV/c^2 and 2.01 GeV/c^2. For the decay chains, $D_s^+ \to \phi\pi^+$ and $D_s^+ \to \bar{K}^{*0}K^+$, a vertex fit [17, 18] is applied and only candidates with a confidence level > 0.001 are considered. Additionally, a cut is imposed on the cosine of the helicity angle, $|cos(\theta_{Hel})| > 0.4$, where the helicity angle (θ_{Hel}) is defined as the angle between the momentum of $K^+(\pi^+)$ and the direction opposite to the momentum of D_s^+ in the rest frame of $K^+K^-(\pi^+K^-)$

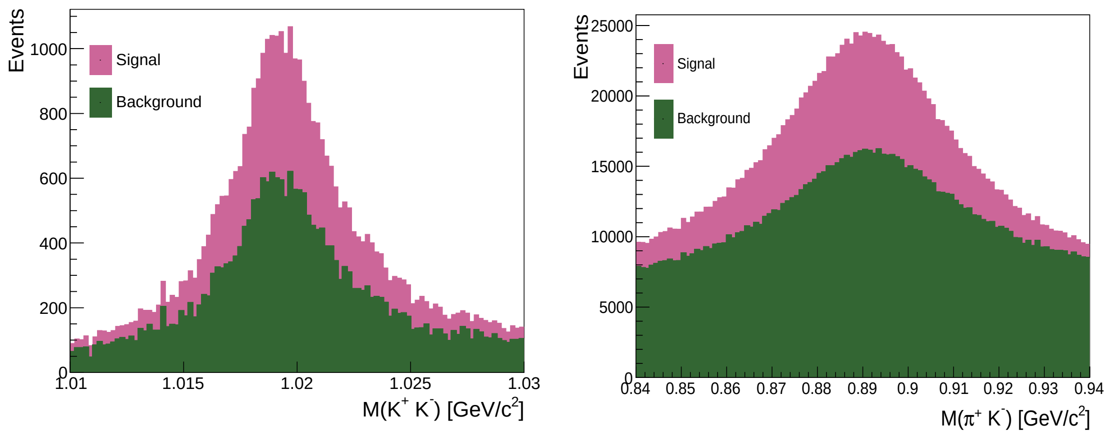

(a) (b)

Figure 4.2: (a) M(K^+K^-) and (b) M(π^+K^-) distributions, here magenta distribution is signal and the green distribution represents background.

for $D_s^+ \to \phi\pi^+(D_s^+ \to \bar{K}^{*0}K^+)$. This condition reduces about 25% background while retaining 95% of the signal event.

For D_s^{*+} candidates, difference between the invariant mass of D_s^{*+} and D_s^+, ΔM, is required to be in 0.14 - 0.16 GeV/c^2 and 0.1 - 0.18 GeV/c^2 for the $D_s^{*+} \to D_s^+(\phi\pi^+)\pi^0$ and $D_s^{*+} \to D_s^+(\phi\pi^+)\gamma$ modes, respectively. Additionally, to reject the contribution of charmed mesons coming from B decays, the center of mass momentum of D_s^{*+}, $p^*(D_s^{*+})$, is required to be larger than 2.5 GeV/c. Table 4.1 summarizes the selection criteria for $D_s^{*+} \to D_s^+\pi^0$ and $D_s^{*+} \to D_s^+\gamma$ modes.

4.3.4 π^0 veto for $D_s^{*+} \to D_s^+\gamma$

One of the possible backgrounds for the $D_s^{*+} \to D_s^+\gamma$ mode is where γ is coming from the decay of π^0. To reject this contribution π^0 veto is applied. For this purpose, $D_s^{*+} \to D_s^+\gamma$ decay is reconstructed using the selection criteria as discussed above. Subsequently, a Rest of Event (ROE) is reconstructed event that includes every particle that is not associated with the signal event or specific decay mode of interest. Then, γ of the signal events is combined with other γs, having energy > 50 MeV, in

Objects	Selection Cuts ($D_s^{*+} \to D_s^+ \pi^0$)	Selection Cuts ($D_s^{*+} \to D_s^+ \gamma$)
Tracks	$dr < 1$ cm $\lvert dz\rvert < 3$ cm	$dr < 1$ cm $\lvert dz\rvert < 3$ cm
K^+	$KaonID\ \frac{\mathcal{L}_K}{\mathcal{L}_\pi + \mathcal{L}_K} > 0.4$	$KaonID\ \frac{\mathcal{L}_K}{\mathcal{L}_\pi + \mathcal{L}_K} > 0.4$
π^+	$PionID\ \frac{\mathcal{L}_\pi}{\mathcal{L}_\pi + \mathcal{L}_K} > 0.4$	$PionID\ \frac{\mathcal{L}_\pi}{\mathcal{L}_\pi + \mathcal{L}_K} > 0.4$
γ	$E_\gamma^{barrel} > 30$ MeV $E_\gamma^{forward} > 120$ MeV $E_\gamma^{backward} > 80$ MeV clusterE1E9 > 0.4 0.5 < clusterTheta < 2.6180 clusterNHits > 1.5	E > 300 MeV clusterE1E9 > 0.6 0.5 < clusterTheta < 2.6180 clusterNHits > 1.5
π^0	$0.121 < M(\gamma\gamma) < 0.142$ GeV/c^2 -1.2 < $\Delta\phi$ < 1.2 daughterAngle(0,1) < 1 Mass Fit	- - - -
D_s^+	$1.93 < M < 2.01$ GeV/c^2	$1.93 < M < 2.01$ GeV/c^2
D_s^{*+}	$0.135 < \Delta M < 0.16$ GeV/c^2 $p^*(D_s^{*+}) > 2.5$ GeV/c	$0.1 < \Delta M < 0.18$ GeV/c^2 $p^*(D_s^{*+}) > 2.5$ GeV/c

Table 4.1: Summary of the selection cuts and criteria used in the reconstruction of $D_s^{*+} \to D_s^+ \pi^0$ and $D_s^{*+} \to D_s^+ \gamma$ modes.

the ROE and the invariant mass is required to be within 0.08 GeV/c^2 $< M <$ 0.2 GeV/c^2. There are multiple π^0 candidates but only π^0 candidate with minimum χ^2 is selected for the analysis. Here, χ^2 is defined as ((Invariant mass - nominal PDG mass)/σ)^2. Further event is rejected if the selected π^0 has χ^2 larger than 0.2. This condition helps in substantial, $\sim$ 67%, reduction in background from π^0 with about 20% of the signal loss.

4.3.5 Best Candidate Selection (BCS)

After applying all the selection cuts, the multiplicity of D_s^{*+} candidates is found to be less than 1% for each decay mode used in this study. Candidate multiplicity is defined as the number of events that have more than one candidate out of a total number of events. Out of multiple D_s^{*+} candidates, only one candidate with the reconstructed mass closest to the nominal D_s^{*+} mass will retain. Table 4.2 summarizes the candidate multiplicity and BCS efficiency corresponding to different decay modes. BCS efficiency is defined as

$$\epsilon_{BCS} = \frac{\text{Number of correct candidates selected in BCS}}{\text{Number of true events having candidate multiplicity } > 1}$$

Decay mode	Candidate Multiplicity(%)	Efficiency of BCS(%)
$D_s^{*+} \to D_s^+(\phi\pi^+)\pi^0$	0.04	99.1
$D_s^{*+} \to D_s^+(\bar{K}^{*0}K^+)\pi^0$	0.08	98.2
$D_s^{*+} \to D_s^+(\phi\pi^+)\gamma$	0.07	98.5
$D_s^{*+} \to D_s^+(\bar{K}^{*0}K^+)\gamma$	0.05	90.0

Table 4.2: Candidate multiplicity and efficiency of best candidate selection corresponding to different decay channels.

4.4 Reconstructed D_s^{*+} candidates

After applying the above selection criteria, a clean sample of D_s^{*+} candidates is obtained. Figures 4.3 and 4.4 display the invariant mass of the D_s^+ candidate and ΔM distribution for the $D_s^{*+} \to D_s^+(\phi\pi^+)\pi^0$ and $D_s^{*+} \to D_s^+(\bar{K}^{*0}K^+)\pi^0$ decays, respectively. These distributions depict signal and background components separately. Figures 4.5 and 4.6 represent the 2D scatter plot of signal (left distribution) and background (right distribution) components between ΔM and $M(D_s^+)$ for $D_s^{*+} \to D_s^+(\phi\pi^+)\pi^0$ and $D_s^{*+} \to D_s^+(\bar{K}^{*0}K^+)\pi^0$ decays, respectively. These distributions demonstrate that there is no correlation between the ΔM and $M(D_s^+)$ variables. Therefore, there is no bias from the correlation of these two variables in parameter estimation and ensures precise measurement. The signal and the background are selected through truth matching.

Background observed in the decay mode $D_s^{*+} \to D_s^+(\phi\pi^+)\pi^0$ has two distinct

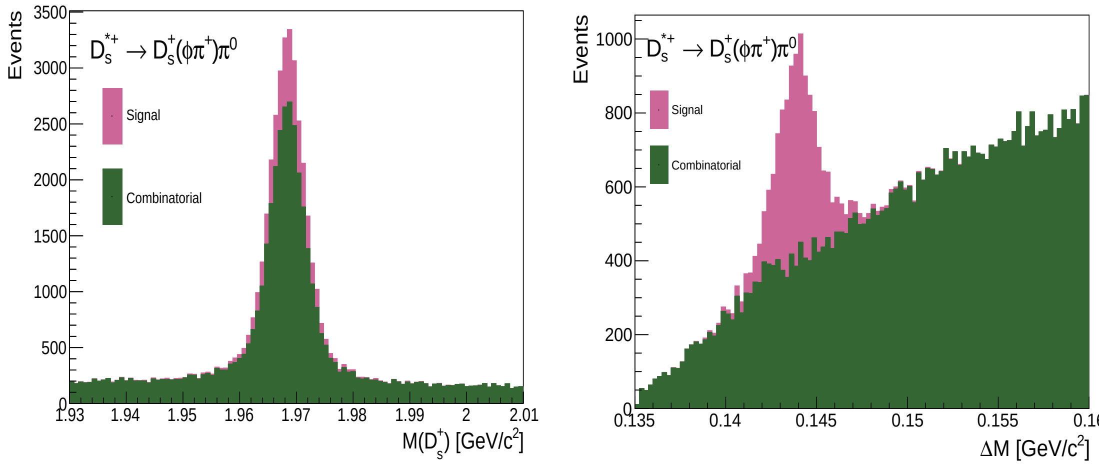

(a) (b)

Figure 4.3: (a) M(D_s^+) and (b) ΔM distributions from $D_s^{*+} \to D_s^+(\phi\pi^+)\pi^0$ decay channel, here magenta distribution is signal and the green distribution represents background from different productions. Peaking structure in M(D_s^+) background is due to the fake π^0 background.

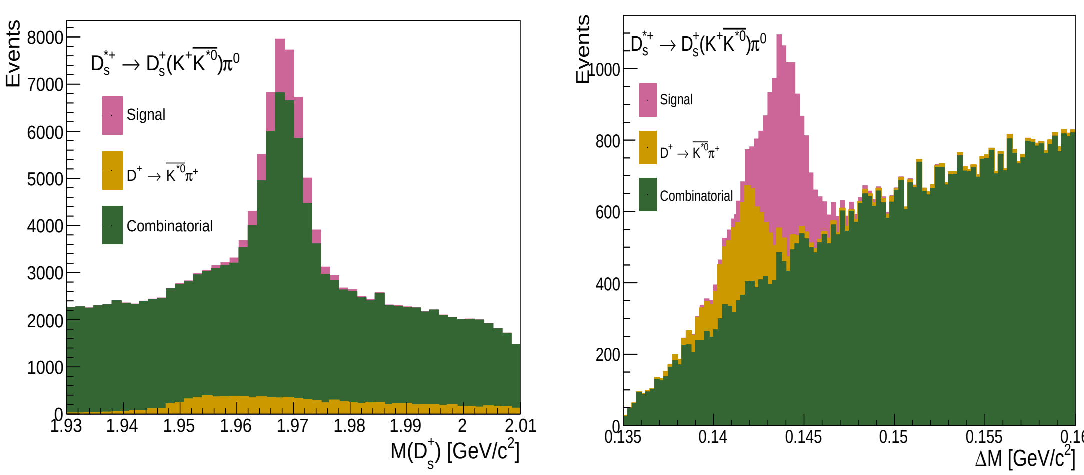

(a) (b)

Figure 4.4: (a) M(D_s^+) and (b) ΔM distributions from $D_s^{*+} \to D_s^+(\bar{K}^{*0}K^+)\pi^0$ decay channel, here magenta distribution is signal, the orange component represents $D^+ \to \bar{K}^{*0}\pi^+$ background and the green component represents fake π^0 and combinatorial backgrounds.

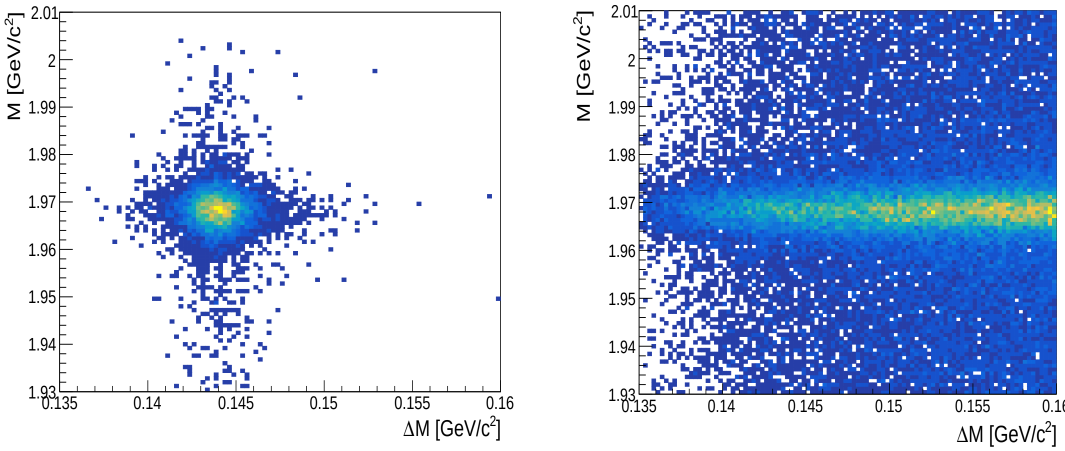

(a) (b)

Figure 4.5: M(D_s^+) vs ΔM correlation plot for $D_s^{*+} \to D_s^+(\phi\pi^+)\pi^0$ (a) signal and associated (b) background events

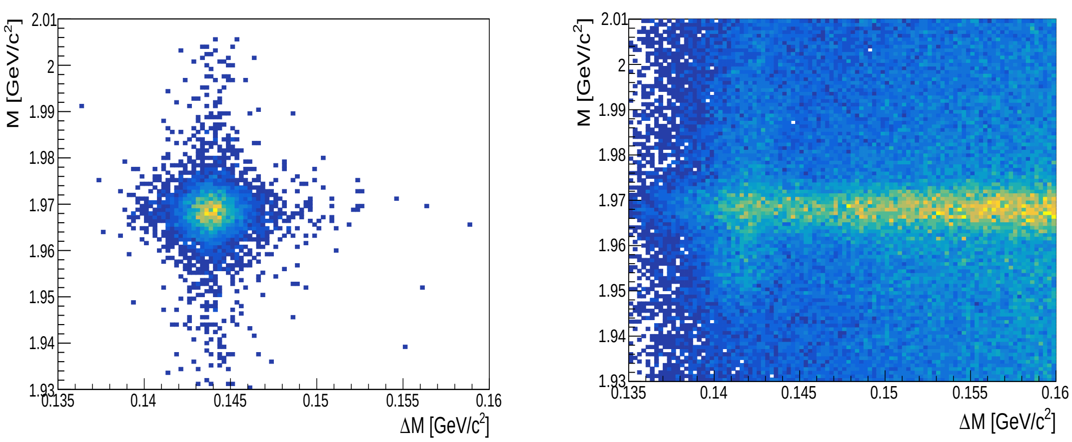

(a) (b)

Figure 4.6: M(D_s^+) vs ΔM correlation plot for $D_s^{*+} \to D_s^+(\bar{K}^{*0}K^+)\pi^0$ (a) signal and associated (b) background events

components. First, there is a contribution from fake π^0 candidates resulting from fake or mis-reconstructed π^0 candidates combined with genuine D_s^+ candidates. A peaking structure in $M(D_s^+)$ is observed due to this fake π^0 background. Second, the background also includes a combinatorial component.

For the $D_s^{*+} \to D_s^+(\bar{K}^{*0}K^+)\pi^0$ decay channel, the background is primarily due to three sources: due to the fake or mis-reconstructed π^0 candidates, $D^+ \to \bar{K}^{*0}\pi^+$ decay and combinatorial background. The background that arises from $D^+ \to \bar{K}^{*0}\pi^+$ decay has a peaking structure in the lower signal region of the ΔM distribution.

Figures 4.7 and 4.8 illustrate the invariant mass of the D_s^+ candidate and ΔM distribution for $D_s^{*+} \to D_s^+(\phi\pi^+)\gamma$ and $D_s^{*+} \to D_s^+(\bar{K}^{*0}K^+)\gamma$ decays, respectively. These distributions show signal and background components separately. Figures 4.9 and 4.10 represent the 2D scatter plot of signal (left distribution) and background (right distribution) components between ΔM and $M(D_s^+)$ for $D_s^{*+} \to D_s^+(\phi\pi^+)\gamma$ and $D_s^{*+} \to D_s^+(\bar{K}^{*0}K^+)\gamma$ decays, respectively. Similarly to the previous case, these distributions demonstrate no correlation between the ΔM and $M(D_s^+)$ variables, therefore, there is no bias these variables in parameter estimation.

In the $D_s^{*+} \to D_s^+\gamma$ decays, there are three different background contributions. Firstly, there is a fake γ background arises from the fake or mis-reconstructed γ candidates recombining with the genuine D_s^+ candidates which result in the peaking structure in the $M(D_s^+)$ distribution. Secondly, there is a background due to fake D_s^+ candidates combined with real γ candidates that leads to the peaking structure in ΔM distribution, although its contribution is minimal. Lastly, the background also includes a combinatorial component.

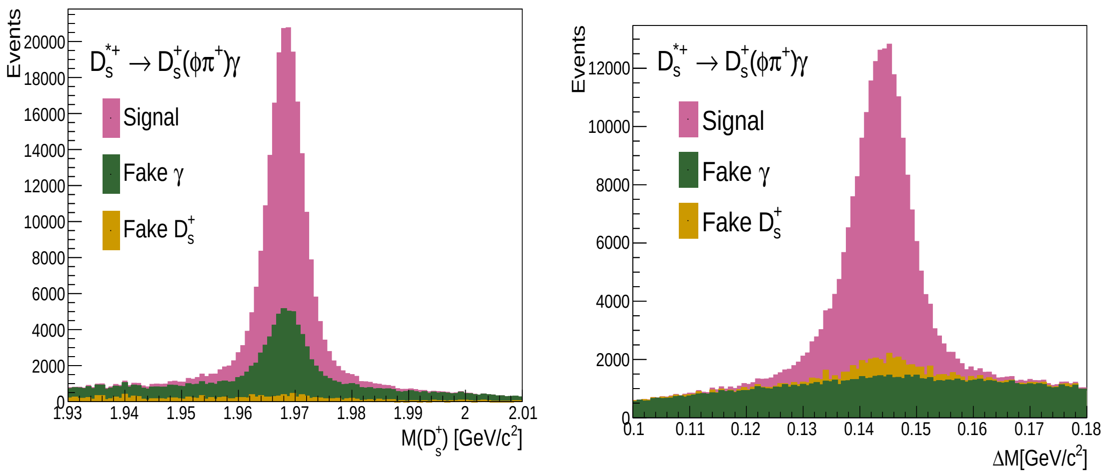

(a) (b)

Figure 4.7: (a) M(D_s^+) and (b) ΔM distributions from $D_s^{*+} \to D_s^+(\phi\pi^+)\gamma$ decay channel, here magenta distribution is signal, the orange component represents the fake D_s^+ background and the green component represents fake γ and combinatorial backgrounds.

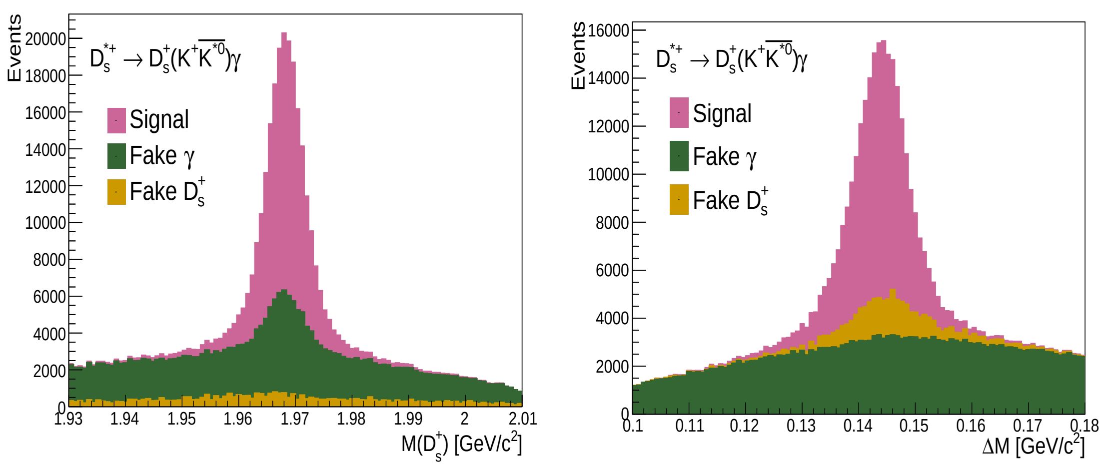

(a) (b)

Figure 4.8: (a) M(D_s^+) and (b) ΔM distributions from $D_s^{*+} \to D_s^+(\bar{K}^{*0}K^+)\gamma$ decay channel, here magenta distribution is signal, the orange component represents the fake D_s^+ background and the green component represents fake γ and combinatorial backgrounds.

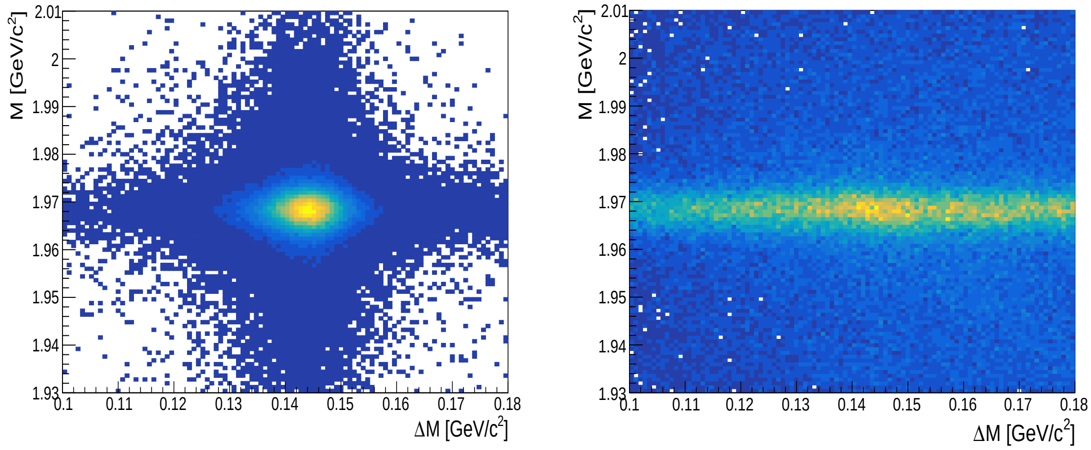

(a) (b)

Figure 4.9: M(D_s^+) vs ΔM correlation plot for $D_s^{*+} \to D_s^+(\phi\pi^+)\gamma$ (a) signal and associated (b) background events.

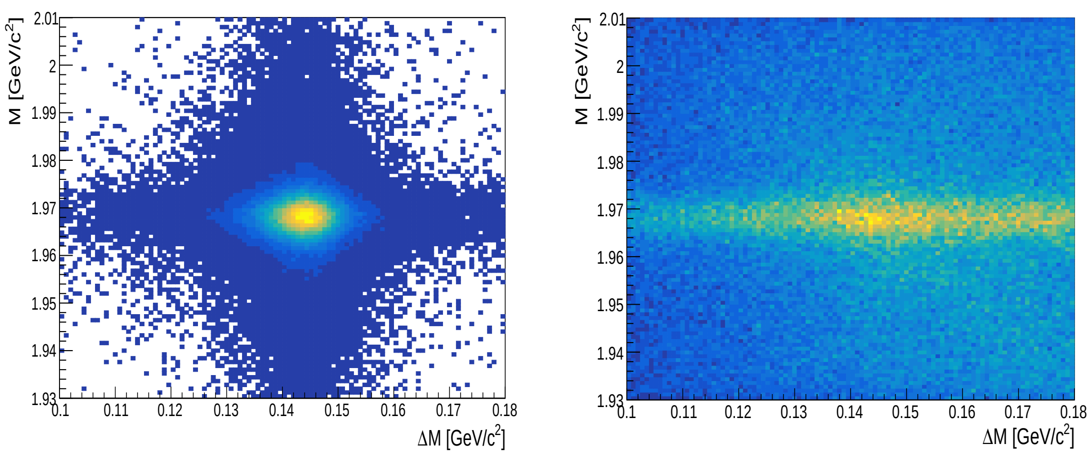

(a) (b)

Figure 4.10: M(D_s^+) vs ΔM correlation plot for $D_s^{*+} \to D_s^+(\bar{K}^{*0}K^+)\gamma$ (a) signal and associated (b) background events.

These signal regions have varying signal purity i.e. 25-80% for different modes. The signal purity for different modes is summarized in the Table 4.3. These selected event samples fitted to extract the signal yield as discussed in the subsequent sections.

Process	Purity(%)
$D_s^{*+} \to D_s^+(\phi\pi^+)\pi^0$	45
$D_s^{*+} \to D_s^+(\bar{K}^{*0}K^+)\pi^0$	24
$D_s^{*+} \to D_s^+(\phi\pi^+)\gamma$	82
$D_s^{*+} \to D_s^+(\bar{K}^{*0}K^+)\gamma$	74

Table 4.3: Purity of the decay modes of interest within the signal region.

4.5 Probability Density Functions

To determine the signal selection efficiency and to extract the signal yield, a two-dimensional fitting of the invariant mass of D_s^+ and the ΔM distributions is performed. Probability Density Functions (PDFs) are used to fit signal and background components as discussed below.

4.5.1 PDFs for $D_s^{*+} \to D_s^+\pi^0$ mode

For ΔM, the Johnson function [19] is used to model the signal contribution in the $D_s^{*+} \to D_s^+(\phi\pi^+)\pi^0$ and $D_s^{*+} \to D_s^+(\bar{K}^{*0}K^+)\pi^0$ decays. Johnson function is defined as:

$$PDF_{\Delta M}^{sig} = \frac{\delta(2\pi)^{-\frac{1}{2}}}{\sigma_{\Delta M}\sqrt{1+\left(\frac{\Delta M-\mu_{\Delta M}}{\sigma_{\Delta M}}\right)^2}} \exp\left[-\frac{1}{2}\left(\gamma+\delta\sinh^{-1}\left(\frac{\Delta M-\mu_{\Delta M}}{\sigma_{\Delta M}}\right)\right)^2\right] \tag{4.4}$$

Here, μ and σ are the mean and the width of the distribution whereas δ and γ are the shape parameters.

To model signal contribution in M(D_s^+) distribution, the sum of two Gaussian functions and a bifurcated Gaussian function is used,

$$PDF_M^{sig} = f_1^s \cdot DG(M;\mu_M,\sigma_M,\sigma_1,f_2^s) + (1-f_1^s)\cdot G_{bg}(M;\mu_M,\sigma_L,\sigma_R) \tag{4.5}$$

Here, $DG(M;\mu_M,\sigma_M,\sigma_1,f_2^s)$ is the double Gaussian function that represents the sum of two Gaussian functions defined as:

$$DG(M;\mu_M,\sigma_M,\sigma_1,f_2^s) = f_2^s \cdot G(M;\mu_M,\sigma_M) + (1-f_2^s)\cdot G(M;\mu_M,\sigma_1) \tag{4.6}$$

where, $\sigma_1 = s \times \sigma_M$ and the Gaussian function is defined as:

$$G(M;\mu,\sigma) = \frac{1}{\sigma\sqrt{2\pi}} \exp\left(-\frac{1}{2}\frac{(M-\mu)^2}{\sigma^2}\right) \tag{4.7}$$

and G_{bg}(M; μ_M, σ_{bg}) is a bifurcated Gaussian function and is defined as:

$$G_{bg}(M;\mu,\sigma_{bg}) = \frac{1}{\sigma_{bg}\sqrt{2\pi}} \exp\left(-\frac{1}{2}\frac{(M-\mu)^2}{\sigma_{bg}^2}\right) \tag{4.8}$$

where, $\sigma_{bg} = \sigma_L$ for M $< \mu$ and $\sigma_{bg} = \sigma_R$ for M $\geq \mu$

To model the combinatorial and fake π^0 background contribution in ΔM distribution, the threshold function is used and defined as:

$$PDF_{\Delta M}^{bkg} = \left(1-\exp\left(-\frac{\Delta M - m_0}{C}\right)\right)\cdot\left(\frac{\Delta M}{m_0}\right)^A + B\cdot\left(\frac{\Delta M}{m_0}-1\right) \tag{4.9}$$

Since the fake π^0 background in the M(D_s^+) distribution has a peaking contribution, the sum of Gaussian and bifurcated Gaussian functions is used to fit this background.

$$PDF_M^{fake\pi^0} = f_1^b \cdot DG(M;\mu_M^b,\sigma_M^b,\sigma_1^b,f_2^b) + (1-f_1^b)\cdot G_{bg}(M;\mu_M^b,\sigma_L^b,\sigma_R^b) \tag{4.10}$$

where, $\mu_M^b = \delta^b + \mu_M$ and $\sigma_M^b = s^b \times \sigma_M$

Variable	Signal	Combinatorial Bkg	fake π^0
ΔM	Johnson	Threshold function	Threshold function
$M(D_s^+)$	Double Gauss. + Bifurcated Gauss.	2^{nd} order Chebyshev polynomial	Double Gauss. + Bifurcated Gauss.

Table 4.4: Summary of the PDFs for the fitting of $D_s^{*+} \to D_s^+(\phi\pi^+)\pi^0$ decay mode.

Variables	Signal	Combinatorial	$D^+ \to \bar{K}^{*0}\pi^+$ bkg.	fake π^0
ΔM	Johnson	Threshold	Gaussian	Threshold
$M(D_s^+)$	Double Gauss. + Bifurcated Gauss.	2^{nd} order Chebyshev Polynomial	2^{nd} order Chebyshev polynomial	Double Gauss. + Bifurcated Gauss.

Table 4.5: Summary of the PDFs for the fitting of $D_s^{*+} \to D_s^+(\bar{K}^{*0}K^+)\pi^0$ decay mode.

The 2^{nd} order Chebyshev polynomial function is used to fit the combinatorial background contribution in the M(D_s^+) distributions.

$$PDF_{bkg}(M; a_1, a_2) = f.(a_1 M^2 + a_2 M + 1) \tag{4.11}$$

In $D_s^{*+} \to D_s^+(K^{*\bar{0}}K^+)\pi^0$ decay mode, there is also a background contribution from $D^+ \to \bar{K}^{*0}\pi^+$ decay which is peaking in the ΔM and flat in the M(D_s^+) distribution. To fit this background contribution in ΔM, the Gaussian function is used and to fit this in M(D_s^+), a 2^{nd} order Chebyshev polynomial function is used.

PDFs for $D_s^{*+} \to D_s^+(\phi\pi^+)\pi^0$ and $D_s^{*+} \to D_s^+(\bar{K}^{*0}K^+)\pi^0$ decays are summarized in the Tables 4.4 and 4.5, respectively.

4.5.2 PDFs for $D_s^{*+} \to D_s^+\gamma$ mode

To fit the signal contribution in ΔM, the sum of the Johnson function as mentioned in equation 4.4 and two Gaussian functions as defined in equation 4.7 is used,

$$PDF_{\Delta M}^{sig} = g_1^s \cdot DG(\Delta M; \mu_{\Delta M}, \sigma_{\Delta M}, \sigma_{\Delta M1}, g_2^s) + (1 - g_1^s) \cdot J(\Delta M; \mu_{\Delta M}, \sigma_J, \delta, \gamma) \tag{4.12}$$

Variables	Signal	Combinatorial	fake D_s^+	fake γ
ΔM	Johnson + Double Gaussian	2^{nd} order Chebyshev polynomial	Gaussian	2^{nd} order Chebyshev polynomial
$M(D_s^+)$	Double Gauss. + Bifurcated Gauss.	2^{nd} order Chebyshev polynomial	2^{nd} order Chebyshev polynomial	Double Gauss. + Bifurcated Gauss.

Table 4.6: Summary of the PDFs for the fitting of $D_s^{*+} \to D_s^+(\phi\pi^+)\gamma$ and $D_s^{*+} \to D_s^+(\bar{K}^{*0}K^+)\gamma$ decay mode.

To model signal contribution for M(D_s^+) distribution, the sum of Gaussian and bifurcated Gaussian functions is used, which is defined in equation 4.5.

The fake γ background is flat in ΔM distribution and peaking in the M(D_s^+) distribution. Thus, to fit the fake γ background in ΔM, 2^{nd} order polynomial function as defined in equation 4.11 is used. To fit the peaking part of this background in M(D_s^+) distribution, the sum of the Gaussian and bifurcated Gaussian function is used.

To fit the fake D_s^+ background, the Gaussian function in ΔM distribution and the 2^{nd} order Chebyshev polynomial function in the M(D_s^+) distribution is used. To fit the combinatorial background, 2^{nd} order polynomial function is used in both the ΔM and M(D_s^+) distributions. PDFs for the fitting of $D_s^{*+} \to D_s^+(\phi\pi^+)\gamma$ and $D_s^{*+} \to D_s^+(\bar{K}^{*0}K^+)\gamma$ decays are summarized in Table 4.6.

4.6 Signal selection efficiency

As discussed in the Section 4.1, the ratio of branching fraction given by the equation 4.1, requires to measure ratio of the selection efficiency of the $D_s^{*+} \to D_s^+\pi^0$ and $D_s^{*+} \to D_s^+\gamma$ modes. The selection efficiency can be factorized as;

$$\epsilon(D_s^{*+} \to D_s^+\gamma) = \epsilon(D_s^+) \times \epsilon(\gamma) \times \epsilon(\text{combining } D_s^+ \text{ with } \gamma) \tag{4.13}$$

$$\epsilon(D_s^{*+} \to D_s^+\pi^0) = \epsilon(D_s^+) \times \epsilon(\pi^0) \times \epsilon(\text{combining } D_s^+ \text{ with } \pi^0) \tag{4.14}$$

Here, the important component is ratio of selection efficiency of γ and π^0. This ratio can be measured using collision data in control channels such as $\eta \to \pi^+\pi^-\pi^0$ and $\eta \to \pi^+\pi^-\gamma$ as referenced in the $\epsilon(\pi^0)$ correction study [20]. Following method is used to compute the ratio of efficiencies:

$$N(\eta \to \pi^+\pi^-\pi^0) = \epsilon(\eta \to \pi^+\pi^-\pi^0) \times N(\eta) \times \mathcal{B}(\eta \to \pi^+\pi^-\pi^0) \tag{4.15}$$

$$N(\eta \to \pi^+\pi^-\gamma) = \epsilon(\eta \to \pi^+\pi^-\gamma) \times N(\eta) \times \mathcal{B}(\eta \to \pi^+\pi^-\gamma) \tag{4.16}$$

The efficiencies are expressed as follows:

$$\epsilon(\eta \to \pi^+\pi^-\pi^0) = \epsilon(\pi^+) \times \epsilon(\pi^-) \times \epsilon(\pi^0) \times \epsilon(\text{combining } \pi^+\pi^- \text{ with } \pi^0) \tag{4.17}$$

$$\epsilon(\eta \to \pi^+\pi^-\gamma) = \epsilon(\pi^+) \times \epsilon(\pi^-) \times \epsilon(\gamma) \times \epsilon(\text{combining } \pi^+\pi^- \text{ with } \gamma) \tag{4.18}$$

The ratio $\epsilon(\pi^0)/\epsilon(\gamma)$ is then obtained as:

$$\frac{\epsilon(\pi^0)}{\epsilon(\gamma)} \sim \frac{\epsilon(\eta \to \pi^+\pi^-\pi^0)}{\epsilon(\eta \to \pi^+\pi^-\gamma)} = \frac{N(\eta \to \pi^+\pi^-\pi^0)}{N(\eta \to \pi^+\pi^-\gamma)} \times \frac{\mathcal{B}(\eta \to \pi^+\pi^-\gamma)}{\mathcal{B}(\eta \to \pi^+\pi^-\pi^0)} \tag{4.19}$$

For the reconstruction of these control processes, the selection criteria is the same, as discussed earlier, for the tracks, γ, and π^0. In addition, invariant mass is required to lie in the window [0.52, 0.58] GeV/c^2 with resulting momentum larger than 2 GeV. There is a significant difference in the kinematics of η and D_s^+ as shown in Figure 4.11, which can introduce differences in the measured efficiencies.

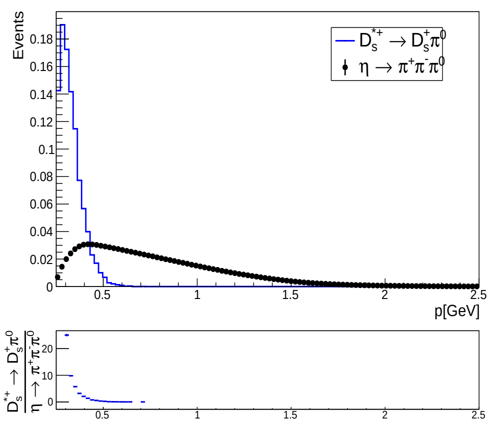

(a)

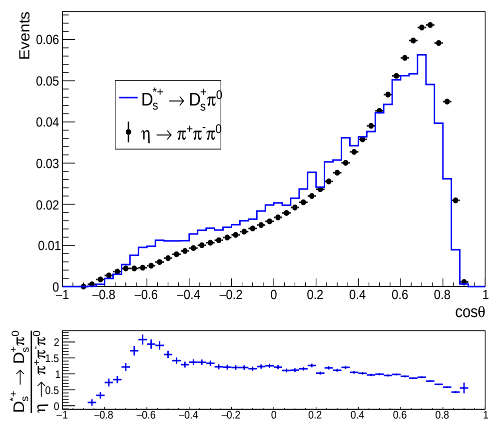

(b)

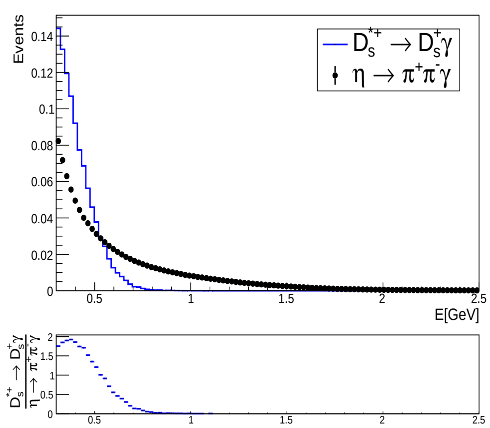

(c)

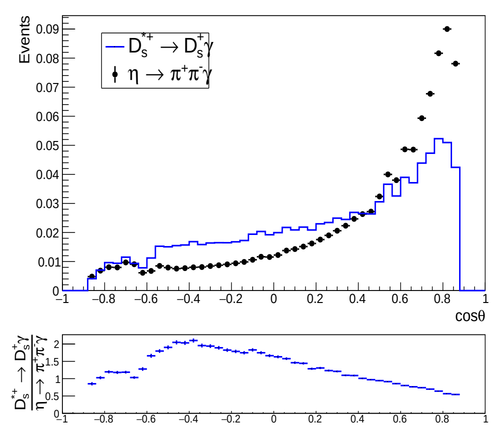

(d)

Figure 4.11: Shape comparison distributions of (a)p_{π^0}, (b) $cos\theta_{\pi^0}$, (c)E_γ and (d) $cos\theta_\gamma$ between η and D_s^{*+} decays from data. Blue plots are for D_s^{*+}'s decays and black points are from η's decays. Lower plots show the ratio between D_s^{*+} and η decays.

This difference is taken into account by a 2D reweighting procedure. Here, the weights are calculated in the bins of the p_{π^0}/E_γ and $cos(\theta_{\pi^0/\gamma})$ which are applied bin-by-bin to the events for control processes. Figure 4.12 illustrates the kinematic shape comparison of π^0 and γ after reweighting.

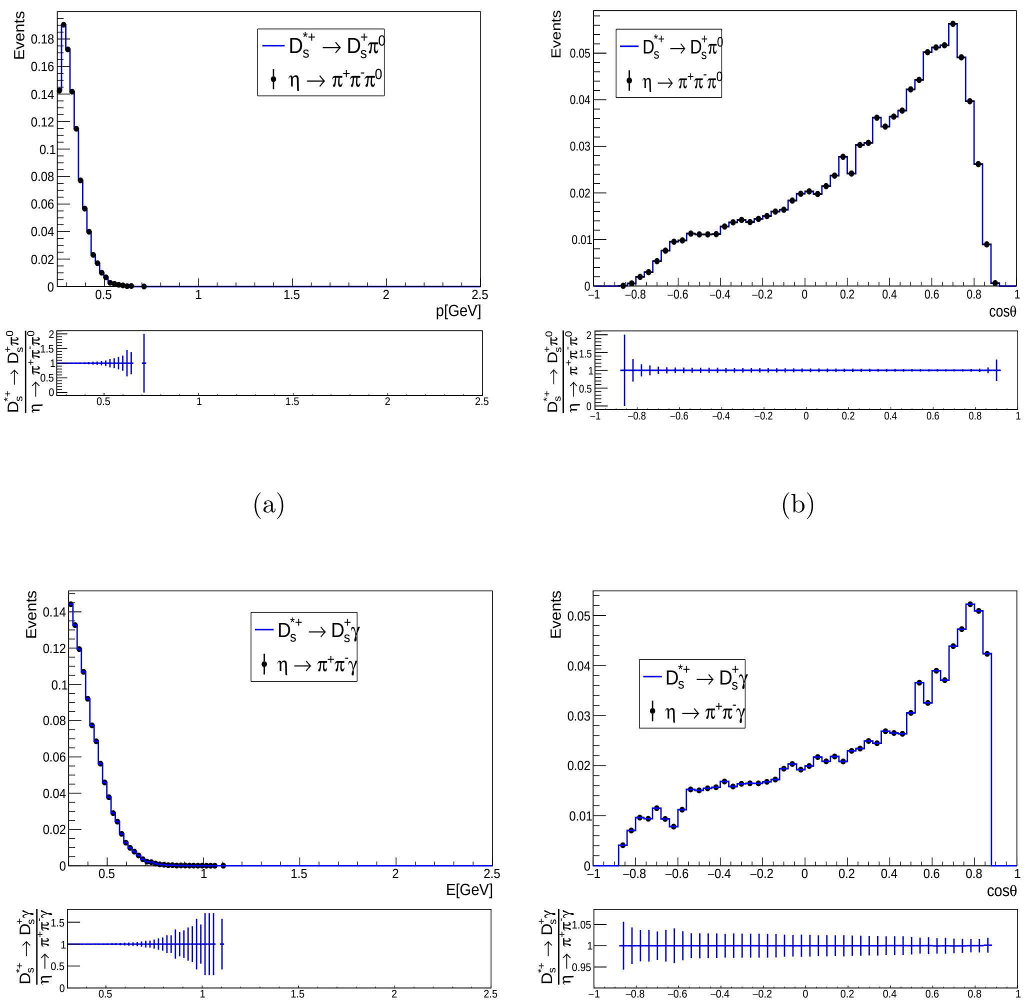

(a) (b)

(c) (d)

Figure 4.12: Shape comparison distributions of (a)p_{π^0}, (b) $cos\theta_{\pi^0}$, (c)E_γ and (d) $cos\theta_\gamma$ between η and D_s^{*+} decays from data after reweighting. Blue plots are for D_s^{*+}'s decays and black points are from η's decays. Lower plots show the ratio between D_s^{*+} and η decays.

Signal yields are extracted by fitting the reweighted $M(\eta)$ distribution in both generic MC and data. For signal fitting, a sum of two Gaussian and bifurcated Gaussian functions is utilized, while a 1^{st} order polynomial function is employed for background fitting. Figures 4.13 and 4.14 depict the fitting of the weighted $M(\eta)$ distribution for simulation and real data, respectively. In Table 4.7, a summary of the measurement of $\epsilon(\pi^0)/\epsilon(\gamma)$ following the reweighting process in both simulation and data is presented. The ratio of selection efficiencies of π^0 and γ, $\epsilon(\pi^0)/\epsilon(\gamma)$, is measured to be 0.699 ± 0.010 and 0.640 ± 0.006 for data and simulations, respectively.

Observables	Data (424 fb^{-1})	Simulations (400 fb^{-1})
$N(\eta \to \pi^+\pi^-\pi^0)$	1544885 ± 3547	744192 ± 3123
$N(\eta \to \pi^+\pi^-\gamma)$	410892 ± 1631	235166 ± 2074
$\mathcal{B}(\eta \to \pi^+\pi^-\pi^0)$	0.2302 ± 0.0025	0.2274
$\mathcal{B}(\eta \to \pi^+\pi^-\gamma)$	0.0428 ± 0.0007	0.046
$\epsilon(\pi^0)/\epsilon(\gamma)$	0.699 ± 0.010	0.640 ± 0.006

Table 4.7: Signal yields, branching fractions and $\epsilon(\gamma)$ in data and simulations after reweighting of η decay modes

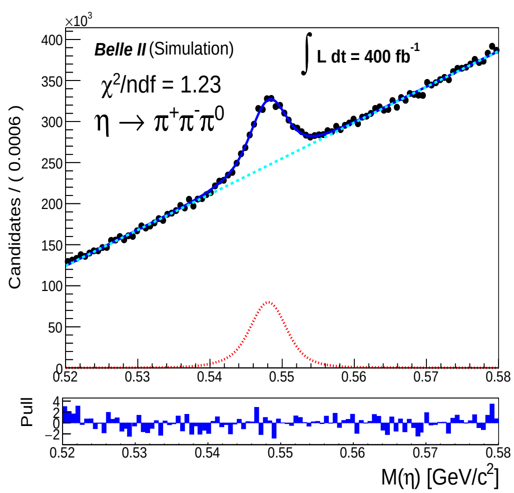

(a)

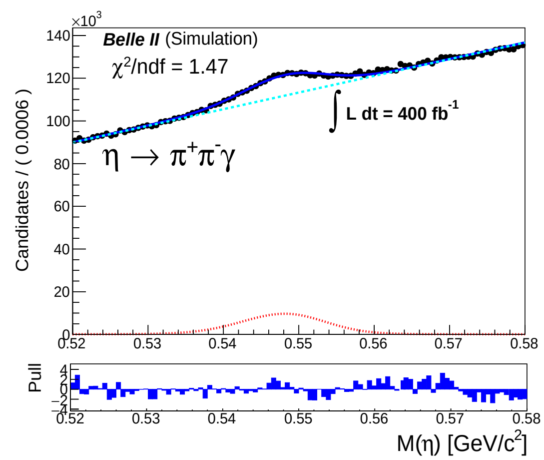

(b)

Figure 4.13: 1D unbinned maximum likelihood fitted M(η) distribution in (a) $\eta \to \pi^+\pi^-\pi^0$ and (b) $\eta \to \pi^+\pi^-\gamma$ decay modes in generic MC samples (400 fb^{-1}), blue curve shows total fit, black points are data points, red dotted represents signal and cyan dashed lines represent background.

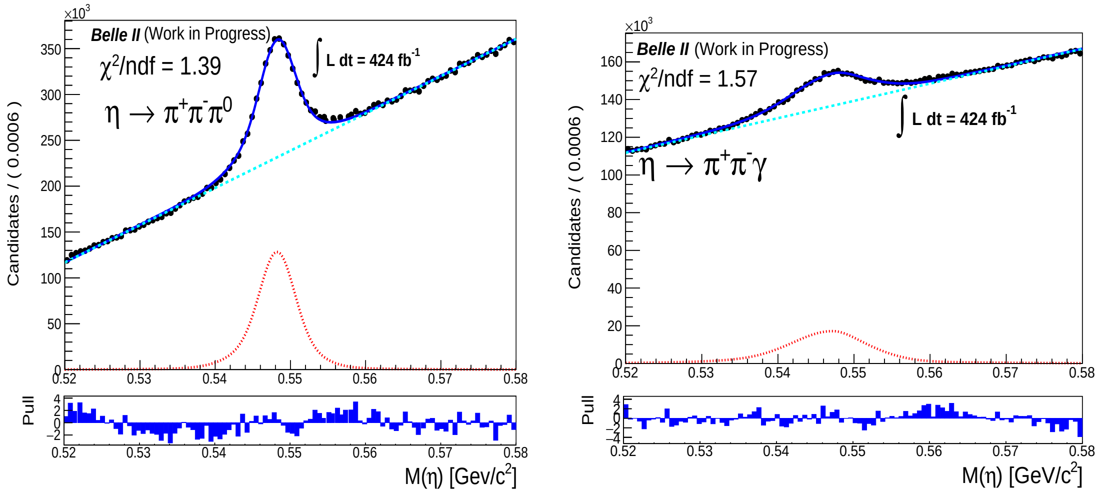

(a) (b)

Figure 4.14: 1D unbinned maximum likelihood fitted M(η) distribution in (a) $\eta \to \pi^+\pi^-\pi^0$ and (b) $\eta \to \pi^+\pi^-\gamma$ decay modes in Belle II data including proc13 and prompt dataset corresponding to 424 fb^{-1}, blue curve shows total fit, black points are data points, red dotted represents signal and cyan dashed lines represent background.

4.7 Signal yield extraction

The signal yield is extracted by two-dimensional extended maximum likelihood fit of the $M(D_s^+)$ and ΔM for the $D_s^{*+} \to D_s(\phi\pi^+)\pi^0$, $D_s^{*+} \to D_s^+(\bar{K}^{*0}K^+)\pi^0$, $D_s^{*+} \to D_s^+(\phi\pi^+)\gamma$, and $D_s^{*+} \to D_s^+(\bar{K}^{*0}K^+)\gamma$ decay channels for the data events. The fitting is performed using the signal and background PDFs as discussed in Section 4.6. Before getting there, it is important to validate fitting setup with MC samples.

To extract the signal yield from MC samples during fitting, the mean, sigma and yield of the signal and background are allowed to vary. Whereas the shape parameters of the signal PDFs are fixed as derived from the fitting of signal MC samples. Furthermore, the background parameters of the non-peaking background are determined by separately fitting the background distributions from the generic

MC samples.

For the peaking backgrounds (fake π^0 background in case of $D_s^{*+} \to D_s^+\pi^0$ decays and fake γ and fake D_s^+ background in $D_s^{*+} \to D_s^+\gamma$ decays) in $M(D_s^+)$ and ΔM, the mean and sigma parameters are parameterized based on those of the signal while maintaining a fixed shape from MC. Figures 4.15, 4.16, 4.17, and 4.18 illustrates the two-dimensional unbinned maximum likelihood fitting of the ΔM and $M(D_s^+)$ distributions for the $D_s^{*+} \to D_s^+(\phi\pi^+)\pi^0$, $D_s^{*+} \to D_s^+(\bar{K}^{*0}K^+)\pi^0$, $D_s^{*+} \to D_s^+(\phi\pi^+)\gamma$, and $D_s^{*+} \to D_s^+(\bar{K}^{*0}K^+)\gamma$ decay channels. Table 4.8 compares the signal yield extracted from the fitting and the yield estimated for the integrated luminosity of 424 fb^{-1}. The signal yield extracted from the fitting is consistent with the MC predictions which establishes the robustness of the fitting setup.

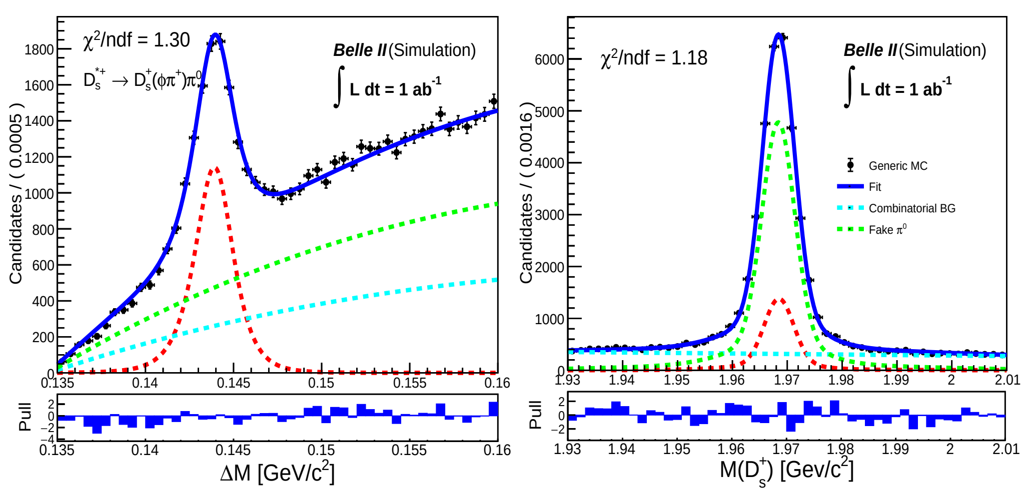

Figure 4.15: The 2D unbinned maximum likelihood fitted MC distribution of ΔM (left) and $M(D_s^+)$ (right) for the $D_s^{*+} \to D_s^+(\phi\pi^+)\pi^0$ mode. The data is shown by black markers whereas contribution of signal, combinatorial background and fake π^0 background is shown with red dotted, green dashed and cyan dashed, respectively. The bottom panel shows the pull distributions.

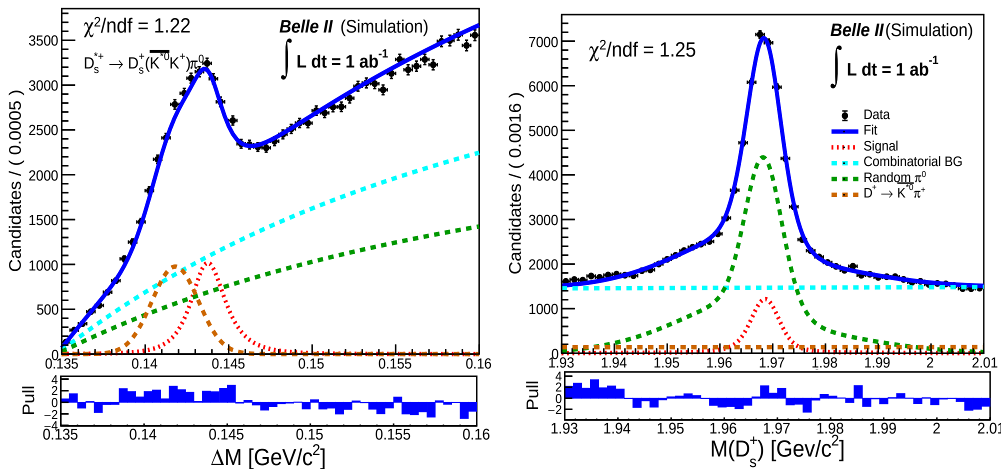

Figure 4.16: The 2D unbinned maximum likelihood fitted MC distribution of ΔM (left) and $M(D_s^+)$ (right) for the $D_s^{*+} \to D_s^+(\bar{K}^{*0}K^+)\pi^0$ mode. The data is shown by black markers whereas contribution of signal, combinatorial background, $D^+ \to \bar{K}^{*0}\pi^+$ background and fake π^0 background is shown with red dotted, green dashed, orange dashed and cyan dashed lines, respectively. The bottom panel shows the pull distributions.

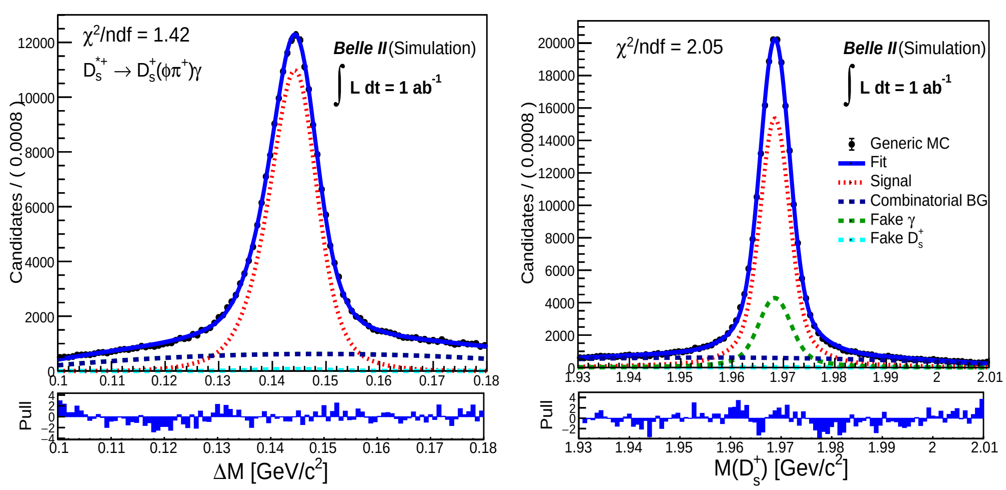

Figure 4.17: The 2D unbinned maximum likelihood fitted MC distribution of ΔM (left) and $M(D_s^+)$ (right) for the $D_s^{*+} \to D_s^+(\phi\pi^+)\gamma$ mode. The data is shown by black markers whereas contribution of signal, combinatorial background, fake γ and fake D_s^+ backgrounds is shown with red dotted, green dashed, cyan dashed and purple dashed lines, respectively. The bottom panel shows the pull distributions.

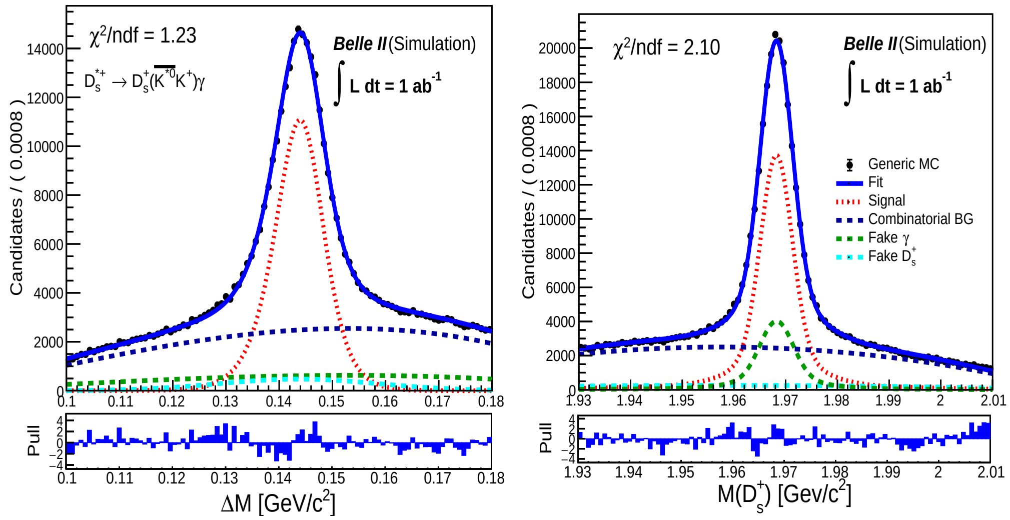

Figure 4.18: The 2D unbinned maximum likelihood fitted MC distribution of ΔM (left) and $M(D_s^+)$ (right) for the $D_s^{*+} \to D_s^+(\bar{K}^{*0}K^+)\gamma$ mode. The data is shown by black markers whereas contribution of signal, combinatorial background, fake γ and fake D_s^+ backgrounds is shown with red dotted, green dashed, cyan dashed and purple dashed lines, respectively. The bottom panel shows the pull distributions.

Process	Yield scaled at 424 fb^{-1}	Expected yield at 424 fb^{-1}
$D_s^{*+} \to D_s^+(\phi\pi^+)\pi^0$	2899 ± 68	2925
$D_s^{*+} \to D_s^+(\bar{K}^{*0}K^+)\pi^0$	2885 ± 102	2939
$D_s^{*+} \to D_s^+(\phi\pi^+)\gamma$	71773 ± 373	71814
$D_s^{*+} \to D_s^+(\bar{K}^{*0}K^+)\gamma$	70987 ± 423	71944

Table 4.8: Signal yield (statistical uncertainty) corresponding to different decay channels and comparison between extracted signal yield and expected signal yield at 424 fb^{-1} luminosity.

The fitting procedure is further validated using the pseudo experiment with the help of MC events. The pull distribution and linearity test suggest robustness and stable performance of the fitting procedure. Figures 4.19 and 4.20 show the pull distributions for $D_s^{*+} \to D_s^+\pi^0$ and $D_s^{*+} \to D_s^+\gamma$ decay channels, respectively. Pulls are calculated as $(N_{fit} - N_{gen})/\sigma(N_{fit})$, where N_{gen} is the generated yield and N_{fit} is the fitted yield using the same PDFs employed to extract the signal yield. The pull distributions have mean and sigma consistent with 0 and 1, respectively, which establishes the robustness of the fitting method.

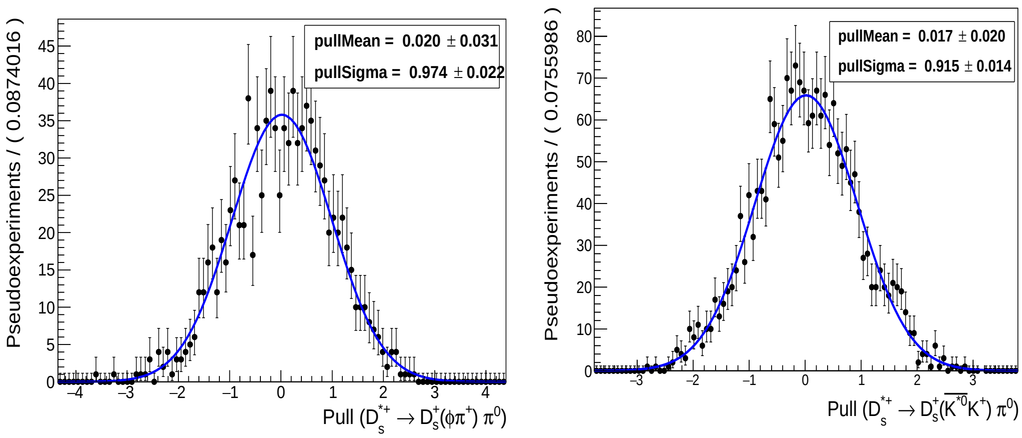

(a) (b)

Figure 4.19: Pull distributions between the fitted and generated signal yields for (a)$D_s^{*+} \to D_s^+(\phi\pi^+)\pi^0$ and (b)$D_s^{*+} \to D_s^+(\bar{K}^{*0}K^+)\pi^0$, decays.

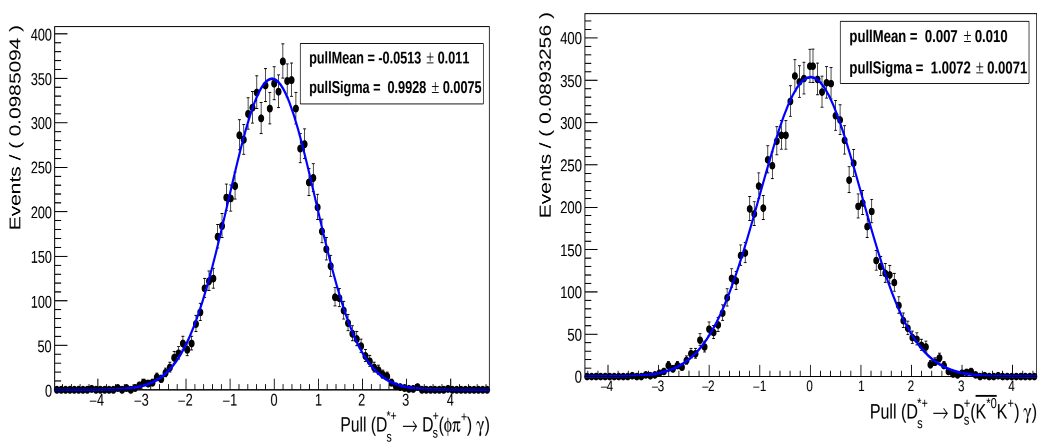

(a) (b)

Figure 4.20: Pull distributions between the fitted and generated signal yields for (a)$D_s^{*+} \to D_s^+(\phi\pi^+)\gamma$ and (b)$D_s^{*+} \to D_s^+(\bar{K}^{*0}K^+)\gamma$, decays.

In the linearity test, 1000 pseudo experiments are performed with varying signal yields. Figures 4.21 and 4.22 show the extracted yield as a function of the signal yield set in the input. It is clear from the fitted line that there is a good consistency between the input and the extracted signal yields. These closure tests establish the robustness of the fitting procedure and can be used for the fitting data distribution to extract the signal yield.

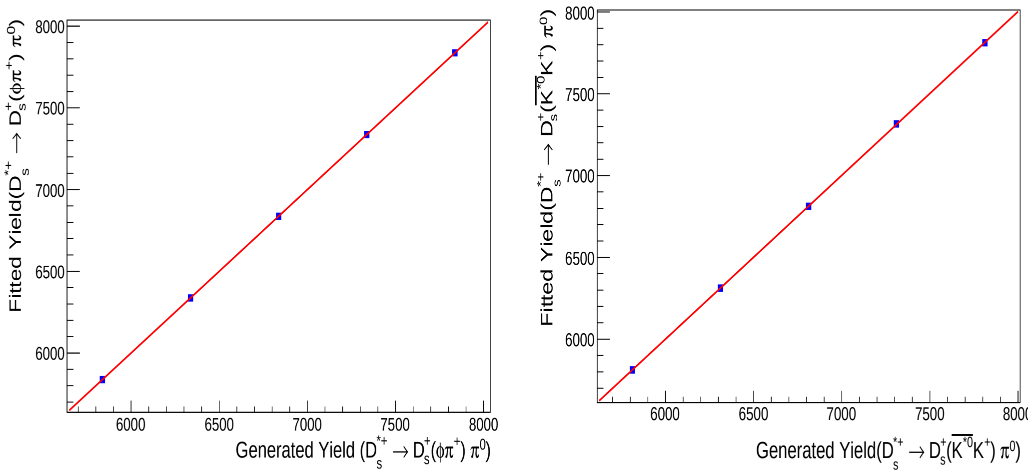

(a) (b)

Figure 4.21: Mean of the fitted signal yield vs each of the corresponding generated signal yields for (a)$D_s^{*+} \to D_s^+(\phi\pi^+)\pi^0$ and (b)$D_s^{*+} \to D_s^+(\bar{K}^{*0}K^+)\pi^0$, decays.

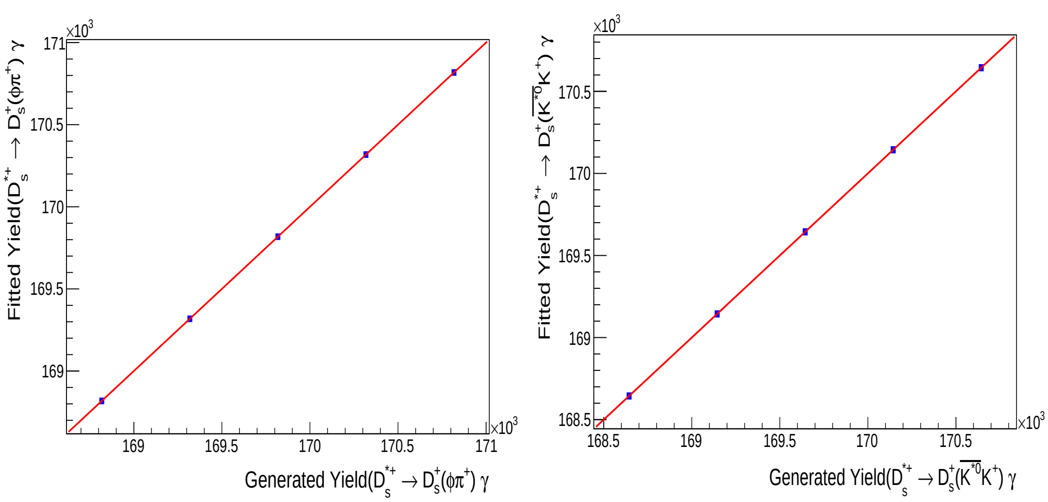

(a) (b)

Figure 4.22: Mean of the fitted signal yield vs each of the corresponding generated signal yields for (a)$D_s^{*+} \to D_s^+(\phi\pi^+)\gamma$ and (b)$D_s^{*+} \to D_s^+(\bar{K}^{*0}K^+)\gamma$, decays.

4.7.1 Yield extraction in data

After establishing the robustness of the fitting procedure, the same approach is used for the signal yield in the real data. To minimize the bias from MCs, the sigma and mean for the signal PDFs are allowed to vary. For the peaking background in $M(D_s^+)$, the mean and sigma are parameterized in such a way that these depend on the floated parameters of the signal.

Regarding the non-peaking backgrounds, the thresholds are fixed whereas the parameters of the polynomial functions are floated. Additionally, in the ΔM distribution of the $D_s^{*+} \to D_s^+(\bar{K}^{*0}K^+)\pi^0$ decay, the mean of the peaking background (from $D^+ \to \bar{K}^{*0}\pi^+$ decay) is varied. This flexible approach ensures robustness in our analysis by adjusting for any disparities between the Belle II data and MC simulations. Figures 4.23, 4.24, 4.25 and 4.26 illustrate the two-dimensional unbinned maximum likelihood fitting of the ΔM and $M(D_s^+)$ distributions for the $D_s^{*+} \to D_s^+(\phi\pi^+)\pi^0$, $D_s^{*+} \to D_s^+(\bar{K}^{*0}K^+)\pi^0$, $D_s^{*+} \to D_s^+(\phi\pi^+)\gamma$, and $D_s^{*+} \to D_s^+(\bar{K}^{*0}K^+)\gamma$ decay channels for Belle II data, respectively. The extracted signal yield from different decay channels is summarized in Table 4.9.

Process	Signal Yield (424 fb^{-1})
$D_s^{*+} \to D_s^+(\phi\pi^+)\pi^0$	1875 ± 77
$D_s^{*+} \to D_s^+(\bar{K}^{*0}K^+)\pi^0$	1932 ± 75
$D_s^{*+} \to D_s^+(\phi\pi^+)\gamma$	42398 ± 292
$D_s^{*+} \to D_s^+(\bar{K}^{*0}K^+)\gamma$	43023 ± 345

Table 4.9: Signal yield (statistical uncertainty) from Belle II data corresponding to different decay channels.

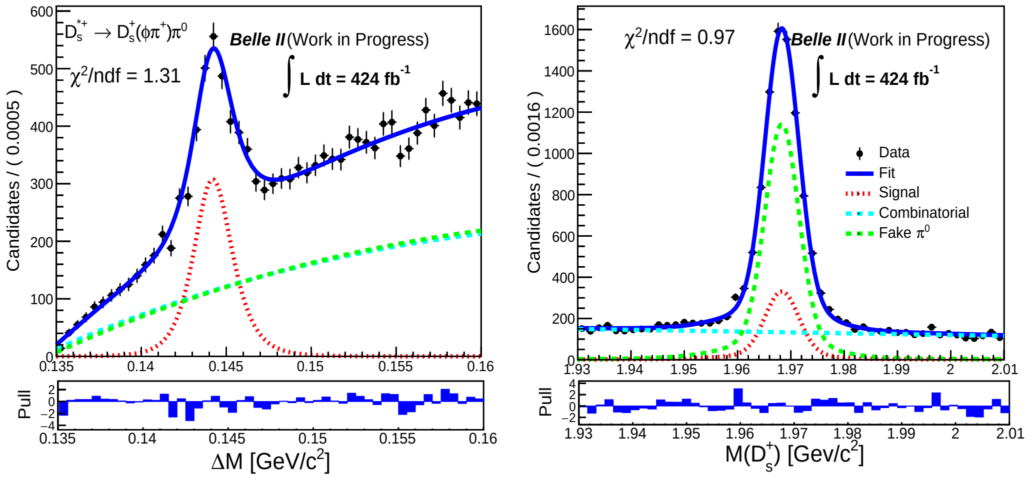

Figure 4.23: The 2D unbinned maximum likelihood fitted data distribution of ΔM (left) and $M(D_s^+)$ (right) for the $D_s^{*+} \to D_s^+(\phi\pi^+)\pi^0$ mode. The data is shown by black markers whereas contribution of signal, combinatorial and fake π^0 backgrounds is shown with red dotted, green dashed and cyan dashed lines, respectively. The bottom panel shows the pull distributions.

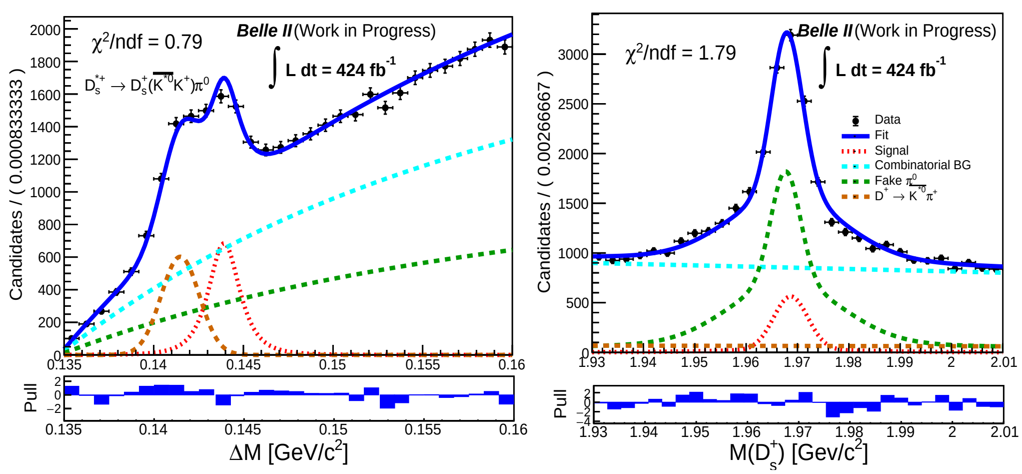

Figure 4.24: The 2D unbinned maximum likelihood fitted data distribution of ΔM (left) and $M(D_s^+)$ (right) for the $D_s^{*+} \to D_s^+(\bar{K}^{*0}K^+)\pi^0$ mode. The data is shown by black markers whereas contribution of signal, combinatorial, $D^+ \to \bar{K}^{*0}\pi^+$ and fake π^0 backgrounds is shown with red dotted, green dashed, orange dashed and cyan dashed lines, respectively. The bottom panel shows the pull distributions.

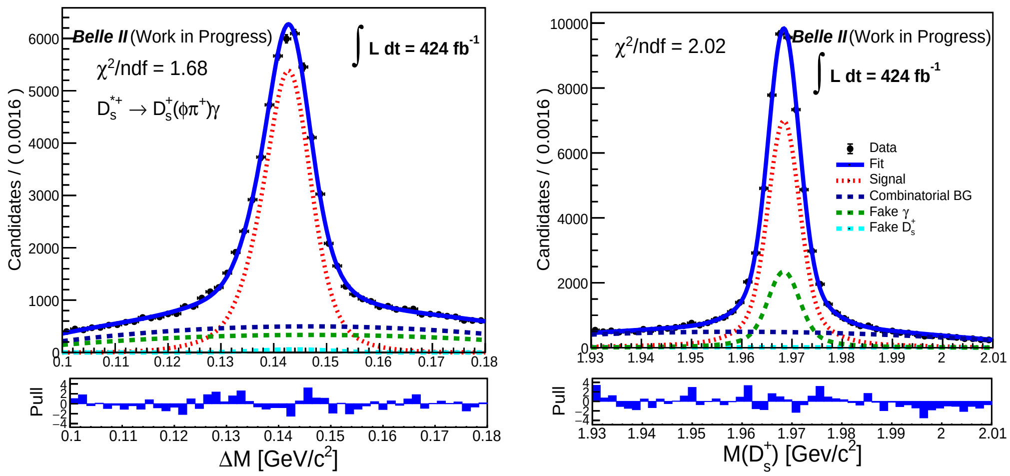

Figure 4.25: The 2D unbinned maximum likelihood fitted data distribution of ΔM (left) and $M(D_s^+)$ (right) for the $D_s^{*+} \to D_s^+(\phi\pi^+)\gamma$ mode. The data is shown by black markers whereas contribution of signal, combinatorial background, fake γ and fake D_s^+ backgrounds is shown with red dotted, green dashed, cyan dashed and purple dashed lines, respectively. The bottom panel shows the pull distributions.

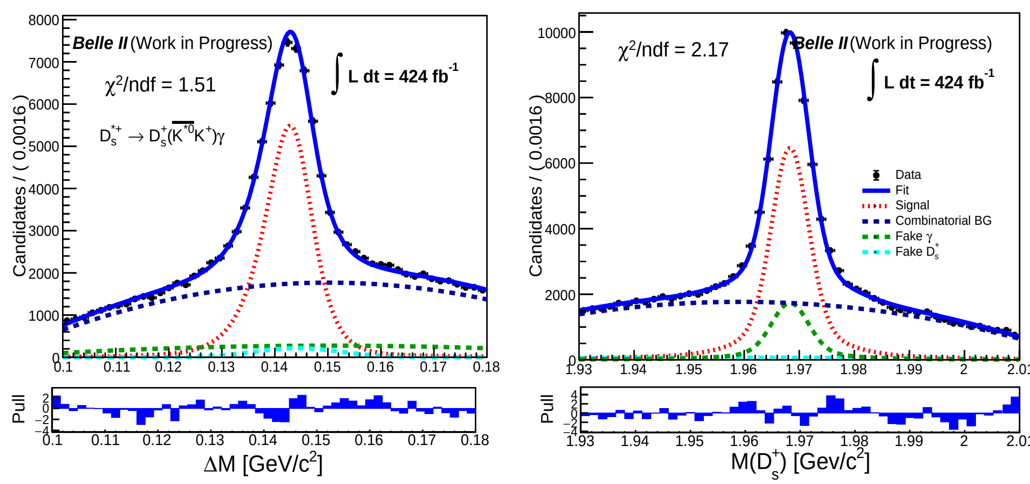

Figure 4.26: The 2D unbinned maximum likelihood fitted data distribution of ΔM (left) and $M(D_s^+)$ (right) for the $D_s^{*+} \to D_s^+(\bar{K}^{*0}K^+)\gamma$ mode. The data is shown by black markers whereas contribution of signal, combinatorial background, fake γ and fake D_s^+ backgrounds is shown with red dotted, green dashed, cyan dashed and purple dashed lines, respectively. The bottom panel shows the pull distributions.

4.8 Systematic Uncertainties

Systematic uncertainties are deviations or limitations that occur from factors such as the measurement methodology, experimental configuration and theoretical frameworks used in the analysis. Unlike statistical uncertainties, which decrease with larger data samples, systematic uncertainties are intrinsic to the measurement process and cannot be significantly reduced by increasing the dataset size. Instead, they must be quantified and included in the analysis to ensure an accurate interpretation of the results.

In the present analysis, the branching fraction of $D_s^{*+} \rightarrow D_s^+\pi^0$ is measured with respect to the branching fraction of the $D_s^{*+} \rightarrow D_s^+\gamma$, so most of the systematics will cancel in the ratio. The remaining systematics are explained in the following subsections.

4.8.1 Dependence of branching fraction on $p^*(D_s^{*+})$

The main source of systematic uncertainty (6.8%) in the BaBar study [5] was identified to be the dependence of branching fractions on center-of-mass momentum of D_s^{*+} candidate, $p^*(D_s^{*+})$. A similar procedure is adopted to obtain the associated systematic uncertainty. The measurement of $\mathcal{B}(D_s^{*+} \rightarrow D_s^+\pi^0)/\mathcal{B}(D_s^{*+} \rightarrow D_s^+\gamma)$ is repeated within intervals of $p^*(D_s^{*+})$. We fit the ratio of branching fractions as a function of p^* using both a constant function and a first-order polynomial function. Figure 4.27 displays the branching fractions as a function of p^* fitted with both a constant function and a first order polynomial function. This difference in the integral of the two fit functions is considered as a measure of the associated systematic uncertainties. The systematic uncertainty measured to be 1.6% which is significantly lower compared to that measured in BaBar.

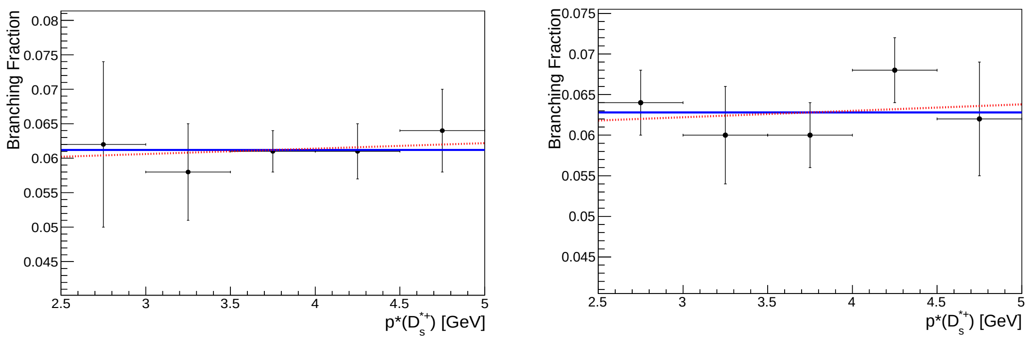

(a) (b)

Figure 4.27: Measured value of (a) $\mathcal{B}(D_s^{*+} \to D_s^+(\phi\pi^+)\pi^0)/\mathcal{B}(D_s^{*+} \to D_s^+(\phi\pi^+)\gamma)$ and (b) $\mathcal{B}(D_s^{*+} \to D_s^+(\bar{K}^{*0}K^+)\pi^0)/\mathcal{B}(D_s^{*+} \to D_s^+(\bar{K}^{*0}K^+)\gamma)$ in the intervals of $p^*(D_s^{*+})$, error bars indicate the statistical error, blue solid line and red dashed lines represent the constant fit and first order polynomial fit, respectively.

4.8.2 Measurement of $\epsilon(\pi^0)/\epsilon(\gamma)$

A reweighting process is used while measuring $\epsilon(\pi^0)/\epsilon(\gamma)$. Each weight factor has a statistical uncertainty which is considered to evaluate the systematic uncertainty due to the reweighting process. For this uncertainty, 100K toys are generated where the weight factor is varied within the associated statistical uncertainties. Figure 4.28 shows the distribution of $\epsilon(\pi^0)/\epsilon(\gamma)$ for 100K toys. This distribution follows the Gaussian function and the standard deviation of this Gaussian distribution with respect to the mean will be the uncertainty on the $\epsilon(\pi^0)/\epsilon(\gamma)$ due to reweighting.

The 1σ (0.0063) of this Gaussian distribution is considered as the systematic uncertainty and is measured as 0.9%. There is also a statistical uncertainty on $\epsilon(\pi^0)/\epsilon(\gamma)$ which is about 0.010 (1.43%), as shown in Table 4.7. These two uncertainties are added in quadrature and considered as the total systematic uncertainties due to the reweighing process in the measurement of $\epsilon(\pi^0)/\epsilon(\gamma)$. 0.012 (1.7%) is measured as the total systematic uncertainty due to the $\epsilon(\pi^0)/\epsilon(\gamma)$.

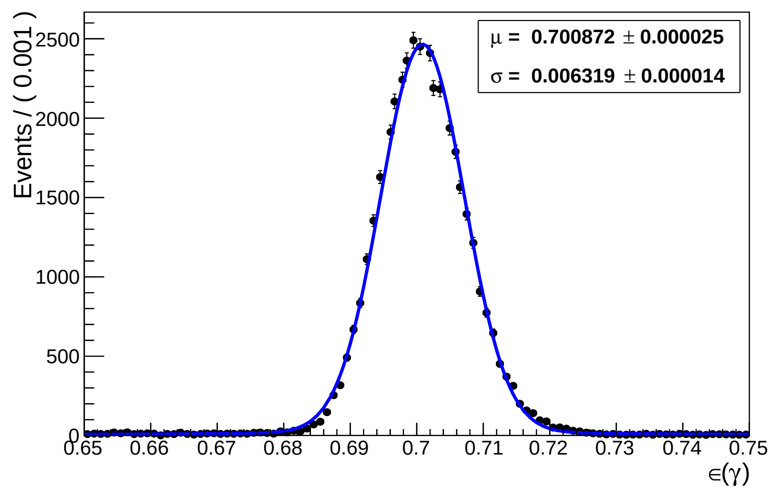

Figure 4.28: $\epsilon(\pi^0)/\epsilon(\gamma)$ distribution for 100K toys representing the Gaussian function where mean(μ) represents the $\epsilon(\pi^0)/\epsilon(\gamma)$ and the standard deviation(σ) is uncertainty.

4.8.3 Systematics on the PDFs

To estimate the systematic uncertainty due to fitting, each parameter of the fit function is varied with $\pm 1\sigma$. The quadratic sum of the changes in the branching fraction is taken as the systematic uncertainty due to the fitting. Table 4.10 summarizes the systematic uncertainties corresponding to $D_s^+ \to \phi\pi^+$ and $D_s^+ \to \bar{K}^{*0}K^+$ decay modes.

Source	$D_s^+ \to \phi\pi^+$ (%)	$D_s^+ \to \bar{K}^{*0}K^+$ (%)
Fitting	1.2	2.5
$\epsilon(\pi^0)/\epsilon(\gamma)$	1.7	1.7
$p^*(D_s^{*+})$ dependence	1.6	1.6
Total	2.62	3.42

Table 4.10: Systematic uncertainties from all three sources for both $D_s^+ \to \phi\pi^+$ and $D_s^+ \to \bar{K}^{*0}K^+$ decay modes.

4.9 Measurement of the $\frac{\mathcal{B}(D_s^{*+}\to D_s^+\pi^0)}{\mathcal{B}(D_s^{*+}\to D_s^+\gamma)}$

As discussed earlier the ratio can be written as:

$$\frac{\mathcal{B}(D_s^{*+} \to D_s^+\pi^0)}{\mathcal{B}(D_s^{*+} \to D_s^+\gamma)} = \frac{N(D_s^{*+} \to D_s^+\pi^0)}{N(D_s^{*+} \to D_s^+\gamma)} \times \frac{\epsilon(\gamma)}{\epsilon(\pi^0)} \tag{4.20}$$

The selected efficiencies and yields are measured in previous sections are summarized in Table 4.11. These numbers are used in equation 4.20 to calculate the ratio of branching fractions for different decay modes. Table 4.12 summarized the measured ratio of branching fractions for data and MC events, for $D_s^+ \to \phi\pi^+$ and $D_s^+ \to \bar{K}^{*0}K^+$ decay modes.

Observables	Data	Simulations
$N(D_s^{*+} \to D_s^+(\phi\pi^+)\pi^0)$	1875 ± 77	2899 ± 68
$N(D_s^{*+} \to D_s^+(\phi\pi^+)\gamma)$	42398 ± 292	71773 ± 373
$N(D_s^{*+} \to D_s^+(\bar{K}^{*0}K^+)\pi^0)$	1932 ± 75	2885 ± 102
$N(D_s^{*+} \to D_s^+(\bar{K}^{*0}K^+)\gamma)$	43023 ± 345	70987 ± 423
$\epsilon(\pi^0)/\epsilon(\gamma)$	0.699 ± 0.010	0.640 ± 0.006

Table 4.11: Selected efficiencies and extracted signal yields for both decay modes of D_s^+ for data and MC events.

Branching fractions	Data	Simulations
$\frac{\mathcal{B}(D_s^{*+}\to D_s^+(\phi\pi^+)\pi^0)}{\mathcal{B}(D_s^{*+}\to D_s^+(\phi\pi^+)\gamma)}$	0.063 ± 0. 0026	0.0631 ± 0.0015
$\frac{\mathcal{B}(D_s^{*+}\to D_s^+(\bar{K}^{*0}K^+)\pi^0)}{\mathcal{B}(D_s^{*+}\to D_s^+(\bar{K}^{*0}K^+)\gamma)}$	0.064 ± 0.0025	0.0634 ± 0.0022

Table 4.12: Ratio of branching fractions corresponding to both decay modes of D_s^+ for data and MC events.

Further, the results from two decay modes of D_s^+: $D_s^+ \to \phi\pi^+$ and $D_s^+ \to$

$\bar{K}^{*0}K^+$ are combined using weighted average method of combining branching fractions. The combined result provides a more precise estimate of the branching fraction than from the single decay mode. The uncertainties associated with each measurement are also taken into account in the combined result to provide a complete assessment of the branching fraction and its uncertainty.

In the weighted average method, each measurement of the branching ratio from different decay channels is assigned a weight based on its statistical uncertainty. These weights reflect the relative reliability and precision of each measurement. The weighted average is calculated by summing the products of the branching ratio and its corresponding weight for all measurements and dividing by the sum of the weights.

Let's BR_i denote the branching fractions from different decay modes where $i = 1, 2, 3, ..., N$ represents each decay mode. Similarly, σ_i represents the total uncertainty associated with each branching ratio BR_i.

The weight assigned to each measurement BR_i can be calculated using its uncertainty as:

$$w_i = \frac{1}{\sigma_i^2}$$

Then, the weighted average branching fraction $\bar{BR}$ is calculated as follows:

$$\bar{BR} = \frac{\sum_{i=1}^{N} w_i \cdot BR_i}{\sum_{i=1}^{N} w_i}$$

This formula essentially calculates the weighted average by taking the sum of the products of each branching ratio and its corresponding weight and dividing by the sum of the weights.

The uncertainty associated with the weighted average $\bar{BR}$ can be calculated using the standard error of the mean, given by:

$$\sigma_{\bar{BR}} = \sqrt{\frac{1}{\sum_{i=1}^{N} w_i}}$$

This formula accounts for the uncertainties of individual measurements and their weights in determining the overall uncertainty of the weighted average. This approach ensures that measurements with smaller uncertainties contribute more to the final result while taking into account the overall precision and reliability of each measurement.

0.0634 ± 0.0018 and 0.0632 ± 0.0013 are the final ratios of the branching fractions calculated with weighted average method for data and MC, respectively.

To compile the systematic uncertainties from both decay modes of D_s^+, the weighted average method is used similarly as used to compile the branching ratios. Combined systematics calculated from the weighted average method from both decay modes of D_s^+ is 3%.

The branching fraction $\mathcal{B}(D_s^{*+} \to D_s^+\pi^0)$ with respect to $\mathcal{B}(D_s^{*+} \to D_s^+\gamma)$ using the data corresponding to 424 fb^{-1} luminosity collected by Belle II detector during e^+e^- collisions at or near $\Upsilon(4S)$ resonance is measured. The results is :

$$\frac{\mathcal{B}(D_s^{*+} \to D_s^+\pi^0)}{\mathcal{B}(D_s^{*+} \to D_s^+\gamma)} = 0.0634 \pm 0.0018 \pm 0.0019$$

where the first uncertainty is the statistical and the second one is systematical uncertainty. The results from the data are consistent with simulations and with the previous measurements. A significant 50% reduction in the statistical uncertainty is achieved and a 40% decrease in the overall uncertainty compared to the previous best measurements. Figure 4.29 compares the $\mathcal{B}(D_s^{*+} \to D_s^+\pi^0)/\mathcal{B}(D_s^{*+} \to D_s^+\gamma)$ measured by different experiments with Belle II results.

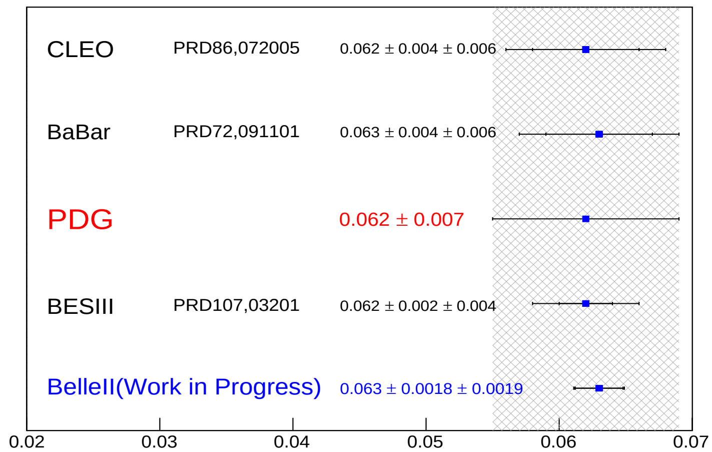

Figure 4.29: Comparison of $\mathcal{B}(D_s^{*+} \to D_s^+\pi^0)/\mathcal{B}(D_s^{*+} \to D_s^+\gamma)$ measured by different experiments with Belle II results.

Bibliography

[1] Y. Kubota et al. (CLEO Collaboration), "The CLEO II detector," *Nuclear Instruments and Methods in Physics Research Section A: Accelerators, Spectrometers, Detectors and Associated Equipment*, vol. 320, no. 1, pp. 66–113, 1992.

[2] B. Aubert et al. (BaBar Collaboration), "The BaBar detector," *Nuclear Instruments and Methods in Physics Research A: Accelerators, Spectrometers, Detectors and Associated Equipment*, vol. 479, pp. 1–116, 2002.

[3] M. Ablikim et al. (BESIII Collaboration), "Design and construction of the BESIII detector," *Nuclear Instruments and Methods in Physics Research A: Accelerators, Spectrometers, Detectors and Associated Equipment*, vol. 614, no. 3, pp. 345–399, 2010.

[4] J. Gronberg et al. (CLEO Collaboration), "Observation of the isospin-violating decay $D_s^{*+} \to {D_s}^+\pi^0$," *Physical Review Letters*, vol. 75, pp. 3232–3236, 1995.

[5] B. Aubert et al. (BABAR Collaboration), "Measurement of the branching ratios $\Gamma(D_s^{*+} \to D_s^+\pi^0)/\Gamma(D_s^{*+} \to D_s^+\gamma)$ and $\Gamma(D^{*0} \to D^0\pi^0)/\Gamma(D^{*0} \to D^0\gamma)$," *Physical Review D*, vol. 72, p. 091101, 2005.

[6] M. Ablikim et al. (BESIII Collaboration), "Measurement of branching fraction of $D_s^{*+} \to D_s^+\pi^0$ relative to $D_s^{*+} \to D_s^+\gamma$," *Physical Review D*, vol. 107, p. 032011, 2023.

[7] R. L. Workman et al. (Particle Data Group), "Review of Particle Physics," *Progress of Theoretical and Experimental Physics*, vol. 2022, p. 083C01, 2022.

[8] T. B. I. Collaboration, "Measurement of the integrated luminosity of data samples collected during 2019-2022 by the Belle II experiment," 2024. `https://arxiv.org/abs/2407.00965`.

[9] Sato, Yo, Cunliffe, Sam, Meier, Frank, and Zupanc, Anze, “Monte Carlo matching in the Belle II software,” *EPJ Web Conf.*, vol. 251, p. 03021, 2021.

[10] T. Ferber and P. Urquijo, “Overview of the Belle II Physics Generators,” Jun 2015. `https://docs.belle2.org/record/282?ln=en`.

[11] D. Lange, “The EvtGen particle decay simulation package,” *Nuclear Instruments and Methods in Physics Research Section A: Accelerators, Spectrometers, Detectors and Associated Equipment*, vol. 462, pp. 152 – 155, 2001.

[12] S. Jadach et al., “Multi-photon Monte Carlo event generator KKMCee for lepton and quark pair production in lepton colliders,” *Computer Physics Communications*, vol. 283, p. 108556, Feb. 2023.

[13] S. Agostinelli *et al.*, “GEANT4: A Simulation toolkit,” *Nuclear Instruments and Methods in Physics Research Section A: Accelerators, Spectrometers, Detectors and Associated Equipment*, vol. 506, pp. 250 – 303, Jan. 2003.

[14] S. Prabha Maharana, V. Vimal Sukhida, and S. Sandilya, “Charged Particle Identification Performances in Belle II,” *Springer Proc. Phys.*, vol. 304, pp. 166–169, 2024.

[15] H. Ikeda et al. (Belle Collaboration), “A detailed test of the CsI(Tl) calorimeter for BELLE with photon beams of energy between 20 MeV and 5.4 GeV,” *Nuclear Instruments and Methods in Physics Research Section A: Accelerators, Spectrometers, Detectors and Associated Equipment*, vol. 441, no. 3, pp. 401–426, 2000.

[16] Belle II Collaboration, “Belle II Software Documentation,” `https://software.belle2.org/development/sphinx/index.html`.

[17] J. F. Krohn et al., “Global decay chain vertex fitting at Belle II,” *Nuclear Instruments and Methods in Physics Research Section A: Accelerators, Spectrometers, Detectors and Associated Equipment*, vol. 976, p. 164269, 2020.

[18] R. Fruhwirth, "Application of Kalman filtering to track and vertex fitting," *Nuclear Instruments and Methods in Physics Research Section A: Accelerators, Spectrometers, Detectors and Associated Equipment*, vol. 262, pp. 444–450, 1987.

[19] N. L. Johnson, "Systems of frequency curves generated by methods of translation," *Biometrika*, vol. 36, pp. 149–176, 1949.

[20] A. Selce, T. Koga, and S. Stengel, "Optimization of pi0 reconstruction selection and first systematic uncertainty evaluation of the efficiencies," 2020.

Chapter 5

Summary and Conclusion

This thesis is based on the study of the decays of charm meson using the Belle II experiment. The study of charm meson decays is crucial for advancing our understanding of the fundamental forces and particles in the universe by testing the limits of current theories and exploring potential physics beyond the Standard Model. Since the prediction of the charm quark's existence, the study of the charm mesons plays an important role in the flavor physics. The charm meson decays help to probe the validity and limitations of the Standard Model, especially in understanding weak interactions and CP violation. Investigating CP violation in charm decays can provide insights to the matter dominated universe. The discovery of the charm quark with the J/ψ meson confirmed the existence of the fourth quark predicted by the GIM mechanism [1] that explains the suppression of Flavor Changing Neutral Currents (FCNC). Precise measurements of the charm quark processes, such as neutral charm meson mixing, CP violations, FCNCs and lepton flavor violation, can potentially uncover new physics phenomena. Experiments like Belle II [2], BaBar [3] and LHCb [4] have made a significant contribution in exploring the D meson decays.

The Belle II experiment located at the SuperKEKB accelerator [5] is the next-generation B-Factory and has a significant improvement over the Belle [6] and the

BaBar experiments [3]. Over the coming decades, the Belle II experiment will collect billions of bottom mesons, charm mesons and τ leptons generated by electron-positron collisions at the SuperKEKB accelerator. This vast dataset collected under controlled and low-background conditions offers an opportunity to measure hundreds of parameters that validate the Standard Model and explore the potential existence of new particles. Clean background environment, higher trigger efficiency, excellent reconstruction of gamma and π^0 particles, efficient flavor-tagging and access to numerous control samples for systematic studies are some advantages of studying charm physics at the Belle II experiment over the hadron experiments like LHCb.

The work presented in this thesis focuses on the measurement of the branching fraction $\mathcal{B}(D_s^{*+} \to D_s^+\pi^0)$ with respect to $\mathcal{B}(D_s^{*+} \to D_s^+\gamma)$. These precise measurements hold significant importance in understanding the dynamics of strong interaction processes involving charm quarks within the Quantum Chromodynamics (QCD) [7]. It can also provide crucial input for theoretical models that allows a deeper understanding of particle interactions, serving as a testbed for predictions within the Standard Model of particle physics. Any deviations from the expected branching fraction could indicate a presence of new physics beyond the Standard Model. By comparing experimental measurements with theoretical predictions, these theoretical models can be improved. Moreover, the precise and early measurements obtained from the Belle II data also serve as valuable benchmarks for evaluating the performance of the Belle II detector.

This measurement is based on the analysis of e^+e^- collision data collected with Belle II detector. The analyzed data corresponds to an integrated luminosity of 424 fb^{-1}. An optimized criteria is devised to efficiently identify and reconstruct decay modes $D_s^{*+} \to D_s^+\pi^0$ and $D_s^{*+} \to D_s^+\gamma$. Here the D_s^+ candidate is considered to decay into $\phi\pi^+$ and $\bar{K}^{*0}K^+$. The signal yield is extracted by performing a two-dimensional extended maximum likelihood fit of invariant mass of D_s^+, $M(D_s^+)$, and the mass difference of D_s^{*+} and D_s^+, ΔM, distributions. The fitting procedure uses Probability Density Functions (PDFs) for each decay mode. Different PDFs are applied to model the signal and various background components such as combinatorial background and fake π^0 and γ backgrounds. Signal selection efficiencies are calculated by using the control sample of η decay modes. Various sources of systematic uncertainties are investigated. Here dominant uncertainties arise from the efficiency corrections for γ and π^0 reconstruction, dependence of branching fraction on the center of mass momentum of D_s^{*+} candidates and fitting model assumptions. The measured value of the ratio is:

$$\frac{\mathcal{B}(D_s^{*+} \to D_s^+ \pi^0)}{\mathcal{B}(D_s^{*+} \to D_s^+ \gamma)} = 0.0634 \pm 0.0018 \pm 0.0019,$$

where the first uncertainty is the statistical and the second one is systematic uncertainty. A significant 50% reduction in statistical uncertainty and a 40% decrease in overall uncertainty is achieved compared to the previous best measurements. This analysis offers the most precise result to date. The measured branching fraction ratio is consistent with the predictions from the Standard Model as well as with the previous measurements by other experiments like CLEO [8], BaBar [9] and BESIII [10]. This consistency shows the robustness in the fitting methodology and reliability of the Belle II detector's performance in conducting precision measurements in charm physics. The predictions by the covariant model (0.079 ± 0.008) [11] overestimate the measured values and, therefore, require further refinement.

These precise measurements are crucial for understanding QCD within the Standard Model. These measurements provide valuable constraints on low-energy phenomenological models and are essential inputs for determining key parameters such as the D_s^+ decay constant, $f_{D_s^+}$, and the $c \to s$ CKM matrix element, $|V_{cs}|$. Therefore, this study can provide a significant role in refining our understanding of these fundamental processes.

Bibliography

[1] S. L. Glashow, J. Iliopoulos, and L. Maiani, "Weak interactions with lepton-hadron symmetry," *Physical Review D*, vol. 2, pp. 1285–1292, Oct 1970.

[2] T. Abe et al. (Belle II Collaboration), *"Belle II Technical Design Report"*. KEK-REPORT-2010-1, 2010.

[3] B. Aubert et al. (BaBar Collaboration), "The BaBar detector," *Nuclear Instruments and Methods in Physics Research A: Accelerators, Spectrometers, Detectors and Associated Equipment*, vol. 479, pp. 1–116, 2002.

[4] P. Perret, "Status and expected performance of the LHCb experiment," *Nuclear Physics B - Proceedings Supplements*, vol. 142, pp. 442–447, 2005.

[5] K. Akai et al. (SuperKEKB Collaboration), "SuperKEKB collider," *Nuclear Instruments and Methods in Physics Research Section A: Accelerators, Spectrometers, Detectors and Associated Equipment*, vol. 907, pp. 188–199, Nov. 2018.

[6] A. Abashian et al. (Belle Collaboration), "The Belle Detector," *Nuclear Instruments and Methods in Physics Research Section A: Accelerators, Spectrometers, Detectors and Associated Equipment*, vol. 479, pp. 117–232, 2002.

[7] W. Marciano and H. Pagels, "Quantum chromodynamics," *Physics Reports*, vol. 36, pp. 137–276, 1978.

[8] J. Gronberg et al. (CLEO Collaboration), "Observation of the isospin-violating decay $D_s^{*+} \to {D_s}^+\pi^0$," *Physical Review Letters*, vol. 75, pp. 3232–3236, 1995.

[9] B. Aubert et al. (BABAR Collaboration), "Measurement of the branching ratios $\Gamma(D_s^{*+} \to D_s^+\pi^0)/\Gamma(D_s^{*+} \to D_s^+\gamma)$ and $\Gamma(D^{*0} \to D^0\pi^0)/\Gamma(D^{*0} \to D^0\gamma)$," *Physical Review D*, vol. 72, p. 091101, 2005.

[10] M. Ablikim et al. (BESIII Collaboration), "Measurement of branching fraction of $D_s^{*+} \to D_s^+\pi^0$ relative to $D_s^{*+} \to D_s^+\gamma$," *Physical Review D*, vol. 107, p. 032011, 2023.

[11] C.-Y. Cheung and C.-W. Hwang, "Three symmetry breakings in strong and radiative decays of strange heavy mesons," *Eur. Phys. J. C*, vol. 76, p. 19, Jan. 2016.

Societal Impact

Studying charm physics with the Belle II detector plays a unique role in society from advancing fundamental scientific knowledge to encouraging global collaboration. Charm meson decays help to understand the fundamental structure of the universe. The Standard Model explains the basic building blocks of the universe and the fundamental particles. These decays help to increase our knowledge regarding the universe by allowing us to study physics not explained by the Standard Model such as dark matter, dark energy, nature of gravity, matter-antimatter asymmetry, etc. Understanding particle behavior and forces could lead to new energy sources, advanced materials, or technologies that could dramatically change society. In addition to our theoretical understanding, experiments like Belle II have a great impact on society. This thesis involves the statistical analysis of large datasets, which play a fundamental role in the development and application of machine learning techniques. Various statistical methods used for the analysis such as classifying data, making predictions and recognizing patterns are basics of machine learning algorithms. In this way, there is a close connection between experimental high energy physics and advancements in artificial intelligence and data science. Technological advancements such as data analysis and machine learning, developed for the experimental high energy physics detectors can be applied to various fields like medical imaging, cybersecurity and big data analytics. A key example of this is the development of the Positron Emission Tomography (PET) scans which is a critical tool in modern medicine. Particle accelerators such as cyclotrons are used to produce the radioisotopes required for PET scans that provide high resolution imaging of internal body structures and are essential for detecting cancer. This technology was initially developed for high energy physics research and became a foundation of non-invasive medical diagnostics. Beyond these technological advancements, the Belle II experiment has played a major role in educating and training scientists and engineers. These individuals develop expertise in fields such as physics, computer science and engineering. Skills such as problem-solving, data analysis and programming acquired during working on particle physics experiments can also be used in other sectors and have a significant contribution to academia, industry, and public service. Working on experiments like Belle II can also promote the global scientific collaboration. Researchers from all over the world contribute to the success of the experiment. These relationships extend beyond the realm of physics by promoting shared knowledge and technologies that can be applied to societal challenges such as climate change, renewable energy and public health. Studying charm physics using Belle II detector has many benefits for society as a whole. The tools and technologies developed through this research help to address many questions that are not explained by current models.

Precise Measurement of the D^0 and D^+ Lifetimes at Belle II

F. Abudinén,[31] I. Adachi,[21,18] K. Adamczyk,[66] L. Aggarwal,[73] H. Ahmed,[76] H. Aihara,[112] N. Akopov,[2] A. Aloisio,[88,25] N. Anh Ky,[40,13] D. M. Asner,[3] H. Atmacan,[99] V. Aushev,[81] V. Babu,[11] S. Bacher,[66] H. Bae,[112] S. Baehr,[46] S. Bahinipati,[33] P. Bambade,[95] Sw. Banerjee,[103] S. Bansal,[73] M. Barrett,[21] J. Baudot,[96] M. Bauer,[46] A. Baur,[11] J. Becker,[46] P. K. Behera,[35] J. V. Bennett,[106] E. Bernieri,[29] F. U. Bernlochner,[97] M. Bertemes,[38] E. Bertholet,[84] M. Bessner,[101] S. Bettarini,[91,28] V. Bhardwaj,[32] F. Bianchi,[93,30] T. Bilka,[7] S. Bilokin,[54] D. Biswas,[103] A. Bobrov,[4,68] D. Bodrov,[64,52] A. Bolz,[11] A. Bozek,[66] M. Bračko,[104,80] P. Branchini,[29] N. Braun,[46] R. A. Briere,[5] T. E. Browder,[101] A. Budano,[29] S. Bussino,[92,29] M. Campajola,[88,25] L. Cao,[11] G. Casarosa,[91,28] C. Cecchi,[90,27] D. Červenkov,[7] M.-C. Chang,[15] P. Chang,[65] R. Cheaib,[11] V. Chekelian,[57] C. Chen,[42] Y.-T. Chen,[65] B. G. Cheon,[20] K. Chilikin,[52] K. Chirapatpimol,[8] H.-E. Cho,[20] K. Cho,[48] S.-J. Cho,[118] S.-K. Choi,[19] S. Choudhury,[34] D. Cinabro,[116] L. Corona,[91,28] L. M. Cremaldi,[106] S. Cunliffe,[11] T. Czank,[113] F. Dattola,[11] E. De La Cruz-Burelo,[6] G. de Marino,[95] G. De Nardo,[88,25] G. De Pietro,[29] R. de Sangro,[24] M. Destefanis,[93,30] S. Dey,[84] A. De Yta-Hernandez,[6] A. Di Canto,[3] F. Di Capua,[88,25] J. Dingfelder,[97] Z. Doležal,[7] I. Domínguez Jiménez,[87] T. V. Dong,[13] M. Dorigo,[31] K. Dort,[45] D. Dossett,[105] S. Dubey,[101] S. Duell,[97] G. Dujany,[96] P. Ecker,[46] D. Epifanov,[4,68] T. Ferber,[11] D. Ferlewicz,[105] G. Finocchiaro,[24] K. Flood,[101] A. Fodor,[58] F. Forti,[91,28] B. G. Fulsom,[72] A. Gabrielli,[94,31] N. Gabyshev,[4,68] A. Gaz,[89,26] A. Gellrich,[11] G. Giakoustidis,[97] R. Giordano,[88,25] A. Giri,[34] A. Glazov,[11] B. Gobbo,[31] R. Godang,[110] P. Goldenzweig,[46] B. Golob,[102,80] W. Gradl,[44] E. Graziani,[29] D. Greenwald,[83] T. Gu,[108] Y. Guan,[99] K. Gudkova,[4,68] J. Guilliams,[106] C. Hadjivasiliou,[72] S. Halder,[82] K. Hara,[21,18] T. Hara,[21,18] O. Hartbrich,[101] K. Hayasaka,[67] H. Hayashii,[63] S. Hazra,[82] C. Hearty,[98,39] I. Heredia de la Cruz,[6,10] M. Hernández Villanueva,[11] A. Hershenhorn,[98] T. Higuchi,[113] E. C. Hill,[98] H. Hirata,[60] M. Hoek,[44] M. Hohmann,[105] C.-L. Hsu,[111] T. Humair,[57] T. Iijima,[60,62] K. Inami,[60] G. Inguglia,[38] A. Ishikawa,[21,18] R. Itoh,[21,18] M. Iwasaki,[70] Y. Iwasaki,[21] W. W. Jacobs,[36] D. E. Jaffe,[3] E.-J. Jang,[19] S. Jia,[16] Y. Jin,[31] H. Junkerkalefeld,[97] H. Kakuno,[86] A. B. Kaliyar,[82] J. Kandra,[7] K. H. Kang,[51] R. Karl,[11] G. Karyan,[2] Y. Kato,[60,62] T. Kawasaki,[47] C. Kiesling,[57] C.-H. Kim,[20] D. Y. Kim,[79] Y.-K. Kim,[118] Y. Kim,[49] T. D. Kimmel,[115] K. Kinoshita,[99] P. Kodyš,[7] T. Koga,[21] S. Kohani,[101] T. Konno,[47] S. Korpar,[104,80] E. Kovalenko,[4,68] R. Kowalewski,[114] T. M. G. Kraetzschmar,[57] F. Krinner,[57] P. Križan,[102,80] P. Krokovny,[4,68] T. Kuhr,[54] J. Kumar,[5] M. Kumar,[56] R. Kumar,[74] K. Kumara,[116] S. Kurz,[11] A. Kuzmin,[4,68] Y.-J. Kwon,[118] S. Lacaprara,[26] K. Lalwani,[56] T. Lam,[115] L. Lanceri,[31] J. S. Lange,[45] M. Laurenza,[92,29] K. Lautenbach,[1] F. R. Le Diberder,[95] S. C. Lee,[51] P. Leitl,[57] D. Levit,[83] C. Li,[53] L. K. Li,[99] J. Libby,[35] K. Lieret,[54] Z. Liptak,[23] Q. Y. Liu,[11] D. Liventsev,[116,21] S. Longo,[11] T. Lueck,[54] C. Lyu,[97] R. Manfredi,[94,31] E. Manoni,[27] C. Marinas,[41] A. Martini,[11] T. Matsuda,[107] K. Matsuoka,[21] D. Matvienko,[4,52,68] J. A. McKenna,[98] F. Meier,[12] M. Merola,[88,25] F. Metzner,[46] C. Miller,[114] K. Miyabayashi,[63] R. Mizuk,[52,64] G. B. Mohanty,[82] N. Molina-Gonzalez,[6] H. Moon,[49] H.-G. Moser,[57] M. Mrvar,[38] C. Murphy,[113] R. Mussa,[30] I. Nakamura,[21,18] K. R. Nakamura,[21,18] M. Nakao,[21,18] H. Nakazawa,[65] Z. Natkaniec,[66] A. Natochii,[101] G. Nazaryan,[2] C. Niebuhr,[11] M. Niiyama,[50] N. K. Nisar,[3] S. Nishida,[21,18] K. Nishimura,[101] S. Ogawa,[85] Y. Onishchuk,[81] H. Ono,[67] Y. Onuki,[112] P. Oskin,[52] E. R. Oxford,[5] H. Ozaki,[21,18] P. Pakhlov,[52,59] A. Paladino,[91,28] T. Pang,[108] A. Panta,[106] E. Paoloni,[91,28] S. Pardi,[25] H. Park,[51] S.-H. Park,[21] B. Paschen,[97] A. Passeri,[29] A. Pathak,[103] S. Patra,[32] S. Paul,[83] T. K. Pedlar,[55] I. Peruzzi,[24] R. Peschke,[101] R. Pestotnik,[80] F. Pham,[105] M. Piccolo,[24] L. E. Piilonen,[115] G. Pinna Angioni,[93,30] P. L. M. Podesta-Lerma,[87] T. Podobnik,[80] S. Pokharel,[106] G. Polat,[1] V. Popov,[64] C. Praz,[11] S. Prell,[42] E. Prencipe,[45] M. T. Prim,[97] M. V. Purohit,[69] H. Purwar,[101] N. Rad,[11] P. Rados,[38] S. Raiz,[94,31] S. Reiter,[45] M. Remnev,[4,68] I. Ripp-Baudot,[96] G. Rizzo,[91,28] L. B. Rizzuto,[80] S. H. Robertson,[58,39] J. M. Roney,[114,39] A. Rostomyan,[11] N. Rout,[35] M. Rozanska,[66] D. Sahoo,[42] D. A. Sanders,[106] S. Sandilya,[34] A. Sangal,[99] L. Santelj,[102,80] Y. Sato,[21] V. Savinov,[108] B. Scavino,[44] J. Schueler,[101] C. Schwanda,[38] A. J. Schwartz,[99] Y. Seino,[67] A. Selce,[29,14] K. Senyo,[117] J. Serrano,[1] C. Sfienti,[44] J.-G. Shiu,[65] B. Shwartz,[4,68] A. Sibidanov,[101] F. Simon,[57] R. J. Sobie,[114,39] A. Soffer,[84] A. Sokolov,[37] E. Solovieva,[52] S. Spataro,[93,30] B. Spruck,[44] M. Starič,[80] S. Stefkova,[11] Z. S. Stottler,[115] R. Stroili,[89,26] J. Strube,[72] M. Sumihama,[17,71] W. Sutcliffe,[97] S. Y. Suzuki,[21,18] H. Svidras,[11] M. Tabata,[9] M. Takizawa,[75,22,77] U. Tamponi,[30] S. Tanaka,[21,18] K. Tanida,[43] H. Tanigawa,[112] N. Taniguchi,[21] F. Tenchini,[91,28] R. Tiwary,[82] D. Tonelli,[31] E. Torassa,[26] N. Toutounji,[111] K. Trabelsi,[95] T. Tsuboyama,[21,18] I. Ueda,[21,18] S. Uehara,[21,18] Y. Uematsu,[112] T. Uglov,[52,64] K. Unger,[46] Y. Unno,[20] K. Uno,[67] S. Uno,[21,18] P. Urquijo,[105] Y. Ushiroda,[21,18,112] Y. V. Usov,[4,68] S. E. Vahsen,[101] R. van Tonder,[97] G. S. Varner,[101] A. Vinokurova,[4,68] L. Vitale,[94,31] A. Vossen,[12] E. Waheed,[21] H. M. Wakeling,[58] E. Wang,[108] M.-Z. Wang,[65] X. L. Wang,[16] A. Warburton,[58] M. Watanabe,[67] M. Welsch,[97] C. Wessel,[97] J. Wiechczynski,[66] E. Won,[49] X. P. Xu,[78] B. D. Yabsley,[111] S. Yamada,[21] W. Yan,[109] S. B. Yang,[49] H. Ye,[11] J. Yelton,[100] J. H. Yin,[49] K. Yoshihara,[60] Y. Yusa,[67] L. Zani,[1] V. Zhilich,[4,68] Q. D. Zhou,[60,61,62] X. Y. Zhou,[53] V. I. Zhukova,[52] and R. Žlebčík[7]

(Belle II Collaboration)

[1]Aix Marseille Université, CNRS/IN2P3, CPPM, 13288 Marseille, France
[2]Alikhanyan National Science Laboratory, Yerevan 0036, Armenia
[3]Brookhaven National Laboratory, Upton, New York 11973, USA
[4]Budker Institute of Nuclear Physics SB RAS, Novosibirsk 630090, Russian Federation
[5]Carnegie Mellon University, Pittsburgh, Pennsylvania 15213, USA
[6]Centro de Investigacion y de Estudios Avanzados del Instituto Politecnico Nacional, Mexico City 07360, Mexico
[7]Faculty of Mathematics and Physics, Charles University, 121 16 Prague, Czech Republic
[8]Chiang Mai University, Chiang Mai 50202, Thailand
[9]Chiba University, Chiba 263-8522, Japan
[10]Consejo Nacional de Ciencia y Tecnología, Mexico City 03940, Mexico
[11]Deutsches Elektronen-Synchrotron, 22607 Hamburg, Germany
[12]Duke University, Durham, North Carolina 27708, USA
[13]Institute of Theoretical and Applied Research (ITAR), Duy Tan University, Hanoi 100000, Vietnam
[14]ENEA Casaccia, I-00123 Roma, Italy
[15]Department of Physics, Fu Jen Catholic University, Taipei 24205, Taiwan
[16]Key Laboratory of Nuclear Physics and Ion-beam Application (MOE) and Institute of Modern Physics, Fudan University, Shanghai 200443, China
[17]Gifu University, Gifu 501-1193, Japan
[18]The Graduate University for Advanced Studies (SOKENDAI), Hayama 240-0193, Japan
[19]Gyeongsang National University, Jinju 52828, South Korea
[20]Department of Physics and Institute of Natural Sciences, Hanyang University, Seoul 04763, South Korea
[21]High Energy Accelerator Research Organization (KEK), Tsukuba 305-0801, Japan
[22]J-PARC Branch, KEK Theory Center, High Energy Accelerator Research Organization (KEK), Tsukuba 305-0801, Japan
[23]Hiroshima University, Higashi-Hiroshima, Hiroshima 739-8530, Japan
[24]INFN Laboratori Nazionali di Frascati, I-00044 Frascati, Italy
[25]INFN Sezione di Napoli, I-80126 Napoli, Italy
[26]INFN Sezione di Padova, I-35131 Padova, Italy
[27]INFN Sezione di Perugia, I-06123 Perugia, Italy
[28]INFN Sezione di Pisa, I-56127 Pisa, Italy
[29]INFN Sezione di Roma Tre, I-00146 Roma, Italy
[30]INFN Sezione di Torino, I-10125 Torino, Italy
[31]INFN Sezione di Trieste, I-34127 Trieste, Italy
[32]Indian Institute of Science Education and Research Mohali, SAS Nagar, 140306, India
[33]Indian Institute of Technology Bhubaneswar, Satya Nagar 751007, India
[34]Indian Institute of Technology Hyderabad, Telangana 502285, India
[35]Indian Institute of Technology Madras, Chennai 600036, India
[36]Indiana University, Bloomington, Indiana 47408, USA
[37]Institute for High Energy Physics, Protvino 142281, Russian Federation
[38]Institute of High Energy Physics, Vienna 1050, Austria
[39]Institute of Particle Physics (Canada), Victoria, British Columbia V8W 2Y2, Canada
[40]Institute of Physics, Vietnam Academy of Science and Technology (VAST), Hanoi, Vietnam
[41]Instituto de Fisica Corpuscular, Paterna 46980, Spain
[42]Iowa State University, Ames, Iowa 50011, USA
[43]Advanced Science Research Center, Japan Atomic Energy Agency, Naka 319-1195, Japan
[44]Institut für Kernphysik, Johannes Gutenberg-Universität Mainz, D-55099 Mainz, Germany
[45]Justus-Liebig-Universität Gießen, 35392 Gießen, Germany
[46]Institut für Experimentelle Teilchenphysik, Karlsruher Institut für Technologie, 76131 Karlsruhe, Germany
[47]Kitasato University, Sagamihara 252-0373, Japan
[48]Korea Institute of Science and Technology Information, Daejeon 34141, South Korea
[49]Korea University, Seoul 02841, South Korea
[50]Kyoto Sangyo University, Kyoto 603-8555, Japan
[51]Kyungpook National University, Daegu 41566, South Korea
[52]P.N. Lebedev Physical Institute of the Russian Academy of Sciences, Moscow 119991, Russian Federation
[53]Liaoning Normal University, Dalian 116029, China
[54]Ludwig Maximilians University, 80539 Munich, Germany
[55]Luther College, Decorah, Iowa 52101, USA
[56]Malaviya National Institute of Technology Jaipur, Jaipur 302017, India

[57]Max-Planck-Institut für Physik, 80805 München, Germany
[58]McGill University, Montréal, Québec, H3A 2T8, Canada
[59]Moscow Physical Engineering Institute, Moscow 115409, Russian Federation
[60]Graduate School of Science, Nagoya University, Nagoya 464-8602, Japan
[61]Institute for Advanced Research, Nagoya University, Nagoya 464-8602, Japan
[62]Kobayashi-Maskawa Institute, Nagoya University, Nagoya 464-8602, Japan
[63]Nara Women's University, Nara 630-8506, Japan
[64]National Research University Higher School of Economics, Moscow 101000, Russian Federation
[65]Department of Physics, National Taiwan University, Taipei 10617, Taiwan
[66]H. Niewodniczanski Institute of Nuclear Physics, Krakow 31-342, Poland
[67]Niigata University, Niigata 950-2181, Japan
[68]Novosibirsk State University, Novosibirsk 630090, Russian Federation
[69]Okinawa Institute of Science and Technology, Okinawa 904-0495, Japan
[70]Osaka City University, Osaka 558-8585, Japan
[71]Research Center for Nuclear Physics, Osaka University, Osaka 567-0047, Japan
[72]Pacific Northwest National Laboratory, Richland, Washington, D.C. 99352, USA
[73]Panjab University, Chandigarh 160014, India
[74]Punjab Agricultural University, Ludhiana 141004, India
[75]Meson Science Laboratory, Cluster for Pioneering Research, RIKEN, Saitama 351-0198, Japan
[76]St. Francis Xavier University, Antigonish, Nova Scotia, B2G 2W5, Canada
[77]Showa Pharmaceutical University, Tokyo 194-8543, Japan
[78]Soochow University, Suzhou 215006, China
[79]Soongsil University, Seoul 06978, South Korea
[80]J. Stefan Institute, 1000 Ljubljana, Slovenia
[81]Taras Shevchenko National Univ. of Kiev, Kiev, Ukraine
[82]Tata Institute of Fundamental Research, Mumbai 400005, India
[83]Department of Physics, Technische Universität München, 85748 Garching, Germany
[84]Tel Aviv University, School of Physics and Astronomy, Tel Aviv, 69978, Israel
[85]Toho University, Funabashi 274-8510, Japan
[86]Tokyo Metropolitan University, Tokyo 192-0397, Japan
[87]Universidad Autonoma de Sinaloa, Sinaloa 80000, Mexico
[88]Dipartimento di Scienze Fisiche, Università di Napoli Federico II, I-80126 Napoli, Italy
[89]Dipartimento di Fisica e Astronomia, Università di Padova, I-35131 Padova, Italy
[90]Dipartimento di Fisica, Università di Perugia, I-06123 Perugia, Italy
[91]Dipartimento di Fisica, Università di Pisa, I-56127 Pisa, Italy
[92]Dipartimento di Matematica e Fisica, Università di Roma Tre, I-00146 Roma, Italy
[93]Dipartimento di Fisica, Università di Torino, I-10125 Torino, Italy
[94]Dipartimento di Fisica, Università di Trieste, I-34127 Trieste, Italy
[95]Université Paris-Saclay, CNRS/IN2P3, IJCLab, 91405 Orsay, France
[96]Université de Strasbourg, CNRS, IPHC, UMR 7178, 67037 Strasbourg, France
[97]University of Bonn, 53115 Bonn, Germany
[98]University of British Columbia, Vancouver, British Columbia, V6T 1Z1, Canada
[99]University of Cincinnati, Cincinnati, Ohio 45221, USA
[100]University of Florida, Gainesville, Florida 32611, USA
[101]University of Hawaii, Honolulu, Hawaii 96822, USA
[102]Faculty of Mathematics and Physics, University of Ljubljana, 1000 Ljubljana, Slovenia
[103]University of Louisville, Louisville, Kentucky 40292, USA
[104]Faculty of Chemistry and Chemical Engineering, University of Maribor, 2000 Maribor, Slovenia
[105]School of Physics, University of Melbourne, Victoria 3010, Australia
[106]University of Mississippi, University, Mississippi 38677, USA
[107]University of Miyazaki, Miyazaki 889-2192, Japan
[108]University of Pittsburgh, Pittsburgh, Pennsylvania 15260, USA
[109]University of Science and Technology of China, Hefei 230026, China
[110]University of South Alabama, Mobile, Alabama 36688, USA
[111]School of Physics, University of Sydney, New South Wales 2006, Australia
[112]Department of Physics, University of Tokyo, Tokyo 113-0033, Japan
[113]Kavli Institute for the Physics and Mathematics of the Universe (WPI), University of Tokyo, Kashiwa 277-8583, Japan
[114]University of Victoria, Victoria, British Columbia, V8W 3P6, Canada
[115]Virginia Polytechnic Institute and State University, Blacksburg, Virginia 24061, USA
[116]Wayne State University, Detroit, Michigan 48202, USA

[117]*Yamagata University, Yamagata 990-8560, Japan*
[118]*Yonsei University, Seoul 03722, South Korea*

(Received 6 August 2021; accepted 20 October 2021; published 19 November 2021)

We report a measurement of the D^0 and D^+ lifetimes using $D^0 \to K^-\pi^+$ and $D^+ \to K^-\pi^+\pi^+$ decays reconstructed in $e^+e^- \to c\bar{c}$ data recorded by the Belle II experiment at the SuperKEKB asymmetric-energy e^+e^- collider. The data, collected at center-of-mass energies at or near the $\Upsilon(4S)$ resonance, correspond to an integrated luminosity of 72 fb^{-1}. The results, $\tau(D^0) = 410.5 \pm 1.1(\mathrm{stat}) \pm 0.8(\mathrm{syst})$ fs and $\tau(D^+) = 1030.4 \pm 4.7(\mathrm{stat}) \pm 3.1(\mathrm{syst})$ fs, are the most precise to date and are consistent with previous determinations.

DOI: 10.1103/PhysRevLett.127.211801

Accurate predictions of lifetimes of weakly decaying charmed and bottom hadrons are challenging because they involve strong-interaction theory at low energy. Predictions must resort to effective models, such as the heavy-quark expansion [1–6], which also underpin strong-interaction calculations required for the determination of fundamental standard-model parameters from hadron-decay measurements (e.g., to extract the strength of quark-mixing couplings from decay widths). Precise lifetime measurements provide excellent tests of such effective models. Lifetimes are also important inputs for a wide variety of studies because they are needed to compare measured decay branching fractions to predictions for partial decay widths.

Weakly decaying charmed hadrons have lifetimes ranging from about 0.1 to 1 ps [7]. The world averages of the D^0 and D^+ lifetimes, 410.1 ± 1.5 and 1040 ± 7 fs, are almost exclusively determined from systematically limited permille-precision measurements made by FOCUS two decades ago [7,8]. Recently, the LHCb Collaboration precisely measured the lifetimes of the D_s^+ meson and charmed baryons relative to that of the D^+ meson [9–12]. Such relative measurements minimize systematic uncertainties due to decay-time-biasing event-selection criteria that are particularly severe at hadron colliders. By contrast, experiments at e^+e^- colliders, owing to the reconstruction of large charmed hadron yields without decay-time-biasing selections, have a great potential for absolute lifetime measurements. With the first layer of its vertex detector only 1.4 cm away from the interaction region, the Belle II experiment at the SuperKEKB asymmetric-energy e^+e^- collider [13,14] obtains a decay-time resolution two times better than the Belle and *BABAR* experiments [15], enabling high precision for the measurement of charmed lifetimes with early data. To limit systematic uncertainties this potential must be complemented with an accurate vertex-detector alignment, a precise calibration of final-state particle momenta, and powerful background discrimination.

In this Letter, we report high-precision measurements of the D^0 and D^+ lifetimes using $D^{*+} \to D^0(\to K^-\pi^+)\pi^+$ and $D^{*+} \to D^+(\to K^-\pi^+\pi^+)\pi^0$ decays reconstructed in the data collected by Belle II during 2019 and the first half of 2020 at center-of-mass energies at or near the $\Upsilon(4S)$ resonance. (Charge-conjugate decays are implied throughout.) The data correspond to an integrated luminosity of 72 fb^{-1}. At Belle II, D^{*+} mesons from $e^+e^- \to c\bar{c}$ events are produced with boosts that displace the D^0 and D^+ decay points from those of production by approximately 200 and 500 μm on average, respectively. The decay time is measured from this displacement $\vec{L}$, projected onto the direction of the momentum $\vec{p}$ as $t = m_D \vec{L} \cdot \vec{p}/|\vec{p}|^2$, where m_D is the known mass of the relevant D meson [7]. The decay-time uncertainty σ_t is calculated by propagating the uncertainties in $\vec{L}$ and $\vec{p}$, including their correlations. The lifetimes are measured using a fit to the (t, σ_t) distributions of the reconstructed decay candidates. The sample selection and fit strategy have been optimized and validated using simulation; however, no input from simulation is used in the fit to data. To avoid bias, we inspected the lifetimes measured with the full data sample only after the entire analysis procedure was finalized and all uncertainties were determined. However, we examined the results from the subset of data collected during 2019 (approximately 13% of the total) before the analysis was complete.

The Belle II detector [13] consists of several subsystems arranged in a cylindrical structure around the beam pipe. The tracking system consists of a two-layer silicon-pixel detector (PXD), surrounded by a four-layer double-sided silicon-strip detector (SVD) and a 56-layer central drift chamber (CDC). Only two out of 12 ladders were installed in the second layer of the PXD for this data sample. The combined PXD and SVD system provides average decay-time resolutions of about 70 and 60 fs, respectively, for the D^0 and D^+ decays considered here. A time-of-propagation counter and an aerogel ring-imaging Cherenkov counter that cover the barrel and forward end cap regions of the detector, respectively, are essential for charged-particle identification. The electromagnetic calorimeter fills the remaining volume inside a 1.5 T superconducting solenoid and serves to reconstruct photons and electrons. A dedicated system to identify K_L^0 mesons and muons is installed in the outermost part of the detector. The z axis of the laboratory frame is defined as the central axis of the solenoid, with its positive direction determined by the direction of the electron beam.

The simulation uses KKMC [16] to generate quark-antiquark pairs from e^+e^- collisions, PYTHIA8 [17] for hadronization, EVTGEN [18] for the decay of the generated hadrons, and GEANT4 [19] for the detector response.

The reconstruction [20–22] and selection of the signal candidates avoid any requirement that could bias the decay time or introduce a variation of the efficiency as a function of decay time, as checked in simulation. Events are first selected by vetoing events consistent with Bhabha scattering and by requiring at least three tracks with loose upper bounds on their impact parameters and with transverse momenta greater than 200 MeV/c. These three tracks are not necessarily associated with the decay modes being reconstructed.

Candidate $D^0 \to K^-\pi^+$ decays are formed using pairs of oppositely charged tracks. Each track must have a hit in the first layer of the PXD, at least one hit in the SVD, at least 20 hits in the CDC, and be identified as a kaon, if negative, or else a pion. Low-momentum pion candidates are tracks consistent with originating from the interaction region that are required to have hits both in the SVD and CDC. They are combined with D^0 candidates to form $D^{*+} \to D^0\pi^+$ decays. A global decay-chain vertex fit [23] constrains the tracks according to the decay topology and constrains the D^{*+} candidate to originate from the measured position of the e^+e^- interaction region (IR). Only candidates with fit χ^2 probabilities larger than 0.01 are retained for further analysis. The IR has typical dimensions of 250 μm along the z axis and of 10 and 0.3 μm in the two directions of the transverse plane. Its position and size vary over data taking and are regularly measured using $e^+e^- \to \mu^+\mu^-$ events. The mass of the D^0 candidate $m(K^-\pi^+)$ must be in the range $[1.75, 2.00]$ GeV/c^2. The difference between the D^{*+} and D^0 candidate masses Δm must satisfy $144.94 < \Delta m < 145.90$ MeV/c^2 (± 3 times the Δm resolution around the signal peak). Since the D^0 is assumed to originate from the IR, charmed mesons originating from displaced decays of bottom mesons would bias the lifetime measurement. They are suppressed to a negligible rate by requiring that the momentum of the D^{*+} in the e^+e^- center-of-mass system exceeds 2.5 GeV/c. After requiring $1.851 < m(K^-\pi^+) < 1.878$ GeV/c^2 (signal region), multiple D^{*+} candidates occur in a few per mille of the selected events. In such events, one randomly selected candidate is retained for subsequent analysis.

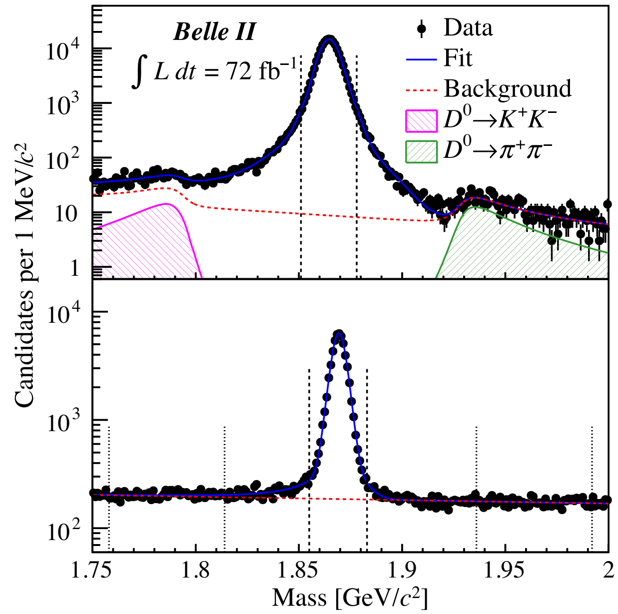

FIG. 1. Mass distributions of (top) $D^0 \to K^-\pi^+$ and (bottom) $D^+ \to K^-\pi^+\pi^+$ candidates with fit projections overlaid. The vertical dashed and (for the bottom plot) dotted lines indicate the signal regions and the sideband, respectively.

The signal region contains approximately 171×10^3 candidates with a signal purity of about 99.8%, as determined from a binned least-squares fit to the $m(K^-\pi^+)$ distribution (Fig. 1). In the fit, the $D^0 \to K^-\pi^+$ signal is modeled with the sum of two Gaussian distributions and a Crystal Ball function [24]; misidentified decays of $D^0 \to \pi^+\pi^-$ and $D^0 \to K^+K^-$, each modeled with a Johnson's S_U distribution [25] with parameters determined from simulation, do not enter the signal region; the remaining background, modeled with an exponential distribution, is dominated by candidates formed by random combinations of particles.

The selection of the $D^{*+} \to D^+(\to K^-\pi^+\pi^+)\pi^0$ candidates follows similar criteria to those for the D^0 mode, but with more stringent requirements to suppress a larger background contamination. Tracks identified as kaons or pions are required to have a hit in the first layer of the PXD, at least one hit in the SVD, and at least 30 hits in the CDC. They are combined to form $D^+ \to K^-\pi^+\pi^+$ candidates. To suppress backgrounds from misreconstructed charmed-hadron decays, such as four-body hadronic or semileptonic decays, the lower-momentum pion must have momentum exceeding 350 MeV/c and the higher-momentum pion must not be identified as a lepton. Candidate $\pi^0 \to \gamma\gamma$ decays are reconstructed using photon candidates from calorimetric energy clusters that are not associated with a track. Each photon energy must be larger than 80, 30, or 60 MeV if detected in the forward, central, or backward region, respectively, of the calorimeter. Neutral-pion candidates with masses in the range $[120, 145]$ MeV/c^2 and momenta larger than 150 MeV/c are combined with D^+ candidates to form $D^{*+} \to D^+\pi^0$ decays. The D^{*+} decay chain is fit using IR and π^0 mass constraints. Only candidates with fit χ^2 probabilities larger than 0.01 are retained. The mass of the D^+ candidate, $m(K^-\pi^+\pi^+)$, must be in the range $[1.75, 2.00]$ GeV/c^2 and the difference between the D^{*+} and D^+ masses in the range $[138, 143]$ MeV/c^2 (± 3 times the Δm resolution around the signal peak). The momentum of the D^{*+} in the e^+e^- center-of-mass system must exceed 2.6 GeV/c to suppress D^{*+} candidates from bottom mesons. This requirement is tighter than that used for D^0 candidates because of the less-precise π^0 -momentum resolution.

The signal region in $m(K^-\pi^+\pi^+)$ is defined as $[1.855, 1.883]$ GeV/c^2 (Fig. 1). It contains approximately 59×10^3 candidates after randomly selecting one D^{*+} candidate for the percent-level fraction of events where more than one is found. A binned least-squares fit to the $m(K^-\pi^+\pi^+)$ distribution identifies about 9% of candidates in the signal region as background. Simulation shows that such background is composed of misreconstructed charmed decays and random track combinations. In the fit, the $D^+ \to K^-\pi^+\pi^+$ signal is modeled with the sum of two Gaussian distributions and a Crystal Ball function; the background is modeled with an exponential distribution.

The lifetimes are determined with unbinned maximum-likelihood fits to the (t, σ_t) distributions of the candidates populating the signal regions. Each signal probability-density function (PDF) is the convolution of an exponential distribution in t with a resolution function that depends on σ_t, multiplied by the PDF of σ_t. In the D^+ case, simulation shows that a Gaussian distribution is sufficient to model the resolution function. The mean of the resolution function is allowed to float in the fit to account for a possible bias in the determination of the decay time; the width is the per-candidate σ_t scaled by a free parameter s to account for a possible misestimation of the decay-time uncertainty. The fit returns $s \approx 1.12$ (1.29) for the D^0 (D^+) sample. In the D^0 case, an additional Gaussian distribution is needed to describe the 3% of candidates with poorer resolution. This second component shares its mean with the principal component but has its own free scaling parameter ($s' \approx 2.5$) for the broader width.

In the D^0 case, the signal region contains a 0.2% fraction of background candidates. Sensitivity to the background contamination and its effects on the decay-time distribution is very limited. For the sake of simplicity, the background is neglected in the fit and a systematic uncertainty is later assigned. In the D^+ case, the signal region contains a non-negligible amount of background, which is accounted for in the fit. The background is modeled using data with $m(K^-\pi^+\pi^+)$ in the *sideband* $[1.758, 1.814] \cup [1.936, 1.992]$ GeV/c^2 (Fig. 1), which is assumed to contain exclusively background candidates and be representative of the background in the signal region, as verified in simulation. The background PDF consists of a zero-lifetime component and two exponential components, all convolved with a Gaussian resolution function having a free mean and a width corresponding to $s\sigma_t$. To better constrain the background parameters, a simultaneous fit to the candidates in the signal region and sideband is performed. The background fraction is Gaussian constrained in the fit to $(8.78 \pm 0.05)\%$, as measured in the $m(K^-\pi^+\pi^+)$ fit.

The PDF of σ_t is a histogram template derived directly from the data. In the fit to the D^0 sample, the template is derived assuming that all candidates in the signal region are signal decays. In the fit to the D^+ sample, the template is derived from the candidates in the signal region by subtracting the scaled distribution of the sideband data. The PDF of σ_t for the background is obtained directly from the sideband data.

The lifetime fits are tested on fully simulated data and on sets of data generated by randomly sampling the PDF with parameters fixed to the values found in the fits to the data. All tests yield unbiased results and expected parameter uncertainties, independent of the assumed values of the D^0 and D^+ lifetimes.

The decay-time distributions of the data, with fit projections overlaid, are shown in Fig. 2. The measured D^0 and D^+ lifetimes $410.5 \pm 1.1(\text{stat}) \pm 0.8(\text{syst})$ fs and $1030.4 \pm 4.7(\text{stat}) \pm 3.1(\text{syst})$ fs, respectively, are consistent with their world averages [7]. The systematic uncertainties arise from the sources listed in Table I and described below. The total systematic uncertainty is the sum in quadrature of the individual components.

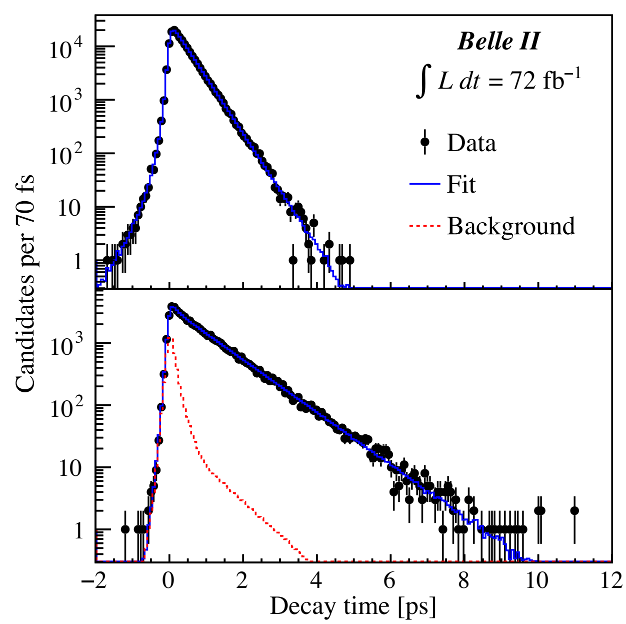

FIG. 2. Decay-time distributions of (top) $D^0 \to K^-\pi^+$ and (bottom) $D^+ \to K^-\pi^+\pi^+$ candidates in their respective signal regions with fit projections overlaid.

TABLE I. Systematic uncertainties.

Source	$\tau(D^0)$ [fs]	$\tau(D^+)$ [fs]
Resolution model	0.16	0.39
Backgrounds	0.24	2.52
Detector alignment	0.72	1.70
Momentum scale	0.19	0.48
Total	0.80	3.10

The decay time and decay-time uncertainty are observed to be correlated in data and simulation reproduces these effects well. The dominant effect is that small σ_t values correspond to larger true decay times (and vice versa). These correlations, when neglected in the fits, result in an imperfect description of the t distribution as a function of σ_t. To quantify the impact on the results, our model that neglects the correlations is fit to 1000 samples of signal-only simulated decays, each the same size as the data. The samples are obtained by resampling, with repetition, a set of simulated e^+e^- collisions corresponding to an integrated luminosity of 500 fb^{-1}. Upper bounds of 0.16 and 0.39 fs on the average absolute deviations of the measured lifetimes from their true values are derived and assigned as the systematic uncertainty due to the imperfect resolution model for the $D^0 \to K^-\pi^+$ and $D^+ \to K^-\pi^+\pi^+$ cases, respectively. For signal decays, the bias of the decay-time resolution function depends nearly linearly on the candidate mass and may not average out when the mass range is restricted. Varying the boundaries of the signal region shows that such a correlation has a negligible effect upon the measured lifetimes.

The background neglected in the $D^0 \to K^-\pi^+$ fit could result in a systematic bias on the measured lifetime. To estimate the size of the bias, we fit our model that neglects the background to 500 resampled sets of simulated e^+e^- collisions, each having the same size and signal-to-background proportion as the data. The measured lifetimes are corrected by subtracting the bias due to the neglected t vs σ_t correlations. The average absolute difference between the resulting value and the simulated lifetime, 0.24 fs, is assigned as a systematic uncertainty due to the neglected background contamination in the $D^0 \to K^-\pi^+$ fit.

The background contamination under the $D^+ \to K^-\pi^+\pi^+$ peak is already accounted for in the fit of the D^+ lifetime using sideband data. In simulation, the sideband (t, σ_t) distribution describes the background (t, σ_t) distribution in the signal region well. The same might not hold in data given that some disagreement is observed between data and simulation in the t distribution of the candidates populating the sideband. We fit to one thousand samples of simulated data obtained by sampling the fit PDF for the signal region and by resampling from the simulated e^+e^- collisions for the sideband. The resulting samples feature sideband data that differ from the background in the signal region with the same level of disagreement as observed between data and simulation. The absolute average difference between the measured and simulated lifetimes, 2.52 fs, is assigned as a systematic uncertainty due to the modeling of the background (t, σ_t) distribution. In the lifetime fit, the fraction of background candidates in the signal region is constrained from the fit to the $m(K^-\pi^+\pi^+)$ distribution. When we change this background fraction to values obtained from fitting to the $m(K^-\pi^+\pi^+)$ distribution with alternative signal and background PDFs, the change in the measured lifetime is negligible.

During data taking, a periodic calibration determines the alignments and surface deformations of the internal components of the PXD and SVD and the relative alignments of the PXD, SVD, and CDC using e^+e^- -collision, beam-background, and cosmic-ray events [26]. Unaccounted-for misalignment can bias the measurement of the charmed decay lengths and hence their decay times. Two sources of uncertainties associated with the alignment procedure are considered: the statistical precision and a possible systematic bias. Their effects are evaluated using simulated signal-only decays reconstructed with a misaligned detector. For the statistical contribution, we consider configurations derived from comparison of alignment parameters determined from data acquired on two consecutive days. These configurations have magnitudes of misalignment comparable to the alignment precision as observed in data averaged over a typical alignment period. For the systematic contribution, we consider configurations derived from simulation studies in which coherent global deformations of the vertex detectors (e.g., radial expansion) are introduced [27]. These deformations have magnitudes, determined by the most misaligned sensors, ranging from about 50 to 700 μm. The alignment procedure determines the magnitude of these deformations within 4 μm accuracy. We consider configurations in which the CDC is perfectly aligned and configurations in which it is misaligned. Possible effects on the determination of the IR are also introduced by using parameters measured on misaligned samples of simulated $e^+e^- \to \mu^+\mu^-$ events, to fully mimic the procedure used for real data. For each misalignment configuration, we fit to the reconstructed signal candidates and estimate the lifetime bias. We estimate the systematic uncertainty due to imperfect detector alignment as the sum in quadrature of the largest biases observed in each of the statistical and systematic contributions. The resulting uncertainties are 0.72 and 1.70 fs for $D^0 \to K^-\pi^+$ and $D^+ \to K^-\pi^+\pi^+$ decays, respectively. The absolute length scale of the vertex detector is determined with a precision significantly better than 0.01% and contributes negligibly to the systematic uncertainty.

The measurement of momenta is calibrated with the peak positions of abundant charmed-, strange-, and bottom-hadron decays. Uncertainty in the scaling of the momenta results in a systematic uncertainty in the lifetimes of 0.19 fs for D^0 and 0.48 fs for D^+. Uncertainties in the D^0 and D^+ masses [7] contribute negligibly to the systematic uncertainty.

As a cross-check, a statistically independent measurement of the D^0 lifetime is performed using approximately 146×10^3 $D^{*+} \to D^0(\to K^-\pi^+\pi^-\pi^+)\pi^+$ decays reconstructed in data with criteria similar to those used for the $D^0 \to K^-\pi^+$ mode and a signal purity greater than 99%. The resulting lifetime, $408.8 \pm 1.2(\text{stat})$ fs, agrees with the value determined from the $D^0 \to K^-\pi^+$ mode.

Finally, the internal consistency of the measurement is tested by repeating the full analysis on various subsets of the data, i.e., running periods and running conditions, charmed-meson momentum and flight direction, and D^{*+} or D^{*-} candidates. We have also studied different selection criteria and sideband definitions. In all cases, the resulting changes in the lifetimes are insignificant.

In conclusion, the D^0 and D^+ lifetimes are measured using $e^+e^- \to c\bar{c}$ data collected by the Belle II experiment corresponding to an integrated luminosity of 72 fb^{-1}. The results,

$$\tau(D^0) = 410.5 \pm 1.1\ (\text{stat}) \pm 0.8\ (\text{syst})\ \text{fs} \quad \text{and} \qquad (1)$$

$$\tau(D^+) = 1030.4 \pm 4.7\ (\text{stat}) \pm 3.1\ (\text{syst})\ \text{fs}, \qquad (2)$$

are the world's most precise to date and are consistent with previous measurements [7]. Assuming that all systematic uncertainties are fully correlated between the two measurements, except those due to the background contamination (assumed uncorrelated), the total correlation coefficient is 18%. The ratio of lifetimes is $\tau(D^+)/\tau(D^0) = 2.510 \pm 0.013(\text{stat}) \pm 0.007(\text{syst})$. These results demonstrate the vertexing capabilities of the Belle II detector and confirm our understanding of systematic effects that impact future decay-time-dependent analyses of neutral-meson mixing and mixing-induced CP violation.

We thank the SuperKEKB group for the excellent operation of the accelerator; the KEK cryogenics group for the efficient operation of the solenoid; the KEK computer group for on-site computing support; and the raw-data centers at BNL, DESY, GridKa, IN2P3, and INFN for off-site computing support. This work was supported by the following funding sources: Science Committee of the Republic of Armenia Grant No. 20TTCG-1C010; Australian Research Council and research Grants No. DP180102629, No. DP170102389, No. DP170102204, No. DP150103061, No. FT130100303, No. FT130100018, and No. FT120100745; Austrian Federal Ministry of Education, Science and Research, Austrian Science Fund No. P 31361-N36, and Horizon 2020 ERC Starting Grant No. 947006 "InterLeptons"; Natural Sciences and Engineering Research Council of Canada, Compute Canada and CANARIE; Chinese Academy of Sciences and research Grant No. QYZDJ-SSW-SLH011, National Natural Science Foundation of China and research Grants No. 11521505, No. 11575017, No. 11675166, No. 11761141009, No. 11705209, and No. 11975076, LiaoNing Revitalization Talents Program under Contract No. XLYC1807135, Shanghai Municipal Science and Technology Committee under Contract No. 19ZR1403000, Shanghai Pujiang Program under Grant No. 18PJ1401000, and the CAS Center for Excellence in Particle Physics (CCEPP); the Ministry of Education, Youth, and Sports of the Czech Republic under Contract No. LTT17020 and Charles University Grants No. SVV 260448 and No. GAUK 404316; European Research Council, Seventh Framework PIEF-GA-2013-622527, Horizon 2020 ERC-Advanced Grants No. 267104 and No. 884719, Horizon 2020 ERC-Consolidator Grant No. 819127, Horizon 2020 Marie Sklodowska-Curie Grant Agreement No. 700525 "NIOBE," and Horizon 2020 Marie Sklodowska-Curie RISE project JENNIFER2 Grant Agreement No. 822070 (European grants); L'Institut National de Physique Nucléaire et de Physique des Particules (IN2P3) du CNRS (France); BMBF, DFG, HGF, MPG, and AvH Foundation (Germany); Department of Atomic Energy under Project Identification No. RTI 4002 and Department of Science and Technology (India); Israel Science Foundation Grant No. 2476/17, U.S.-Israel Binational Science Foundation Grant No. 2016113, and Israel Ministry of Science Grant No. 3-16543; Istituto Nazionale di Fisica Nucleare and the research grants BELLE2; Japan Society for the Promotion of Science, Grant-in-Aid for Scientific Research Grants No. 16H03968, No. 16H03993, No. 16H06492, No. 16K05323, No. 17H01133, No. 17H05405, No. 18K03621, No. 18H03710, No. 18H05226, No. 19H00682, No. 26220706, and No. 26400255, the National Institute of Informatics, and Science Information NETwork 5 (SINET5), and the Ministry of Education, Culture, Sports, Science, and Technology (MEXT) of Japan; National Research Foundation (NRF) of Korea Grants No. 2016R1-D1A1B-01010135, No. 2016R1-D1A1B-02012900, No. 2018R1-A2B-3003643, No. 2018R1-A6A1A-06024970, No. 2018R1-D1A1B-07047294, No. 2019K1-A3A7A-09033840, and No. 2019R1-I1A3A-01058933, Radiation Science Research Institute, Foreign Large-size Research Facility Application Supporting project, the Global Science Experimental Data Hub Center of the Korea Institute of Science and Technology Information and KREONET/GLORIAD; Universiti Malaya RU grant, Akademi Sains Malaysia, and Ministry of Education Malaysia; Frontiers of Science Program Contracts No. FOINS-296, No. CB-221329, No. CB-236394, No. CB-254409, and No. CB-180023, and No. SEP-CINVESTAV research Grant

No. 237 (Mexico); the Polish Ministry of Science and Higher Education and the National Science Center; the Ministry of Science and Higher Education of the Russian Federation, Agreement No. 14.W03.31.0026, and the HSE University Basic Research Program, Moscow; University of Tabuk research Grants No. S-0256-1438 and No. S-0280-1439 (Saudi Arabia); Slovenian Research Agency and research Grants No. J1-9124 and No. P1-0135; Agencia Estatal de Investigacion, Spain Grants No. FPA2014-55613-P and No. FPA2017-84445-P, and No. CIDEGENT/2018/020 of Generalitat Valenciana; Ministry of Science and Technology and research Grants No. MOST106-2112-M-002-005-MY3 and No. MOST107-2119-M-002-035-MY3, and the Ministry of Education (Taiwan); Thailand Center of Excellence in Physics; TUBITAK ULAKBIM (Turkey); National Research Foundation of Ukraine, Project No. 2020.02/0257, and Ministry of Education and Science of Ukraine; the U.S. National Science Foundation and research Grants No. PHY-1807007 and No. PHY-1913789, and the U.S. Department of Energy and research Awards No. DE-AC06-76RLO1830, No. DE-SC0007983, No. DE-SC0009824, No. DE-SC0009973, No. DE-SC0010073, No. DE-SC0010118, No. DE-SC0010504, No. DE-SC0011784, No. DE-SC0012704, No. DE-SC0021274; and the Vietnam Academy of Science and Technology (VAST) under Grant No. DL0000.05/21-23.

[1] M. Neubert, Adv. Ser. Dir. High Energy Phys. **15**, 239 (1998).
[2] N. Uraltsev, in *At the Frontier of Particle Physics*, edited by M. Shifman and B. Ioffe (World Scientific, Singapore, 2001), https://dx.doi.org/10.1142/9789812810458_0034.
[3] A. Lenz and T. Rauh, Phys. Rev. D **88**, 034004 (2013).
[4] A. Lenz, Int. J. Mod. Phys. A **30**, 1543005 (2015).
[5] M. Kirk, A. Lenz, and T. Rauh, J. High Energy Phys. 12 (2017) 068; 06 (2020) 162(E).
[6] H.-Y. Cheng, J. High Energy Phys. 11 (2018) 014.
[7] P. A. Zyla *et al.* (Particle Data Group), Prog. Theor. Exp. Phys. **2020**, 083C01 (2020).
[8] J. M. Link *et al.* (FOCUS Collaboration), Phys. Lett. B **537**, 192 (2002).
[9] R. Aaij *et al.* (LHCb Collaboration), Phys. Rev. Lett. **119**, 101801 (2017).
[10] R. Aaij *et al.* (LHCb Collaboration), Phys. Rev. Lett. **121**, 092003 (2018).
[11] R. Aaij *et al.* (LHCb Collaboration), Phys. Rev. Lett. **121**, 052002 (2018).
[12] R. Aaij *et al.* (LHCb Collaboration), Phys. Rev. D **100**, 032001 (2019).
[13] T. Abe (Belle II Collaboration), arXiv:1011.0352.
[14] K. Akai, K. Furukawa, and H. Koiso, Nucl. Instrum. Methods Phys. Res., Sect. A **907**, 188 (2018).
[15] A. J. Bevan *et al.*, Eur. Phys. J. C **74**, 3026 (2014).
[16] S. Jadach, B. F. L. Ward, and Z. Was, Comput. Phys. Commun. **130**, 260 (2000).
[17] T. Sjöstrand, S. Ask, J. R. Christiansen, R. Corke, N. Desai, P. Ilten, S. Mrenna, S. Prestel, C. O. Rasmussen, and P. Z. Skands, Comput. Phys. Commun. **191**, 159 (2015).
[18] D. J. Lange, Nucl. Instrum. Methods Phys. Res., Sect. A **462**, 152 (2001).
[19] S. Agostinelli *et al.* (GEANT4 Collaboration), Nucl. Instrum. Methods Phys. Res., Sect. A **506**, 250 (2003).
[20] T. Kuhr, C. Pulvermacher, M. Ritter, T. Hauth, and N. Braun (Belle II Framework Software Group), Comput. Software Big Sci. **3**, 1 (2019).
[21] V. Bertacchi *et al.* (Belle II Tracking Group), Comput. Phys. Commun. **259**, 107610 (2021).
[22] S. Kurz, Proceedings, Connecting the dots 2020, Reports No. PROC-CTD2020-40, No. BELLE2-CONF-PROC-2020-009.
[23] J.-F. Krohn *et al.* (Belle II Analysis Software Group), Nucl. Instrum. Methods Phys. Res., Sect. A **976**, 164269 (2020).
[24] T. Skwarnicki, A study of the radiative cascade transitions between the Upsilon-prime and Upsilon resonances, Ph.D thesis, Institute of Nuclear Physics, Krakow, 1986 [Report No. DESY-F31-86-02].
[25] N. L. Johnson, Biometrika **36**, 149 (1949).
[26] T. Bilka *et al.*, EPJ Web Conf. **245**, 02023 (2020).
[27] D. Brown, A. Gritsan, Z. Guo, and D. Roberts, Nucl. Instrum. Methods Phys. Res., Sect. A **603**, 467 (2009).

Precise Measurement of the D_s^+ Lifetime at Belle II

I. Adachi, L. Aggarwal, H. Aihara, N. Akopov, A. Aloisio, N. Anh Ky, D. M. Asner, H. Atmacan, T. Aushev, V. Aushev, M. Aversano, V. Babu, H. Bae, S. Bahinipati, P. Bambade, Sw. Banerjee, M. Barrett, J. Baudot, M. Bauer, A. Baur, A. Beaubien, J. Becker, P. K. Behera, J. V. Bennett, F. U. Bernlochner, V. Bertacchi, M. Bertemes, E. Bertholet, M. Bessner, S. Bettarini, B. Bhuyan, F. Bianchi, T. Bilka, D. Biswas, D. Bodrov, A. Bondar, A. Bozek, M. Bračko, P. Branchini, R. A. Briere, T. E. Browder, A. Budano, S. Bussino, M. Campajola, L. Cao, G. Casarosa, C. Cecchi, J. Cerasoli, M.-C. Chang, P. Chang, P. Cheema, V. Chekelian, B. G. Cheon, K. Chilikin, K. Chirapatpimol, H.-E. Cho, K. Cho, S.-K. Choi, S. Choudhury, J. Cochran, L. Corona, S. Das, F. Dattola, S. A. De La Motte, G. de Marino, G. De Nardo, M. De Nuccio, G. De Pietro, R. de Sangro, M. Destefanis, S. Dey, R. Dhamija, A. Di Canto, F. Di Capua, J. Dingfelder, Z. Doležal, I. Domínguez Jiménez, T. V. Dong, M. Dorigo, K. Dort, S. Dreyer, S. Dubey, G. Dujany, P. Ecker, D. Epifanov, P. Feichtinger, D. Ferlewicz, C. Finck, G. Finocchiaro, A. Fodor, F. Forti, A. Frey, B. G. Fulsom, A. Gabrielli, E. Ganiev, M. Garcia-Hernandez, A. Garmash, G. Gaudino, V. Gaur, A. Gaz, A. Gellrich, G. Ghevondyan, D. Ghosh, H. Ghumaryan, G. Giakoustidis, R. Giordano, A. Giri, A. Glazov, B. Gobbo, R. Godang, O. Gogota, P. Goldenzweig, W. Gradl, E. Graziani, D. Greenwald, Z. Gruberová, T. Gu, Y. Guan, K. Gudkova, Y. Han, K. Hayasaka, H. Hayashii, S. Hazra, C. Hearty, I. Heredia de la Cruz, A. Hershenhorn, T. Higuchi, E. C. Hill, M. Hoek, M. Hohmann, C.-L. Hsu, T. Humair, T. Iijima, K. Inami, N. Ipsita, A. Ishikawa, S. Ito, R. Itoh, M. Iwasaki, P. Jackson, W. W. Jacobs, D. E. Jaffe, E.-J. Jang, Q. P. Ji, S. Jia, Y. Jin, H. Junkerkalefeld, A. B. Kaliyar, J. Kandra, G. Karyan, T. Kawasaki, F. Keil, C. Ketter, C. Kiesling, C.-H. Kim, D. Y. Kim, K.-H. Kim, Y.-K. Kim, H. Kindo, K. Kinoshita, P. Kodyš, T. Koga, S. Kohani, K. Kojima, A. Korobov, S. Korpar, R. Kowalewski, T. M. G. Kraetzschmar, P. Križan, P. Krokovny, T. Kuhr, J. Kumar, M. Kumar, R. Kumar, K. Kumara, A. Kuzmin, Y.-J. Kwon, S. Lacaprara, Y.-T. Lai, T. Lam, J. S. Lange, M. Laurenza, R. Leboucher, F. R. Le Diberder, P. Leitl, D. Levit, P. M. Lewis, L. K. Li, J. Libby, Q. Y. Liu, Z. Q. Liu, D. Liventsev, S. Longo, T. Lueck, C. Lyu, Y. Ma, M. Maggiora, S. P. Maharana, R. Maiti, S. Maity, R. Manfredi, E. Manoni, M. Mantovano, D. Marcantonio, S. Marcello, C. Marinas, C. Martellini, A. Martini, T. Martinov, L. Massaccesi, M. Masuda, T. Matsuda, K. Matsuoka, D. Matvienko, S. K. Maurya, J. A. McKenna, R. Mehta, F. Meier, M. Merola, F. Metzner, M. Milesi, C. Miller, M. Mirra, K. Miyabayashi, G. B. Mohanty, N. Molina-Gonzalez, S. Mondal, S. Moneta, H.-G. Moser, M. Mrvar, R. Mussa, I. Nakamura, Y. Nakazawa, A. Narimani Charan, M. Naruki, Z. Natkaniec, A. Natochii, L. Nayak, G. Nazaryan, N. K. Nisar, S. Nishida, H. Ono, F. Otani, E. R. Oxford, P. Pakhlov, G. Pakhlova, A. Paladino, A. Panta, E. Paoloni, S. Pardi, A. Passeri, S. Patra, S. Paul, T. K. Pedlar, I. Peruzzi, R. Peschke, R. Pestotnik, F. Pham, M. Piccolo, L. E. Piilonen, T. Podobnik, S. Pokharel, C. Praz, S. Prell, E. Prencipe, M. T. Prim, H. Purwar, P. Rados, G. Raeuber, S. Raiz, M. Reif, S. Reiter, M. Remnev, I. Ripp-Baudot, G. Rizzo, J. M. Roney, A. Rostomyan, N. Rout, G. Russo, S. Sandilya, A. Sangal, L. Santelj, Y. Sato, V. Savinov, B. Scavino, C. Schmitt, C. Schwanda, A. J. Schwartz, Y. Seino, A. Selce, K. Senyo, J. Serrano, M. E. Sevior, C. Sfienti, W. Shan, X. D. Shi, T. Shillington, J.-G. Shiu, D. Shtol, A. Sibidanov, F. Simon, R. J. Sobie, M. Sobotzik, A. Soffer, A. Sokolov, E. Solovieva, S. Spataro, B. Spruck, M. Starič, P. Stavroulakis, Z. S. Stottler, R. Stroili, M. Sumihama, H. Svidras, M. Takahashi, M. Takizawa, U. Tamponi, K. Tanida, F. Tenchini, O. Tittel, D. Tonelli, E. Torassa, K. Trabelsi, I. Tsaklidis, K. Unger, Y. Unno, K. Uno, S. Uno, P. Urquijo, Y. Ushiroda, S. E. Vahsen, R. van Tonder, K. E. Varvell, M. Veronesi, V. S. Vismaya, L. Vitale, R. Volpe, B. Wach, S. Wallner, E. Wang, M.-Z. Wang, X. L. Wang, Z. Wang, A. Warburton, M. Watanabe, C. Wessel, E. Won, X. P. Xu, B. D. Yabsley, S. Yamada, W. Yan, S. B. Yang, K. Yoshihara, C. Z. Yuan, Y. Yusa, Y. Zhang, V. Zhilich, J. S. Zhou, Q. D. Zhou, V. I. Zhukova, and R. Žlebčík

(Belle II Collaboration)

(Received 1 June 2023; accepted 14 September 2023; published 25 October 2023)

We measure the lifetime of the D_s^+ meson using a data sample of 207 fb^{-1} collected by the Belle II experiment running at the SuperKEKB asymmetric-energy e^+e^- collider. The lifetime is determined by fitting the decay-time distribution of a sample of 116×10^3 $D_s^+ \to \phi\pi^+$ decays. Our result is $\tau_{D_s^+} = (499.5 \pm 1.7 \pm 0.9)$ fs, where the first uncertainty is statistical and the second is systematic. This result is significantly more precise than previous measurements.

DOI: 10.1103/PhysRevLett.131.171803

The lifetime of a particle, like its mass and spin, is one of the fundamental properties that distinguishes it from other particles. The lifetime is the reciprocal of the total decay width, which is the sum of all partial decay widths. Each partial width is proportional to the magnitude squared of the sum of all decay amplitudes to a final state, and thus every decay amplitude potentially affects the lifetime. As a result, the lifetime can provide information about amplitudes that are difficult to measure or calculate.

Lifetimes of D mesons are dominated by partial widths to hadronic final states. The relatively long lifetime of the D^+ meson, 2.5 times that of the D^0, implies there is a reduction in hadronic partial widths. This reduction is attributed to destructive interference between a "spectator" amplitude and a color-suppressed amplitude (Fig. 1, left) [1]. The small difference in lifetimes of the D^0 and D_s^+ mesons is attributed to the dominance of the spectator amplitude for hadronic decays and different color factors that enter subdominant "exchange" (D^0) and "annihilation" (D_s^+) amplitudes [2]. The latter amplitude for D_s^+ decays (Fig. 1, right) is Cabibbo favored and thus plays a larger role than it does for D^+ decays, in which it is Cabibbo suppressed.

Hadron lifetimes are difficult to calculate theoretically, as they depend on nonperturbative effects arising from quantum chromodynamics (QCD). Thus, lifetime calculations are performed using phenomenological methods such as the heavy quark expansion [3–8]. Comparing calculated values with measured values improves our understanding of QCD, which leads to improved QCD calculations of other quantities such as hadron masses, structure functions, etc. [9]. Measurements of the D_s^+ lifetime have been reported by many experiments [10–16]; the world average value is $\tau_{D_s^+} = (504 \pm 4)$ fs [17]. In this Letter, we present a new measurement of the D_s^+ lifetime using $D_s^+ \to \phi\pi^+$ decays [18] reconstructed in 207 fb^{-1} of data collected by the Belle II experiment [19,20]. The data were recorded at an e^+e^- center-of-mass energy corresponding to the $\Upsilon(4S)$ resonance, and at an energy slightly below. Our result has significantly greater precision than the world average value.

The Belle II experiment runs at the SuperKEKB e^+e^- collider [21]. The overall detector [19] has a cylindrical geometry and includes a two-layer silicon-pixel detector (PXD) surrounded by a four-layer double-sided silicon-strip detector (SVD) [22] and a 56-layer central drift chamber (CDC). These detectors reconstruct tracks (trajectories of charged particles). Only one sixth of the second layer of the PXD was installed for the data analyzed here. The axis of symmetry of these detectors, defined as the z axis, is almost coincident with the direction of the electron beam. Surrounding the CDC is a time-of-propagation counter (TOP) [23] in the central region, and an aerogel-based ring-imaging Cherenkov counter (ARICH) in the forward region. These detectors provide charged-particle identification. Surrounding the TOP and ARICH is an electromagnetic calorimeter based on CsI(Tl) crystals that provides energy and timing measurements for photons and electrons. Outside of the calorimeter is an iron flux return for a superconducting solenoid magnet. The flux return is instrumented with resistive plate chambers and plastic scintillator modules to detect muons, K_L^0 mesons, and neutrons. The solenoid magnet provides a 1.5 T magnetic field that is parallel to the z axis.

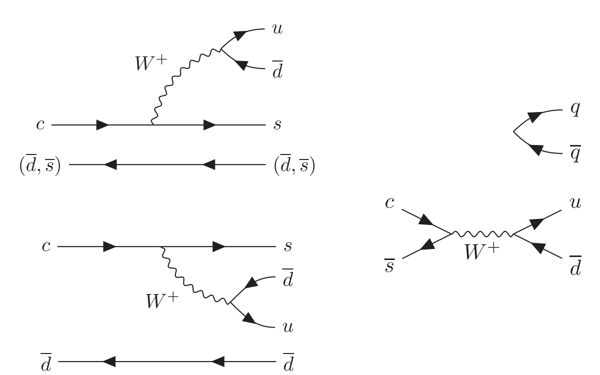

FIG. 1. Left: Spectator amplitude (top) and color-suppressed amplitude (bottom). Right: Annihilation amplitude.

We use Monte Carlo (MC) simulated events to optimize event selection criteria, calculate reconstruction efficiencies, and study sources of background. We generate $e^+e^- \to q\bar{q}\,(q = u, d, s, c, b)$ events using the KKMC package [24] and simulate quark hadronization using the PYTHIA8 package [25]. Hadron decays are simulated using EvtGen [26], and the detector response is simulated using GEANT4 [27]. Final-state radiation is included in the simulation via PHOTOS [28]. Both MC-simulated events and collision data are reconstructed using the Belle II analysis software framework [29,30]. To avoid introducing bias in our analysis, we analyze the data in a "blind" manner, i.e., we finalize all selection criteria and the fitting procedure before evaluating the lifetime of signal candidates.

We reconstruct $D_s^+ \to \phi\pi^+$ decays by first reconstructing $\phi \to K^+K^-$ decays and subsequently pairing the ϕ candidate with a π^+ track. We select well-measured tracks by requiring that each track have at least one hit (measured point) in the PXD, four hits in the SVD, and 30 hits in the CDC. We select tracks that originate from near the interaction point (IP) by requiring $|\delta z| < 2.0$ cm and $\delta r < 0.5$ cm, where δz is the displacement of the track from the IP along the z axis, and δr is the radial displacement in the plane transverse to the z axis. The IP position is measured at regular intervals of data taking using $e^+e^- \to \mu^+\mu^-$ events. The spread of the IP position is typically 250 μm in the z direction, 10 μm in the transverse horizontal direction (x), and only 0.3 μm in the transverse vertical direction (y). We have checked that none of the above requirements, nor any subsequent selection requirements, bias the lifetime measurement.

We identify tracks as pions or kaons based on Cherenkov light recorded in the TOP and ARICH, and specific ionization (dE/dx) information from the CDC and SVD. This information is combined to calculate a likelihood $\mathcal{L}_{K,\pi}$ for a track to be a K^+ or π^+. Tracks having a ratio $\mathcal{L}_K/(\mathcal{L}_K + \mathcal{L}_\pi) > 0.60$ are identified as kaon candidates, while tracks having $\mathcal{L}_K/(\mathcal{L}_K + \mathcal{L}_\pi) < 0.55$ are identified as pion candidates. These requirements are 90% and 95% efficient for kaons and pions, respectively.

To reconstruct $\phi \to K^+K^-$ decays, we combine two kaon candidate tracks having opposite charge and an invariant mass satisfying $1.010\ \mathrm{GeV}/c^2 < M(K^+K^-) < 1.030\ \mathrm{GeV}/c^2$. This selected range retains 91% of $\phi \to K^+K^-$ decays. We pair ϕ candidates with π^+ tracks to form D_s^+ candidates and require that the invariant mass satisfy a loose requirement of $1.922\ \mathrm{GeV}/c^2 < M(\phi\pi^+) < 2.020\ \mathrm{GeV}/c^2$. We fit the three tracks to a common vertex using the TreeFitter algorithm [31]. The vertex position resulting from the fit is taken as the decay vertex of the D_s^+. The fit includes a constraint that the D_s^+ trajectory be consistent with originating from the IP; this constraint improves the resolution on the D_s^+ decay time by a factor of 3.

To eliminate D_s^+ mesons originating from B decays, which would not have a properly determined decay time, we require that the momentum of the D_s^+ in the e^+e^- center-of-mass frame be greater than $2.5\ \mathrm{GeV}/c$. This selection eliminates all D_s^+ mesons from B decays while retaining 67% of those produced via $e^+e^- \to c\bar{c}$. We reduce background arising from random combinations of ϕ and π^+ candidates by requiring $|\cos\theta_K| > 0.45$, where θ_K is the angle in the ϕ rest frame between the K^- momentum and the direction of the D_s^+. This requirement reduces combinatorial background by 40% while retaining 90% of signal decays. After applying all selection criteria, about 2% of events have more than one $D_s^+ \to \phi\pi^+$ candidate. False signal candidates arise mainly from combinations of ϕ decays with unrelated π^+ tracks. These do not peak in $M(\phi\pi^+)$ and are counted as background in our fits for signal yield and D_s^+ lifetime; consequently, they have a negligible effect on the fitted lifetime. We thus retain all signal candidates.

The final $M(\phi\pi^+)$ distribution is shown in Fig. 2. We perform an unbinned maximum likelihood fit to $M(\phi\pi^+)$ to determine the yield of $D_s^+ \to \phi\pi^+$ decays. The signal shape is modeled as the sum of two Gaussian functions and an asymmetric Student's t distribution. The background contains no peaking structure (> 95% consists of random combinations of ϕ and π^+ candidates) and is well-modeled by a second-order polynomial. To measure the D_s^+ lifetime, we select candidates having an invariant mass satisfying $1.960\ \mathrm{GeV}/c^2 < M(\phi\pi^+) < 1.976\ \mathrm{GeV}/c^2$. This range retains 95% of $D_s^+ \to \phi\pi^+$ decays. In this signal region, the fit yields 115 560 signal decays and 9970 background events; the signal purity (ratio of signal over the total) is 92%.

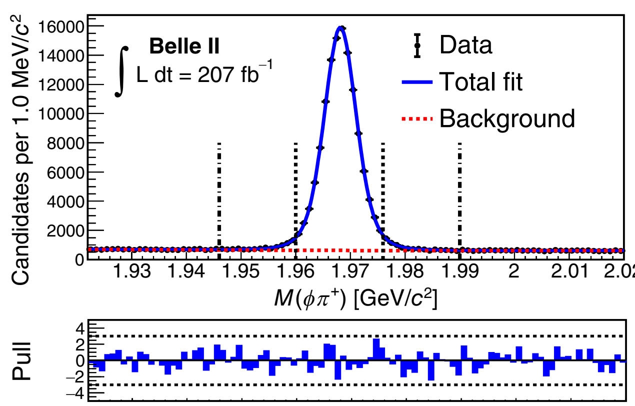

FIG. 2. Distribution of $M(\phi\pi^+)$ for $D_s^+ \to \phi\pi^+$ candidates, with the fit result overlaid. Black dots correspond to the data; the red dashed curve shows the background component; and the blue solid curve shows the overall fit result. Vertical dotted lines denote the signal region, and vertical dot-dashed lines denote the upper and lower boundaries of the lower and upper sidebands (see text). The corresponding pull distribution is shown in the lower panel, where the pull is defined as (data − fit)/(statistical uncertainty in data).

The decay time of a D_s^+ candidate is calculated as

$$t = \left(\frac{\vec{d}\cdot\vec{p}}{p^2}\right) m_{D_s^+}, \qquad (1)$$

where $\vec{d}$ is the displacement vector from the IP to the D_s^+ decay vertex, $\vec{p}$ is the D_s^+ momentum, and $m_{D_s^+}$ is the known D_s^+ mass [17]. The average resolution on t is 108 fs. We determine the D_s^+ lifetime by performing an unbinned maximum likelihood fit to two observables: the decay time t and the per-candidate uncertainty on t (σ_t) as calculated from the uncertainties on $\vec{d}$ and $\vec{p}$. The likelihood function for the ith candidate is given by

$$\mathcal{L}(\tau|t^i,\sigma_t^i) = f_{\rm sig}P_{\rm sig}(t^i|\tau,\sigma_t^i)P_{\rm sig}(\sigma_t^i) + (1-f_{\rm sig})P_{\rm bkg}(t^i|\sigma_t^i)P_{\rm bkg}(\sigma_t^i), \qquad (2)$$

where $f_{\rm sig}$ is the fraction of events that are signal $D_s^+ \to \phi\pi^+$ decays; $P_{\rm sig}(t|\tau,\sigma_t)$ and $P_{\rm bkg}(t|\sigma_t)$ are probability density functions (PDFs) for signal and background events for a reconstructed decay time t, given a D_s^+ lifetime τ for signal and an uncertainty σ_t; and $P_{\rm sig}(\sigma_t)$ and $P_{\rm bkg}(\sigma_t)$ are the respective PDFs for σ_t. To reduce highly mismeasured events that are difficult to simulate, we impose loose requirements -2000 fs $< t <$ 4000 fs and $\sigma_t <$ 900 fs. These requirements reject less than 0.1% of signal candidates.

The signal PDF is the convolution of an exponential function and a resolution function R:

$$P_{\rm sig}(t^i|\tau,\sigma_t^i) = \frac{1}{\tau}\int e^{-t'/\tau}R(t^i-t';\mu,s,\sigma_t^i)dt', \qquad (3)$$

where $R(t^i-t';\mu,s,\sigma_t^i)$ is a single Gaussian function with mean μ and a per-candidate standard deviation $s\times\sigma_t^i$. The scaling factor s accounts for under- or over-estimation of the uncertainty σ_t^i. The PDF $P_{\rm bkg}(t|\sigma_t)$ is determined by fitting the decay-time distribution of events in the $M(\phi\pi^+)$ "upper" sideband 1.990 GeV$/c^2 < M(\phi\pi^+) <$ 2.020 GeV$/c^2$, which has no contamination from signal decays with final-state radiation. We model $P_{\rm bkg}(t|\sigma_t)$ as the sum of three asymmetric Gaussians with a common mean. We use MC simulation to verify that the decay-time distribution of background events in this sideband describes well the decay-time distribution of background events in the signal region.

The PDFs $P_{\rm sig}(\sigma_t)$ and $P_{\rm bkg}(\sigma_t)$ are taken to be finely binned histograms. The former is determined from the σ_t distribution of events in the signal region, after subtracting the σ_t distribution of events in the $M(\phi\pi^+)$ sideband. The resulting $P_{\rm sig}(\sigma_t)$ distribution matches well that of MC-simulated signal decays. The $P_{\rm bkg}(\sigma_t)$ distribution is determined from background events in the $M(\phi\pi^+)$ sideband. The signal fraction $f_{\rm sig}$ is obtained from the earlier fit to the $M(\phi\pi^+)$ distribution (Fig. 2) and fixed in this fit. Thus, there are three floated parameters: the lifetime τ, and the mean parameter μ and scaling factor s of the resolution function. These are determined by maximizing the total log-likelihood $\sum_i \ln\mathcal{L}(\tau|t^i,\sigma_t^i)$, where the sum runs over all events in the signal region.

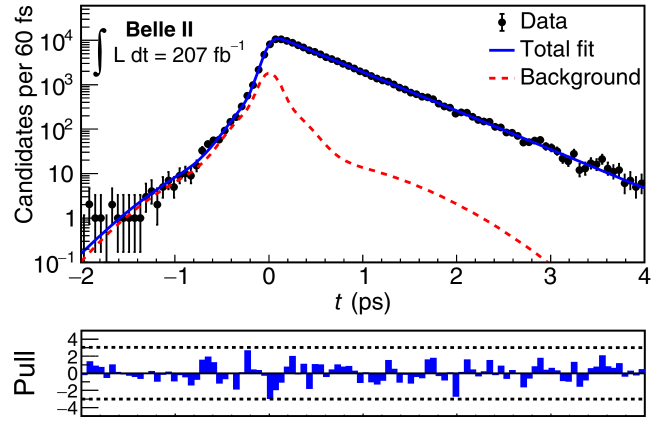

FIG. 3. Distribution of t for $D_s^+ \to \phi\pi^+$ candidates, with the fit result overlaid. Black dots correspond to the data; the red dashed curve shows the background component; and the blue solid curve shows the overall fit result. The corresponding pull distribution is shown in the lower panel.

The result of the fit is $\tau = 498.70 \pm 1.71$ fs, where the uncertainty is statistical only. The projection of the fit for t is shown in Fig. 3 along with the resulting pulls; the χ^2 divided by the number of degrees of freedom $(100-4=96)$ is 1.02. The values $\mu = 0.56 \pm 0.86$ fs and $s = 1.22 \pm 0.01$ obtained for the resolution function are similar to those obtained from MC-simulated samples.

The main systematic uncertainties are listed in Table I and evaluated as follows. Uncertainty arising from possible mismodeling of the detector response and possible correlations between t and σ_t not accounted for by the resolution function is assessed by fitting a large ensemble of MC signal events. The mean of the fitted lifetime values is calculated, and the difference of -0.85 fs between the mean value and the input value is used to correct the fitted

TABLE I. Summary of systematic uncertainties.

Source	Uncertainty (fs)
Resolution function	±0.43
Background (t,σ_t) distribution	±0.40
Binning of σ_t histogram PDF	±0.10
Imperfect detector alignment	±0.56
Sample purity	±0.09
Momentum scale factor	±0.28
D_s^+ mass	±0.02
Total	±0.87

lifetime. We assign half of this correction as a systematic uncertainty.

There is uncertainty arising from modeling the background decay-time distribution. We model this distribution using background events in the upper $M(\phi\pi^+)$ sideband $1.990\ \mathrm{GeV}/c^2 < M(\phi\pi^+) < 2.020\ \mathrm{GeV}/c^2$. To evaluate uncertainty in this model, we choose a lower sideband $1.922\ \mathrm{GeV}/c^2 < M(\phi\pi^+) < 1.946\ \mathrm{GeV}/c^2$, a combination of the two sidebands, and also the MC-simulated background distribution in the signal region. The largest difference observed between the resulting fitted lifetime and our nominal result is assigned as a systematic uncertainty.

We model both signal and background σ_t distributions using histogram PDFs, and there is systematic uncertainty arising from our choice for the number of bins (i.e., statistical fluctuations of the sideband data used to obtain the histogram PDF). We evaluate this by changing the number of bins from the nominal value (80) to other values in the range 60–400. For each choice of binning, we refit for τ. The largest difference observed between the resulting values and our nominal value is taken as a systematic uncertainty.

As measuring the decay time depends on a precise determination of the displacement vector $\vec{d}$ and momentum $\vec{p}$ [Eq. (1)], there is uncertainty arising from possible misalignments of the PXD, SVD, and CDC detectors. We study the effect of such misalignment using MC events reconstructed with various misalignments. Each sample is equivalent in size to that of the collision data used. The difference between the fitted value of τ and the result obtained with no misalignment is recorded, and the root-mean-square (r.m.s.) of the distribution of differences is taken as the systematic uncertainty due to possible detector misalignment.

There is uncertainty arising from the fraction of signal candidates (f_{sig}), which is fixed in the decay-time fit to the value obtained from the fit to the $M(\phi\pi^+)$ distribution. We vary this parameter by its uncertainty and take the resulting change in the fitted lifetime as a systematic uncertainty.

There is an uncertainty arising from the global momentum scale of the detector, which is calibrated using the peak position of $D^0 \to K^-\pi^+$ decays. We evaluate this by varying the global scale factor by its uncertainty ($\pm0.06\%$) and assigning the resulting variation in the fitted lifetime as a systematic uncertainty.

Finally, we include a systematic uncertainty due to uncertainty in the D_s^+ mass [17], which is used to calculate the decay time from the vectors $\vec{d}$ and $\vec{p}$ [see Eq. (1)]. The total systematic uncertainty is obtained by adding together all individual contributions (listed in Table I) in quadrature. The result is ±0.87 fs.

As a final check of our analysis procedure, we divide the data sample into subsets based on D_s^+ (or D_s^-) charge, D_s^+ momentum, D_s^+ polar angle, D_s^+ azimuthal angle, and data-collection (run) period, and we measure the lifetime separately for each subset. All measured values are consistent with statistical fluctuations about the overall result. The fitted lifetime for different run periods is plotted in Fig. 4.

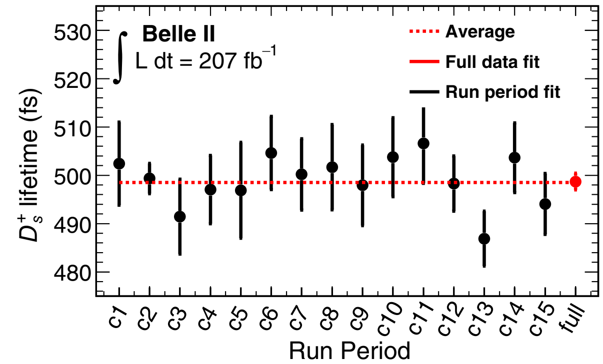

FIG. 4. Fitted lifetime for different run periods (c1–c15). For these fits, the parameters of the resolution function are fixed to the overall fitted values. All values are consistent with the overall result, which is plotted as a red data point. The red dashed line shows the average of the lifetime results for the different run periods.

In summary, we have used 116×10^3 $D_s^+ \to \phi\pi^+$ decays reconstructed in 207 fb^{-1} of data recorded by Belle II in e^+e^- collisions at or near the $\Upsilon(4S)$ resonance to measure the D_s^+ lifetime. The result is

$$\tau_{D_s^+} = (499.5 \pm 1.7 \pm 0.9)\ \mathrm{fs}, \qquad (4)$$

where the first uncertainty is statistical and the second is systematic. This is the most precise measurement to date. It is consistent with, but has half the uncertainty of, the current world-average value of (504 ± 4) fs [17]. It is also consistent with theory predictions [3,6,8]. The high precision results from significantly improved decay-time resolution as compared to previous e^+e^- experiments. This is due to the smaller beam sizes of SuperKEKB, which reduce uncertainty on the IP, and to the smaller radius of the first layer of the vertex detector.

This work, based on data collected using the Belle II detector, which was built and commissioned prior to March 2019, was supported by Science Committee of the Republic of Armenia Grant No. 20TTCG-1C010; Australian Research Council and research Grants No. DP200101792, No. DP210101900, No. DP210102831, No. DE220100462, No. LE210100098, and No. LE230100085; Austrian Federal Ministry of Education, Science and Research, Austrian Science Fund No. P 31361-N36 and No. J4625-N, and Horizon 2020 ERC Starting Grant No. 947006 "InterLeptons"; Natural Sciences and Engineering Research Council of Canada, Compute Canada and CANARIE; National Key R&D Program of China under Contract No. 2022YFA1601903, National Natural Science Foundation of China and research

Grants No. 11575017, No. 11761141009, No. 11705209, No. 11975076, No. 12135005, No. 12150004, No. 12161141008, and No. 12175041, and Shandong Provincial Natural Science Foundation Project ZR2022JQ02; the Ministry of Education, Youth, and Sports of the Czech Republic under Contract No. LTT17020 and Charles University Grant No. SVV 260448 and the Czech Science Foundation Grant No. 22-18469S; European Research Council, Seventh Framework PIEF-GA-2013-622527, Horizon 2020 ERC-Advanced Grants No. 267104 and No. 884719, Horizon 2020 ERC-Consolidator Grant No. 819127, Horizon 2020 Marie Sklodowska-Curie Grant Agreement No. 700525 “NIOBE” and No. 101026516, and Horizon 2020 Marie Sklodowska-Curie RISE project JENNIFER2 Grant Agreement No. 822070 (European grants); L’Institut National de Physique Nucléaire et de Physique des Particules (IN2P3) du CNRS (France); BMBF, DFG, HGF, MPG, and AvH Foundation (Germany); Department of Atomic Energy under Project Identification No. RTI 4002 and Department of Science and Technology (India); Israel Science Foundation Grant No. 2476/17, U.S.-Israel Binational Science Foundation Grant No. 2016113, and Israel Ministry of Science Grant No. 3-16543; Istituto Nazionale di Fisica Nucleare and the research grants BELLE2; Japan Society for the Promotion of Science, Grant-in-Aid for Scientific Research Grants No. 16H03968, No. 16H03993, No. 16H06492, No. 16K05323, No. 17H01133, No. 17H05405, No. 18K03621, No. 18H03710, No. 18H05226, No. 19H00682, No. 22H00144, No. 26220706, and No. 26400255, the National Institute of Informatics, and Science Information NETwork 5 (SINET5), and the Ministry of Education, Culture, Sports, Science, and Technology (MEXT) of Japan; National Research Foundation (NRF) of Korea Grants No. 2016R1D1A1B02012900, No. 2018R1A2B3003643, No. 2018R1A6A1A06024970, No. 2018R1D1A1 B07047294, No. 2019R1I1A3A01058933, No. 2022 R1A2C1003993, and No. RS-2022-00197659, Radiation Science Research Institute, Foreign Large-size Research Facility Application Supporting project, the Global Science Experimental Data Hub Center of the Korea Institute of Science and Technology Information and KREONET/GLORIAD; Universiti Malaya RU grant, Akademi Sains Malaysia, and Ministry of Education Malaysia; Frontiers of Science Program Contracts No. FOINS-296, No. CB-221329, No. CB-236394, No. CB-254409, and No. CB-180023, and No. SEP-CINVESTAV research Grant No. 237 (Mexico); the Polish Ministry of Science and Higher Education and the National Science Center; the Ministry of Science and Higher Education of the Russian Federation, Agreement No. 14.W03.31.0026, and the HSE University Basic Research Program, Moscow; University of Tabuk research Grants No. S-0256-1438 and No. S-0280-1439 (Saudi Arabia); Slovenian Research Agency and research Grants No. J1-9124 and No. P1-0135; Agencia Estatal de Investigacion, Spain Grant No. RYC2020-029875-I and Generalitat Valenciana, Spain Grant No. CIDEGENT/2018/020 Ministry of Science and Technology and research Grants No. MOST106-2112-M-002-005-MY3 and No. MOST107-2119-M-002-035-MY3, and the Ministry of Education (Taiwan); Thailand Center of Excellence in Physics; TUBITAK ULAKBIM (Turkey); National Research Foundation of Ukraine, project No. 2020.02/0257, and Ministry of Education and Science of Ukraine; the U.S. National Science Foundation and research Grants No. PHY-1913789 and No. PHY-2111604, and the U.S. Department of Energy and research Awards No. DE-AC06-76RLO1830, No. DE-SC0007983, No. DE-SC0009824, No. DE-SC0009973, No. DE-SC0010007, No. DE-SC0010073, No. DE-SC0010118, No. DE-SC0010504, No. DE-SC0011784, No. DE-SC0012704, No. DE-SC0019230, No. DE-SC0021274, No. DE-SC0022350, No. DE-SC0023470; and the Vietnam Academy of Science and Technology (VAST) under Grant No. DL0000.05/21-23. We thank the SuperKEKB team for delivering high-luminosity collisions; the KEK cryogenics group for the efficient operation of the detector solenoid magnet; the KEK computer group and the NII for on-site computing support and SINET6 network support; and the raw-data centers at BNL, DESY, GridKa, IN2P3, INFN, and the University of Victoria for offsite computing support.

These acknowledgements are not to be interpreted as an endorsement of any statement made by any of our institutes, funding agencies, governments, or their representatives.

[1] R. J. Morrison and M. S. Witherell, Annu. Rev. Nucl. Part. Sci. **39**, 183 (1989).
[2] T. E. Browder, K. Honscheid, and D. Pedrini, Annu. Rev. Nucl. Part. Sci. **46**, 395 (1996).
[3] A. Lenz, Int. J. Mod. Phys. A **30**, 1543005 (2015).
[4] M. Neubert, Adv. Ser. Dir. High Energy Phys. **15**, 239 (1998).
[5] N. Uraltsev, arXiv:hep-ph/0010328.
[6] A. Lenz and T. Rauh, Phys. Rev. D **88**, 034004 (2013).
[7] M. Kirk, A. Lenz, and T. Rauh, J. High Energy Phys. 12 (2017) 068; 06 (2020) 162(E).
[8] J. Gratrex, B. Melić, and I. Nišandžić, J. High Energy Phys. 07 (2022) 058.
[9] Y. Aoki *et al.* (Flavour Lattice Averaging Group (FLAG)), Eur. Phys. J. C **82**, 869 (2022).
[10] R. Aaij *et al.* (LHCb Collaboration), Phys. Rev. Lett. **119**, 101801 (2017).
[11] J. M. Link *et al.* (FOCUS Collaboration), Phys. Rev. Lett. **95**, 052003 (2005).
[12] M. Iori *et al.* (SELEX Collaboration), Phys. Lett. B **523**, 22 (2001).

[13] E. M. Aitala *et al.* (E791 Collaboration), Phys. Lett. B **445**, 449 (1999).
[14] G. Bonvicini *et al.* (CLEO Collaboration), Phys. Rev. Lett. **82**, 4586 (1999).
[15] P. L. Frabetti *et al.* (E687 Collaboration), Phys. Rev. Lett. **71**, 827 (1993).
[16] J. R. Raab, J. C. Anjos, J. A. Appel, S. B. Bracker, T. E. Browder *et al.* (E691 Collaboration), Phys. Rev. D **37**, 2391 (1988).
[17] R. L. Workman *et al.* (Particle Data Group), Prog. Theor. Exp. Phys. **2022**, 083C01 (2022).
[18] Throughout this Letter, charge-conjugate modes are implicitly included unless noted otherwise.
[19] T. Abe (Belle II Collaboration), arXiv:1011.0352.
[20] W. Altmannshofer *et al.*, Prog. Theor. Exp. Phys. **2019**, 123C01 (2019).
[21] K. Akai, K. Furukawa, and H. Koiso, Nucl. Instrum. Methods Phys. Res., Sect. A **907**, 188 (2018).
[22] K. Adamczyk *et al.* (Belle II SVD Group), J. Instrum. **17**, P11042 (2022).
[23] B. Wang (Belle II TOP Group), arXiv:1709.09938.
[24] S. Jadach, B. F. L. Ward, and Z. Wąs, Comput. Phys. Commun. **130**, 260 (2000).
[25] T. Sjöstrand, S. Ask, J. R. Christiansen, R. Corke, N. Desai, P. Ilten, S. Mrenna, S. Prestel, C. O. Rasmussen, and P. Z. Skands, Comput. Phys. Commun. **191**, 159 (2015).
[26] D. J. Lange, Nucl. Instrum. Methods Phys. Res., Sect. A **462**, 152 (2001).
[27] S. Agostinelli *et al.* (GEANT4 Collaboration), Nucl. Instrum. Methods Phys. Res., Sect. A **506**, 250 (2003).
[28] E. Barberio and Z. Was, Comput. Phys. Commun. **79**, 291 (1994).
[29] T. Kuhr, C. Pulvermacher, M. Ritter, T. Hauth, and N. Braun (Belle II Analysis Software Group), Comput. Softw. Big Sci. **3**, 1 (2019).
[30] 10.5281/zenodo.5574115.
[31] J. F. Krohn *et al.* (Belle II Analysis Software Group), Nucl. Instrum. Methods Phys. Res., Sect. A **976**, 164269 (2020).

Certificate

Latika Aggrawal

has successfully participated and presented a talk titled

Rare charm decays at Belle II

XXIV DAE-BRNS Symposium on High Energy Physics
held **ONLINE** by the
National Institute of Science Education and Research
Jatni 752050 Odisha India
during
December 14-18, 2020

Prof. Bedangadas Mohanty
(Chair)

Prof. Sanjay Swain
(Co-Chair)

Sponsors & Organizers

INDIAN INSTITUTE OF SCIENCE EDUCATION AND RESEARCH MOHALI

(Established by the Ministry of Education, Govt. of India)

Knowledge City, Sector 81, S. A. S. Nagar, Manauli PO 140306, Punjab, India

---

Certificate

On behalf of the local organizing committee, this is to certify that

Latika Aggarwal (Panjab University, Chandigarh)

presented a poster titled

MEASUREMENTS OF THE RATIO OF PARTIAL WIDTHS
$\Gamma(D_s^{*+} \to D_s^+\pi^0)/\Gamma(D_s^{*+} \to D_s^+\gamma)$ [Abstract ID 321]

at the **XXV DAE-BRNS High Energy Physics Symposium 2022**.

The XXV DAE-BRNS high energy physics symposium (*silver jubilee edition*) was held from 12-16 December 2022 at Indian Institute of Science Education and Research Mohali, Punjab, India. The symposium is a premier event held every two years, supported by the Board of Research in Nuclear Sciences (BRNS), Department of Atomic Energy (DAE), India. The deliberations, from both experimental and theoretical perspectives, covered a variety of topics in Astroparticle Physics, Cosmology, Dark matter, Flavor physics, Higgs, Heavy-ion, LHC physics, Neutrino, Societal applications and related areas.

Ambresh

Dr. Ambresh Shivaji, Convener,
XXV DAE-BRNS HEP Symposium,
Indian Institute of Science Education and Research Mohali,
Sector 81, Knowledge City, SAS Nagar,
Punjab-140306, India

CHASCON 2023

NATIONAL CONFERENCE ON

GLOBAL SCIENCE FOR GLOBAL WELLBEING

October 12-14, 2023

RUSA

G20

CRIKC

Certificate of Presentation

Certified that Ms. Latika Aggarwal of University Institute of Engineering and Technology, Panjab University, Chandigarh participated and gave an Oral Presentation entitled "Measurement of the branching fraction of the excited strange charm meson decays" in the Physical Sciences Section of 16th Chandigarh Science Congress (CHASCON 2023), organized by Panjab University, Chandigarh in association with CRIKC from October 12-14, 2023.

Dr. Y. K. Rawal	**Prof. Ajay Mittal**	**Prof. Neena Capalash**
CO-COORDINATOR	CO-COORDINATOR	COORDINATOR